Origin of Polarization Behavior in All-Solid-State Lithium-Ion Battery Using Sulfide Solid Electrolyte

Kezheng Chen

Contents

General Introduction

Part A. Origin of Interfacial Resistance

Chapter 1. Elucidation of the Effect of Introducing Li_3PO_4 Interlayer into $LiCoO_2$/Li_2S-P_2S_5 Interface in All-Solid-State Battery

Chapter 2. Elucidation of the Effect of Introducing Li_3PO_4 Interlayer into $LiNi_{0.5}Mn_{1.5}O_4$/Li_2S-P_2S_5 Interface in All-Solid-State Battery

Part B. Origin of Reaction Distribution

Chapter 4. Elucidation of Reaction Distribution in Composite Electrode of All-Solid-State Battery by Two-Dimensional X-Ray Absorption Spectroscopy

General Introduction

1. Background

In recent years, due to the potential risk of fossil-fuel exhaustion and environmental pollution during the burning of fossil fuel, the use of clean-energy sources instead of fossil fuel has been given great attention. As one of the biggest consumers of energy, the transportation vehicle is also undergoing a transformation of power source: from fossil fuel to electricity. The number of hybrid electric vehicles and even purely electric vehicles sold in the commercial market has increased, and the range of application of these vehicles is also expanding.[1]

There are several methods to generate clean electric power, such as solar radiation, wind, and waves. However, the most convenient and economic method of storing electric energy for portable devices and vehicles is the chemical battery.[2] The battery is capable of storing chemical energy as well as transforming chemical energy into electrical energy with a high conversion efficiency and no harmful exhaust. The requirements for the rechargeable battery are high voltage, high capacity, rate capability, and reliable safety. To satisfy these needs, numerous types of batteries have been developed with continuously improving battery performance, such as the lead-acid battery, zinc-carbon battery, and nickel-hydrogen battery.[3] Since the lithium-ion batteries (LIBs) were first commercialized in 1991 by Sony Enterprise Co., Ltd., their high energy and power density have made them the best choice for power supply in

portable electronics.[4] Furthermore, due to the technological development of LIBs, they are also considered to be the main power source for electric vehicles. However, since conventional LIBs use flammable organic liquid electrolytes, they suffer from potential risks such as volatilization, flammability, and explosion. Therefore, the safety performance of LIBs need to be improved for the application in electric vehicles. [5]

2. Lithium-Ion Secondary Battery

Lithium-ion batteries play a very important role in modern society. Before discussing next-generation all-solid-state batteries, a review of conventional lithium-ion batteries is necessary. In this section, the mechanism and structure of lithium-ion batteries will be briefly explained. Cathode and anode materials of conventional lithium-ion batteries will be introduced later in this section, and solid electrolytes will be discussed in the next section.

The operation of the lithium-ion secondary battery is briefly described here. Figure 1 is a schematic diagram of a representative commercial lithium-ion secondary battery. A Li-containing transition metal oxide such as $LiCoO_2$ is used as the cathode, graphite is used as the anode, and organic electrolyte in which lithium salts are dissolved is used as the electrolyte. The charge / discharge reaction formula of this battery can be expressed as (1) to (3).

$$\text{Cathode}: \quad Li_{1-x}CoO_2 + xLi^+ + xe^- \Leftrightarrow LiCoO_2 \tag{1}$$

$$\text{Anode}: \quad Li_xC_6 \Leftrightarrow xLi^+ + xe^- + C_6 \tag{2}$$

$$\text{Entire}: \quad Li_{1-x}CoO_2 + Li_xC_6 \Leftrightarrow LiCoO_2 + C_6 \tag{3}$$

Lithium ions in the crystal structures of the cathode material are drawn out by the

charge process and are transported into the electrolyte, and lithium ions in the electrolyte are inserted into the porous structure of the anode material. Accordingly, to maintain electric neutrality, electrons must move from the cathode to the anode via an external circuit that needs an external electrodynamic potential. At the time of discharge, the opposite reaction occurs. Lithium ions and electrons move from the negative electrode to the positive electrode via the interior of the battery and the external circuit, respectively, which creates a current in the external circuit, doing work. Therefore, a battery with charge/discharge reversibility can be constructed.

2.1. Cathode Materials

The capacity and operating potential of various cathode materials used in lithium-ion batteries are shown in Table 1. Currently, mainstream cathode materials include layered oxides (e.g., $LiCoO_2$), spinel oxides (e.g., $LiMn_2O_4$), and olivine oxides (e.g., $LiFePO_4$). Furthermore, sulfur-based materials exhibiting high theoretical capacity are drawing an increased amount of attention as one of the next-generation cathode materials.

Layered oxide-based cathode materials show a maximum capacity of about 300 $mAh \cdot g^{-1}$, but due to their weaknesses in high output power and thermal stability, they are often applied to small mobile devices that need high energy density.[4] Although spinel-type and olivine-type cathode materials have better thermal stability and output performance, they are usually used for mobile vehicles and large-scale storage battery systems because of their relative low capacity of 150 $mAh \cdot g^{-1}$ and low conductivity.[5]

In recent years, the demand for batteries with high energy and power density has

increased rapidly, so it is necessary to improve current cathode materials and, simultaneously, search for new high-performance cathode materials. One example is sulfur-based cathode materials with an overwhelmingly high theoretical capacity of about 1700 $mAh \cdot g^{-1}$.[11] However, due to the chemical property of sulfur, improvement in their safety and cycle performance is still necessary.

2.2. Anode Materials

As shown in Table 2, the current anode materials from the lithium-ion secondary battery ideally have the largest base potential (–3.045 V vs. NHE) among metals, with a very large energy density (3860 $mA \cdot g^{-1}$). There is a problem: lithium-ion batteries using lithium metal have not been put into practical use in terms of life cycle and safety. Currently, graphite (theoretical capacity = 372 $mAh \cdot g^{-1}$) that stores lithium ions between layers is mainly used.[12]

One of the next-generation negative electrode material candidates for improving capacity is a Si-based material. These materials do not form dendrites because they are Li alloys. The capacity of Si greatly exceeds that of graphite, expected to be 4000 $mAh \cdot g^{-1}$ or greater.[14] However, Si reacts with the electrolyte and by-products deposited on the electrode surface, hindering the reaction. Also, as the Li alloy expands to about four times the original volume, the volume change in charging and discharging is so great that the electrode will be pulverized as a result of repeated charge and discharge cycles.

In recent years, studies have been conducted such that directly using lithium metal as a negative electrode is possible by introducing a solid electrolyte and solidifying the

entire lithium-ion secondary battery.

2.3. Electrolyte materials

The operation of the lithium ion secondary battery depends on the repeated movement of lithium ions between the cathode and the anode. It is the electrolyte that serves as a bridge for the movement of lithium ions. Since the movement speed of lithium ions greatly affects the performance of the battery, it is desirable for the electrolyte to have a high lithium ion conductivity. Also, since the operating voltage of the lithium ion secondary battery is about 3.6 V and exceeds the potential window of water, it is not possible to use aqueous electrolyte. For this reason, in most lithium ion secondary batteries, an organic electrolyte having a lithium salt dissolved in an organic solvent with the capability to withstand high voltage is currently used. Table 3 shows the physical properties of major organic solvents proposed to act as electrolyte for lithium ion secondary batteries.

A currently used liquid electrolyte in lithium ion secondary batteries is a lithium salt with a concentration of about 1 $mol \cdot dm^{-3}$, dissolved in a carbonate-type mixed solvent that has a high specific dielectric constant and a relatively wide range of potential windows. Ethylene carbonate (EC) has a high dielectric constant and high stability against oxidation and reduction. In addition, since it forms a surface coating (SEI) capable of inserting and extracting lithium ions from a carbon-based negative electrode, it is used as a solvent for a lithium ion secondary battery. However, EC has a low melting point and is solid at room temperature; it has high viscosity and low ionic conductivity, so EC alone cannot be used as a solvent. Therefore, dimethyl carbonate (DMC), diethyl

carbonate (DEC), ethyl methyl carbonate (EMC), and other linear carbonates that have a low melting point and low viscosity are mixed and used as mixed solvent 60. Also, a lithium salt that dissolves in an organic solvent and plays a role as a carrier for lithium ions is a solute. There are many lithium salts, but many have high ionic conductivity and wide potential windows. Physical properties of representative lithium salts are shown in Table 4. A wide variety of electrolytic solutions can be made by combining the above-mentioned solvent and solute.

In recent years, due to the development of mobile devices such as smartphones and wearable devices, there has been an increasing demand for batteries that are thinner and more flexible. Conventionally, in a storage battery using a liquid electrolyte, liquid leakage may occur, so the thickness and shape of the battery are almost determined. Therefore, using solid polymer electrolyte instead of liquid electrolyte was proposed. Table 5 shows the ionic conductivity of the gel-based polymer electrolyte.

Although polymer electrolytes are widely applied to portable devices using small currents, they are not suitable for electric vehicles that are using high current. Therefore, new electrolytes with even higher ionic conductivity are needed. Moreover, since the polymer electrolytes are organic like liquid electrolytes, their durability is weak against heat generated at a high current and electrolysis occurring at a high potential. To avoid the weak points of liquid and polymer electrolytes, to realize further safety and high capacity, and for high power battery storage, research on incombustible inorganic solid electrolytes has been conducted. Inorganic solid electrolytes will be discussed in section 3.

3. Inorganic Solid Electrolyte

The solid electrolyte in all-solid-state batteries works not only as an electrolyte but also as the separator between cathode and anode. Since solid electrolytes do not burn, leak, or corrode, the safety of all-solid-state batteries is much higher than conventional lithium-ion batteries. Important properties that are pursued for ideal solid electrolytes include: high ionic conductivity, high thermal stability during charge and discharge, wide electrochemical stability window against high-voltage cathode, and chemical stability in the presence of a Li metal anode.[17,18] The varieties of existing inorganic solid electrolyte can be classified as: oxide solid electrolytes, sulfide solid electrolytes, and nitride solid electrolytes. The typical solid electrolyte of each type will be discussed in this section with regard to their structure, ionic conductivity mechanism, advantages, and disadvantages. As the most important property of solid electrolyte, the ionic conductivity need to be about 10^{-3} S·cm^{-1}. However, most of the existing solid electrolytes are far away from this objective. Two ionic transport models are used to quantify the ionic conductivity of solid electrolytes currently—the Arrhenius and Vogel-Tammann-Fulcher models. The Arrhenius model is most suitable for inorganic electrolytes with a fixed crystal structure. It is described as:

$$\boldsymbol{\sigma = A \exp\left(\frac{-E_a}{kT}\right)} \tag{4}$$

where A is a pre-exponential factor obtained by extrapolation to infinite temperature T, E_a is the activation energy, and k is the Boltzmann constant.[19] The Vogel-Tammann-Fulcher model is more suitable than the Arrhenius model for materials with free volume,

such as polymer electrolytes. It is represented as:

$$\boldsymbol{\sigma = A\,T^{-\frac{1}{2}}\exp\left(-\frac{B}{T-T_0}\right)} \quad (5)$$

where *A* is a pre-exponential factor obtained by extrapolation to infinite temperature *T*, B is the pseudo-activation energy, which is the delegate of E_a/k, and T_0 is the reference temperature.[19]

3.1. Nitride Solid Electrolyte

Single-crystal Lithium nitride (Li_3N) is one of the earliest reported solid electrolyte. The hexagonal Li_2N layers connected by pure Li layers with N-Li-N bonds form a very open intersecting channel in two dimensions for Li conduction. This 2D structure increases the ionic conductivity to as high as 10^{-3} $S{\cdot}cm^{-1}$ at room temperature for Li_3N.[20] At a different pressure, the single-crystal Li_3N was demonstrated to undergo a phase transformation. When the pressure is less than 0.6 GPa, the single-crystal Li_3N will transform into an α-Li_3N phase with a hexagonal structure. When the pressure is greater than 0.6 GPa, a β-Li_3N phase with hcp structure will be formed. By a first-principles calculation, the lithium ion diffusion mechanism in these two kinds of phase were analyzed. The diffusion mechanism in α-Li_3N is considered to be the favorable diffusion in Li_2N layers, while the diffusion mechanism in β-Li_3N is considered to be the diffusion in pure Li layers.[21] However, due to its extreme low electrochemical decomposition potential (0.445 V vs Li/Li^+) as well as the poor stability, its application as a solid electrolyte used in all-solid-state batteries has been hindered.

Glassy LiPON electrolyte synthesized by sputtering using Li_3PO_4 target in N_2

atmosphere has an ionic conductivity of 3.3×10^{-6} S·cm^{-1} and a wide electrochemical window of 5.5 V. Due to its high electrochemical stability, LiPON is still one of the best choice to fabricate thin-film electrolytes used in miniature batteries. The internal resistance of LiPON will also become lower with decreased thickness. Thin-film electrolytes can supply an intimate contact with the electrode materials and lower the interfacial resistance. However, an ultrathin film electrolyte risks being pierced when it comes into contact with a rough surface of electrode materials, causing an internal short circuit and invalidating the battery system.[21]

3.2. Oxide Solid Electrolyte

The typical LISICON-type compound solid electrolyte $Li_{14}Zn(GeO_4)_4$ was first reported by Hong et al. (1978).[22] It can be considered to be a solid solution of Li_4GeO_4 and Zn_2GeO_4. The schematic diagram of the crystal structure of $Li_{14}Zn(GeO_4)_4$ is shown in Figure 3. The lithium ions occupying the interstitial octahedral sites based on γ-Li_2ZnGeO_4 are responsible for the ionic conductivity in this solid electrolyte.[21] The ionic conductivity of $Li_{14}Zn(GeO_4)_4$ is 0.13 S·cm^{-1} at 573 K with a low migration activation energy of about 0.24 eV.[22] Due to the intrinsic thermal stability, LISICON-type electrolytes can be operated at high temperature. However, the relatively low ionic conductivity at room temperature (10^{-7} S·cm^{-1}) and the instability of Ge towards lithium metal and air restrict their application.[23]

The first sodium superionic conductor (NASICON) $Na_{1+x}Zr_2P_{3-x}Si_xO_{12}$ was reported by Goodenough *et al.* (1976).[26] This material was synthesized by partial replacement of P with Si in $NaM_2(PO_4)_3$ (M = Ge, Ti, or Zr). When the sodium ion is replaced by lithium

ion, this material can turn into NASICON-type compound lithium ionic conductor. However, the original channels for sodium ions are too large for lithium ions and the Li-O bonds is more covalent than Na-O bond, the lithium ion conductivity is lower than sodium ionic conductivity.[20] Therefore, different elements and valences substitution or partial substitution of the framework ions is used to enhance the lithium ion conductivity.

More common NASICON-type compound lithium-ion solid electrolyte $Li_{1+x}Al_xGe_{2-x}(PO_4)_3$ (LAGP) and $Li_{1+x}Al_xTi_{2-x}(PO_4)_3$ (LATP) is formed by partially replacing Ge and Ti by Al since the Al ion has a smaller ionic radius than that of Ge and Ti.[18,25] LAGP and LATP can show remarkable enhancement of lithium ion conductivity due to small uniform grains of these solid electrolyte can form at appropriate temperature which have more favorable conductive phases.[27] The crystal structure of NASICON-type solid electrolyte is shown in Figure 4. The corner-sharing PO_4 tetrahedra and MO_6 octahedra form the framework and the Na occupies interstitial sties, transporting along the *c*-axis. The highest reported ionic conductivities of LAGP and LATP at room temperature are 10^{-3} and 10^{-2} S cm^{-1}[28,29], respectively. However, the Ti^{4+} can be easily reduced by Li metal anode, which restricts the application of LATP. Therefore, the solid electrolyte LAGP without T is more suitable for wide application.[30]

The typical garnet-type compound solid electrolytes have nominal chemical compositions of $Li_5La_3M_2O_{12}$ (M = Nb or Ta) and $Li_6ALa_2M_2O_{12}$ (A = Ca, Sr, or Ba; M = Nb or Ta).[31] These two compounds are isostructural, but show different ionic conductivities of 10^{-6} and 10^{-5} S cm^{-1}, respectively[32]. The crystal structure of garnet-type solid electrolyte is shown in Figure 5. Infinite chains of $(La_3M_2O_{12})_n$– which are

bonded to each other, sharing La ions and Li ions, form the structure of these materials.[31] Neutron power diffraction patterns have shown that the lithium ion conductivity is from a small amount of lithium ions occupying the octahedral sites. The high mobility in octahedral sites due to the static repulsion from the short Li-Li distance is considered to be the mechanism of lithium ion conduction in garnet-type solid electrolytes.[34] However, the redundant Li in garnet-type solid electrolytes will absorb H_2O and CO_2, which limits the application of these materials.

Perovskite-type compound lithium ionic conductors with the general formula of $Li_{3x}La_{2/3-x}TiO_3$, as reported by Inaguma and colleagues, showed a high bulk ionic conductivity up to 10^{-3} S cm^{-1} at room temperature.[35] Their work on aliovalent substitution of metal ions in A-sites in perovskite structure ABO_3 (A = Ca, Sr or La; B = Al or Ti) generated significant interest in this type of solid electrolyte. Most perovskite-type electrolytes have the structure of subcells with La-rich and La-deficient phases alternately arrayed along the *c*-axis (Figure 5). The different La concentration caused by Li concentration distribution make the La-rich and La-deficient phases with different bottleneck size for Li ion conduction. To obtain high ionic conductivity from perovskite-type solid electrolytes, the compositions of these materials need to be carefully designed, because the ionic conductivity is sensitive to the concentration of Li ions, La ions, and vacancies. Also, since the size of cations directly affect the bottleneck between different phases, the substitution of La ions and Ti ions with other elements such as Al and Mg has proved to be effective for enhancing the ionic conductivity.[37] Despite the high ionic conductivity of perovskite-type $Li_{3x}La_{2/3-x}TiO_3$,

the direct contact with Li metal anode will cause Li ion insertion and result in the reduction of Ti^{4+} to Ti^{3+} rapidly. This reaction will lead to high electronic conductivity and restrict the application of $Li_{3x}La_{2/3-x}TiO_3$.

Generally speaking, oxide solid electrolytes show relatively high chemical stability due to their inherent properties that make them easy to synthesize and operate. However, the relatively low ionic conductivity compared to sulfide solid electrolytes restricts their wider application.[38]

3.3. Sulfide Solid Electrolyte

Compared to nitride solid electrolytes and oxide solid electrolytes, most sulfide solid electrolytes have higher Li^+ conductivity. Further, due to their soft mechanical properties, all-solid-state batteries using sulfide solid electrolyte are easier to manufacture by pressing, and the contact between the cathode and electrolyte is better than that for nitride and oxide solid electrolytes.[39]

Binary Li_2S–P_2S_5-based sulfide glassy solid electrolyte with LiI doping was firstly reported by Mercier *et al.* (1981).[41] A class of Li_2S-SiS_2 sulfide glassy solid electrolytes with lithium halides doping reported by Kennedy and Zhang show ionic conductivity higher than 10^{-4} $S \cdot cm^{-1}$. After these study, using mechanical milling method, a large number of glassy sulfide electrolytes based on xLi_2S-$(1-x)P_2S_5$[41-44] and $(x)Li_2S$-$(1-x)SiS_2$[45,46] have been synthesized. With partial substitution of S by Se, Shin *et al.* synthesized both amorphous and crystalline $75Li_2S$-$(25-x)P_2S_5$–$(x)P_2Se_5$ solid electrolyte. Their work confirmed that Se is incorporated into amorphous matrix and crystal lattice. The ionic conductivity of crystalline showed a high conductivity of about

6×10^{-4} S·cm^{-1}.[49]

Since the discovery of a new sulfide solid electrolyte, Li_3PS_4, by Taches *et al.* (1984), research of crystalline sulfide solid electrolyte began to accelerate.[50] Because S^{2-} exhibits a larger ionic radius, more polarizable characteristics, and lower electronegativity than O^{2-}, Kanno *et al.* substituted O^{2-} with S^{2-} and obtained Li_4GeS_4 and $Li_{4-x}Ge_{1-x}P_xS_4$, which shows higher intrinsic ionic conductivity.[19,47,51] Among them, $Li_{3.25}Ge_{0.25}P_{0.75}S_4$ displays a high ionic conductivity of 2.2×10^{-3} S·cm^{-1} at room temperature.[17] The enhancement of ionic conductivity in these thio-LISICON-type is due to the replacement of O^{2-} with S^{2-}, which weakens the bonding of lithium ion with a framework structure and expands the ion transport passage.[50] By heat processing after ball milling, a series of glass-ceramic electrolytes based on xLi_2S-$(1-x)P_2S_5$ was reported by Hayasi *et al.* (2010).[53] The composition ratio of Li_2S and P_2S_5 affects not only the ionic conductivity but also the yield of H_2S, which will hinder the application of sulfide solid electrolyte. In 2011, $Li_{10}GeP_2S_{12}$ (LGPS) was reported by Kamaya *et al.*, which showed an ionic conductivity of 1.2×10^{-2} S·cm^{-1} at room temperature (Figure 6a).[54] By ab initio molecular dynamics simulations, the high ionic conductivity is confirmed to be the result of its rapid transport of the lithium ion in the one-dimensional conduction pathway along the *c*-axis (Figure 6b). However, a first principles calculation carried out by Ceder *et al.* demonstrated that LGPS was a metastable phase and its instability towards the lithium metal anode at low voltage would restrain its application in all-solid-state batteries.[55]

Generally speaking, the relatively high ionic conductivities and the ductile

mechanical properties of sulfide solid electrolytes are the greatest advantages compared to their counterparts. Their relatively low grain boundary resistance compared with those of oxide electrolytes is considered as one of the reasons why sulfide solid electrolytes show the highest ionic conductivity. However, due to the usage of S, their high hygroscopic nature, which generates harmful H_2S gas results in serious safety concern. Moreover, the relatively narrow electrochemical window of sulfide solid electrolytes hinder their large-scale manufacture and usage.

4. Application of Solid Electrolyte

Since the transference number of the solid-state electrolyte approaches one, ultra-high rate discharging becomes possible by using solid-state electrolyte. In 2016, Kato *et al.* discovered a new lithium superionic conductor, $Li_{9.54}Si_{1.74}P_{1.44}S_{11.7}Cl_{0.3}$, which has the LGPS-type crystal structure (Figure 7a)[56,57] This solid electrolyte showed an unprecedented ionic conductivity of 2.5×10^{-2} S·cm^{-1} which is two times greater than conventional LGPS solid electrolytes. It is also the highest conductivity value reported so far for lithium superionic conductors. The nuclear density distribution (Figure 7b) calculated by using the maximum entropy method indicates the three-dimensional conduction pathways (one-dimensional along the *c*-axis and two-dimensional in the *ab*-plane) in $Li_{9.54}Si_{1.74}P_{1.44}S_{11.7}Cl_{0.3}$. All-solid-state cells using $LiNbO_3$-coated $LiCoO_2$ as cathode, $Li_4Ti_5O_{12}$ as anode and $Li_{9.54}Si_{1.74}P_{1.44}S_{11.7}Cl_{0.3}$ as electrolyte exhibited excellent rate capabilities, with discharge current density of 150 C at 25 °C and 1500 C at 100 °C (Figure 8a). These all-solid-state cells also showed excellent cycling performance, with nearly 75% capacity retention and a 100% coulombic efficiency

after over 500 cycles.[56] This extraordinary cell performance has greatly encouraged research into solid electrolytes.

It is also well known that many solid electrolytes have a wider electrochemical window than liquid electrolytes.[57,58] Their electrochemical stability provide the capability to apply a high-voltage cathode, such as $LiNi_{0.5}Mn_{1.5}O_4$[59] and $LiCoPO_4$, to an all-solid-state battery[60], which could greatly improve the power density. Moreover, since solid electrolytes are able to suppress the formation of lithium dendrites, the application of metallic lithium becomes possible, which can provide the highest capacity density for anodes.[61]

Since inorganic solid electrolytes are nonflammable and thermotolerant, the safety issue in batteries using liquid electrolytes, such as liquid leak, combustion, and explosion, can be avoided in all-solid-state batteries.[62] The outstanding safety performance of all-solid-state batteries using inorganic solid electrolytes are particularly suitable for electric vehicles, which are sensitive to safety problems.

5. Problems of All-Solid-State Battery

Despite the advantages of all-solid-state batteries, there are still many problems that prevent the achievement of longevity, high energy density, and high power density for current LiBs using solid electrolytes, restricting their application.[18,48] These problems could be divided into three types according to their spatial scales. As shown in Figure 9, they are: the high interfacial resistance between electrode and solid electrolyte, the low ionic conductivity in solid bulk electrolytes, and the reaction distribution in composite electrodes.

Since the micrometer-scale structures of solid electrolytes have been most discussed in section 1.3, this section will focus on the interfacial resistance and reaction distribution problems.

5.1. Interfacial Resistance between Electrode and Solid Electrolyte

Unlike the electrode / liquid electrolyte interface in conventional lithium-ion batteries, the electrode / solid electrolyte will be a solid-solid interface for the all-solid-state battery. Therefore, the interface design guideline based on the electrochemical analysis of the solid-liquid interface will be inapplicable for the all-solid-state battery. Due to the great difference in interfacial stress and expansion coefficient between solid electrodes and solid electrolytes, the contact between them will deteriorate during long-term operation, which is one of the reasons for high interfacial resistance.[63] Since sulfide solid electrolytes are usually softer than oxide solid electrolytes, their good contact with solid electrodes under a constant high pressure should be easier to achieve. However, even with the soft sulfide solid electrolyte, the interfacial resistance is still very high, influencing the performance of all-solid-state batteries.[66] The detailed reaction mechanism at the electrode / solid electrolyte interface needs to be elucidated so that the interfacial resistance can be reduced.

Interfacial modification between electrode and solid electrolyte is an effective way to reduce the interfacial resistance and improve the cell performance. For example, coating ZrO_2 on $LiNi_{1/3}Mn_{1/3}O_2$ by the sol-gel method successfully lowered the interfacial resistance between $LiNi_{1/3}Mn_{1/3}O_2$ cathode and amorphous Li_3PS_4 solid

electrolyte. Both the charge-discharge capacity and cycle performance were improved due to the reduced interfacial resistance.[69] Ohta *et al.*[70] reported that the nanoscale $Li_4Ti_5O_{12}$ coating between $LiCoO_2$ cathode and thio-LISICON solid electrolyte $Li_{3.25}Ge_{0.25}P_{0.75}S_4$ could effectively reduce the interfacial resistance and enhance the high-rate performance of the homologous all-solid-state batteries (In-Li metal as anode). They also discussed the relationship between thickness of $Li_4Ti_5O_{12}$ coating layer and promotion of cell performance. As shown in Figure 10, the sample numbers represent the thickness (nm) of the $Li_4Ti_5O_{12}$ coating layer. Figure 10(a) showed the Nyquist plot of corresponding all-solid-state batteries with different $Li_4Ti_5O_{12}$ coating layer thicknesses. Figure 10(b) showed the discharge curves of corresponding all-solid-state batteries with different $Li_4Ti_5O_{12}$ coating layer thicknesses. Figure 10(c) showed the charge curves at the beginning of the first charge of corresponding all-solid-state batteries with different $Li_4Ti_5O_{12}$ coating layer thicknesses.[70] Although $Li_4Ti_5O_{12}$ is also well-known as an anode material, since lithium ion insertion only occurs at potentials lower than 1.5 V,[69] it could be regard as an electron-insulating solid electrolyte in the operation potential range of $LiCoO_2$ / In-Li (3.8 V–4.2 V). With increasing thickness in the $Li_4Ti_5O_{12}$ coating layer, the interfacial resistance decreases and the discharge capacity increases, as compared to using uncoated $LiCoO_2$. When the thickness of the $Li_4Ti_5O_{12}$ coating layer was 5 nm, the all-solid-state cell showed the lowest interfacial resistance and the highest discharge capacity. When the thickness of the $Li_4Ti_5O_{12}$ coating layer was thicker than 5 nm, the interfacial resistance increased and the discharge capacity decreased. As shown in Figure 10(c), the voltage slope appeared to

a plateau at 3.3 V, faded as the thickness of $Li_4Ti_5O_{12}$ coating layer. When the thickness is greater than 20 nm, the slope disappeared completely. This phenomenon was explained by Ohta *et al.*[70] to be the $Li_4Ti_5O_{12}$ coating layer suppressing the formation of the space-charge layer. The existing theories for the origin of interfacial resistance as well as the interfacial reaction mechanism will be explained in Section 1.4.2.2 (space-charge layer) and Section 1.4.2.3 (reaction product layer).

5.1.1. Origin of Interfacial Resistance: Space-Charge Layer

Hetero-interfaces are present in electrochemical devices. For instance, in a rechargeable battery, the minimum necessary components—cathode, anode, and electrolyte—will form a cathode / electrolyte interface and anode / electrolyte interface. If the electrolyte is liquid, the electrical double layer will form at the electrode / liquid electrolyte interface. While using solid electrolyte, the electrical double layer was considered not to form at the interface, or just be negligible. In recent years, based on the concept of space-charge layer formation and Schottky barrier occurring at the hetero-interface of semiconductors, the relaxation phenomenon by ionic conduction in a solid electrolyte was understood to be the modulation of the interfacial ionic concentration. At these hetero-interfaces, besides the ionic modulation from the ionic relaxation effect, the stress effect at the vicinity of the interface and the effect of interfacial modification were reported. These phenomena were referred collectively as Nanoionics.[70,71]

To understand the properties of the hetero-interface, investigation of the space charge layer model, which is similar to the Schottky barrier formation at the

metal / semiconductor hetero-contact, is necessary. Figure 11(a) shows the schematic diagram of the space-charge layer formation based on the band diagram from the work of Bradikhin *et al.*[74] Since the work function between metal and N-type semiconductor is different, charge transfer will take place and the space-charge layer will form at the interface. The thickness of this layer (L_e) depends upon the concentration of mobile electrons in the conduction band (n_e) and is of the order of the Debye screening radius for electrons in the N-type semiconductor:

$$\boldsymbol{L_e \simeq \sqrt{\varepsilon k T / e^2 n_e}} \quad (6)$$

where ε is the dielectric constant of the N-type semiconductor, e is the electronic charge, k is Boltzmann's constant, and T is the temperature.[72]

On the other hand, when solid electrolytes with ionic conduction contacts metal in the same conditions, a redistribution of ions will take place due to the bending of the internal potential. In other words, the ionic concentration near the interface will change as a function of the distance from the interface. The modulation of the ionic concentration at this hetero-interface is similar to that of the electric double layer in the liquid electrolyte.

As in the all-solid-state battery $LiCoO_2$ / ($Li_4Ti_5O_{12}$) / Li_4GeS_4-Li_3P_4 / In-Li mentioned above, Takada *et al.*[75] find high interfacial resistance at the cathode / solid electrolyte interface, and they attribute the formation of interfacial resistance to existence of the space-charge layer. This theory can be explained in Nanoionics.[73] First, when the oxide solid electrolyte contacts the sulfide solid electrolyte, since the electrochemical potential of these two phases are different, there will be a space-charge

layer formed at the interface (Figure 12(a)). Since the affinity with lithium ions will be higher for oxides, when these two phases come into contact, lithium ions will move from the sulfide electrolyte to oxide electrolyte. Therefore, gradients in lithium ionic concentrations will form on both sides of the interface, which are opposed to each other. The ionic concentration gradient can fill up the gap of electrochemical potential and form stable space-charge layers. Second, when an ion-electron mixed conductor $LiCoO_2$ comes into contact with the sulfide solid electrolyte Li_4GeS_4-Li_3P_4, since $LiCoO_2$ not only has the ionic conductivity like oxide solid electrolyte, but also has electronic conductivity, the gradients at the interface will be different. In cathode $LiCoO_2$, the potential distribution is related to the lithium ion distribution. If a potential distribution occurs in materials with electronic conductivity, the movement of electrons will result. Therefore, although the gradient in the lithium ion concentrations appears at the $LiCoO_2$ side of the interface, it will also be mitigated by the movement of electrons. So, the lithium ion concentration of the $LiCoO_2$ side near interface will not increase. Furthermore, the lithium ion concentration of the sulfide solid electrolyte side need to decrease substantially to form a balanced interface. As a result, the space-charge layer will expand greatly, and a lithium ion deficient layer will appear, which was considered as the origin of the high interfacial resistance (Figure 12(b)). Finally, when $Li_4Ti_5O_{12}$ is introduced as the interlayer between $LiCoO_2$ and Li_4GeS_4-Li_3P_4, there will be two interfaces formed, as shown in Figure 12(c). Since both $LiCoO_2$ and $Li_4Ti_5O_{12}$ are oxides, their difference in electrochemical potential will not be too large, which is the driving force of formation of the space-charge layer. On the other hand, the space-

charge layer between Li_4GeS_4-Li_3P_4 and $Li_4Ti_5O_{12}$ will not be too large since they are both solid electrolytes, and a lithium ion deficient layer will not form. The introduction of oxide solid electrolyte will restrain the formation of a space-charge layer between $LiCoO_2$ and sulfide solid electrolyte, reducing the high interfacial resistance and making good contact between the cathode and solid electrolyte.

5.1.2. Origin of Interfacial Resistance: Reaction Production Layer

As discussed above, Takada *et al.*[75] explained the interfacial reaction mechanism through space-charge layer theory. The premise of that theory is that no other diffusing species except lithium ions can go through the interface. However, Sakuda *et al.*[76] observed mutual diffusion at the interface between $LiCoO_2$ cathode and $80Li_2S \cdot 20P_2S_5$ sulfide solid electrolyte by high-angle annular dark-field scanning transmission electron microscopy (HAADF-STEM) and energy dispersive x-ray spectrometry (EDX). Moreover, the introduction of a Li_2SiO_3 interlayer would restrain the mutual diffusion and hinder the formation of a reaction production layer at the interface. The HAADF-STEM images and linear analysis of EDX of $LiCoO_2$ / (Li_2SiO_3) / $80Li_2S \cdot 20P_2S_5$ interface after the first charge-discharge cycle are shown in Figure 13. At the interface without an Li_2SiO_3 interlayer, the existence of a thick interfacial layer could be observed by HAADF-STEM. The mutual diffusion of Co and S as well as the reduction in P concentration could be confirmed by EDX (Figure 13(a)). On the contrary, at the interface with the Li_2SiO_3 interlayer, the diffusion depth of Co and S became distinctly shallower. The concentration of P did not decrease even near the interface (Figure 13(b)). The difference resulting from the introduction of a Li_2SiO_3

interlayer was also analyzed by electrochemical methods. The Nyquist plots of interfacial resistance and the discharge curves are shown in Figure 14. The interfacial resistance decreased (Figure 14(a)) and the discharge capacity increased significantly (Figure 14(b)) after introducing a Li_2SiO_3 interlayer. These results from electrochemical methods indicate that the cell performance could be greatly improved by the introduction of a Li_2SiO_3 interlayer. In the consideration of results from HAADF-STEM, EDX, and electrochemical methods, Sakuda *et al.*[76] suggested that the reaction production layer form at the interface was responsible for the high interfacial resistance, while the introduction of a Li_2SiO_3 interlayer could restrain the formation of a reaction production layer and lower the interfacial resistance.

5.2. Reaction Distribution in Composite Electrodes

Since the reaction field of the electrochemical reaction is the two-dimensional interface between the electronic conductor and ionic conductor, it is susceptible to constraint by the mass transfer process. Generally speaking, an electrode used in a lithium ion secondary battery is a composite made of active materials (ion-electron mixed conductor), conductive additives (electronic conductor), and binder materials. This is called a composite electrode. Those material particles are three-dimensionally connected to form a porous electrode, and the electrolyte solution (ion conductor) infiltrates into these pores to realize a pseudo-three-dimensional electrode reaction field. As a result, a suitable reaction current density can be secured.

In composite electrodes, electrons are supplied from the current collector side, and ions are supplied from the electrolyte bulk side. Therefore, the polarization due to

electronic conduction resistance and ionic conduction resistance will occur while being transported in the composite electrodes. Considering the two-dimensional movement in the thickness direction of the composite electrode, the degree of polarization shows a distribution with the inclination depending on the position. This is thought to be a cause of the generation of the reaction distribution in the electrode thickness direction.

5.2.1. Internal Resistance in Composite Electrodes

To understand the reaction distribution, let us first consider the resistance components in conventional batteries using organic liquid electrolyte. Figure 15 shows a schematic diagram of a composite electrode. It has a complicated there-dimensional structure, composed of active materials, conductive additives, and binder materials. There are multiple reaction processes in the battery reaction as well as their respective internal resistance components. The main internal resistance components are listed below.

① Resistance about electrons

(1) Resistance in conductive additives and active materials.

(2) Resistance in current collector

(3) Resistance at interfaces such as conductive additives / active materials, conductive additives / conductive additives and active materials / active materials.

② Resistance about ions

(1) Resistance in bulk electrolyte

(2) Resistance in electrolyte within composite electrolyte.

(3) Charge transfer resistance at interface.

(4) Diffusion resistance in active materials.

The operation voltage that can be obtained from a battery is the voltage obtained from the subtraction of the activation overvoltage, the concentration overvoltage, and the Ohmic loss from the equilibrium potential. The Ohmic loss can be expressed by Ohm' law as internal resistance × current, so it is necessary to minimize the internal resistance as much as possible to obtain a greater energy from the battery. In high-rate charge / discharge, reducing the ionic conduction resistance in composite electrode is important to obtain high cell performance. The ionic conductivity of the liquid electrolyte of the lithium ion secondary battery is about 10^{-3} S·cm^{-1}, which is much smaller than the electronic conductivity of conductive additives.[17] In addition, although the composite electrode is porous, and the electrolyte is retained in the pores, the ionic conductivity of composite electrode is smaller than that of the bulk electrolyte, due to the narrow and distorted lithium ion diffusion path in the mixture electrode. The ionic conductivity in porous materials such as composite electrodes or separators is expressed below,[76]

$$\boldsymbol{\kappa_{\mathrm{eff}}} = \frac{\boldsymbol{\kappa\epsilon}}{\boldsymbol{\tau}} \tag{7}$$

where $\boldsymbol{\kappa_{\mathrm{eff}}}$ and $\boldsymbol{\kappa}$ are the effective conductivity in the porous materials and the bulk electrolyte, respectively. The parameter $\boldsymbol{\tau}$ is the geometrical parameter, which is called the tortuosity. The parameter $\boldsymbol{\epsilon}$ represents the porosity of the porous materials. Parameter τ is a function of the structure and network of vacancies and is affected by engineering parameters such as porosity and shape of the pores. If tortuosity is only

dependent on porosity, the effective diffusion coefficient and ionic conductivity in porous materials can be corrected from the bulk electrolyte. In addition, the tortuosity $\boldsymbol{\tau}$ is often simplified by an empirical formula called the Bruggeman equation,[76]

$$\boldsymbol{\tau} = \boldsymbol{\gamma}\boldsymbol{\epsilon}^{\mathbf{1}-\boldsymbol{\alpha}} \tag{8}$$

where γ and α are both constants, and α is called the Bruggeman constant. They are both dependent on engineering parameters such as morphology, porosity, and particle size distribution of the porous materials. Thorat *et al.*[79] calculated the conductivity of 1M $LiPF_6$ in EC: EMC (3:7 v/v%) in composite. They reported that the conductivity is 9.21 $mS \cdot cm^{-1}$, 1.77 $mS \cdot cm^{-1}$ and 0.81 $mS \cdot cm^{-1}$ in bulk electrolyte, composite electrolyte with 50% porosity, and with 30% porosity, respectively. Since low conductivity results in large resistance, it is necessary to improve the ionic conductivity in the bulk electrolyte as well as the effective conductivity in composite electrodes to fabricate a high power battery. However, to further improve the performance of the battery, it is necessary to grasp the correct relationship between the internal resistance components, the electrochemical characteristics, and the reaction distribution, which are influenced by the three-dimensional structure, and design the structure of the composite electrodes according to fundamental theories.

5.2.2. Analysis of Reaction Distribution in Composite Electrodes

It is known that regions with high and low reactivity are unevenly distributed in the composite electrode, and the electrode reaction does not proceed uniformly in the composite electrode. With such a reaction distribution, Joule heat is generated by

concentrating current in a specific region, which will greatly affect the safety of batteries. In the region where heat is generated, the reaction tends to proceed more easily, so that only specific regions are used and the deterioration of the active material will be accelerated. Furthermore, the utilization ratio of the active material in the composite electrode will deteriorate, causing a decrease in output. In large lithium ion secondary batteries used in electric vehicles, the problem of the reaction distribution becomes more significant, since the charge / discharge proceeds with a large current. Therefore, it is necessary to suppress the occurrence of the reaction distribution in composite electrode.

As mentioned above, it is predicted that the occurrence of the reaction distribution is caused by the nonuniformity of internal resistance, in particular, the nonuniformity of ionic conduction resistance and electronic conduction resistance in the composite electrodes.[78-81] Since the vacancies are narrowly distorted, the movement of lithium ions is hindered, which results in large resistance. Therefore, as shown in Figure 16, the electrochemical potential of the ions in the composite electrode exhibits a large slope in the cross-sectional direction of the electrode from the electrode surface side to the current collector foil side. On the other hand, since the electronic conductivity in the composite electrode is often high due to the conductive additives, the potential of electrons in the composite electrode is substantially the same as in the cross-sectional direction of the electrode. Because the difference between the ionic potential and the electronic potential is the driving force of the electrode reaction, the reaction will proceed from the electrode / electrolyte interface. On the current collector foil side,

almost no reaction will take place, since sufficient driving force cannot be obtained. Therefore, the thickness of the active electrode becomes thin, which cannot generate sufficient output capacity. [82]

It is also known that the three-dimensional structure of the composite electrode is important for reducing the reaction distribution and improving the battery characteristics, and the structure has been designed by experience-based estimation and trial and error. For example, Fongy *et al.*[86,87] evaluated the electrochemical properties of composite electrodes with different porosities and estimated that the three-dimensional structure would affect the ionic and electronic conductivities in composite electrolyte. Ng *et al.*[88] and Hess *et al.*[89] measured the current and potential distribution by inserting an electronic conductor or an ionic conductor into the composite electrode. Liu *et al.*[83] reported analysis of reaction distribution by micro XRD. They measured the reaction distribution in the cross-sectional direction in the composite electrodes by irradiating synchrotron radiation x-rays as large as to 2 μm × 5 μm, while changing the sample position, and measuring the diffraction pattern for each specific position. Nanda *et al.*[90] measured the reaction distribution in the cathode using position-resolved Raman spectroscopy with a 1-μm diameter laser. However, since the laser light could not reach the inside of the electrode, when the conductive additives or the binder materials were present, only the information of the outermost surface could be obtained. To estimate the various kinds of conductivities in a thick electrode. Siroma *et al.*[91] proposed an impedance analysis method using an equivalent circuit called a transmission line model. Impedance measurements were carried out on pellet samples prepared by mixing the

solid electrolyte $75Li_2S \cdot 25P_2S_5$ with the active material $LiNi_{1/3}Mn_{1/3}Co_{1/3}O_2$ graphite at different compounding ratios, using a symmetrical cell with SUS current collectors.

In recent years, direct observations of the reaction distribution in composite electrodes by two-dimensional X-ray absorption spectroscopy (2D-XAS) have been reported. For lithium-ion batteries using liquid electrolyte, Orikasa *et al.*[77] measured the reaction distribution in the cross-sectional direction of composite electrodes with different porosities, which were prepared by changing the pressure of the roll press (Figure 17). With the simultaneous measurement method of the effective ionic conductivity and effective electronic conductivity based on the theory proposed by Siroma *et al.*,[92] they suggested that the ionic conductivity was decreased for lower porosity electrodes, which governed the reaction distribution of composite electrodes. Nakamura *et al.*[93] reported the visualization of the reaction distribution in a composite cathode with oxide solid electrolyte during charge by 2D-XAS technique and suggested the reaction distribution was due to the disconnection of the electron pathway in the all-solid-state lithium-ion battery.

6. Outline of the Present Thesis

As mentioned above, overcoming such interfacial limitations and reaction distribution limitations are necessary to improve the performance of the all-solid-state lithium ion battery. To establish a more effective interface for cell reaction between electrode and sulfide electrolyte, it is necessary to elucidate the origin of interfacial resistance and the effect of interfacial modification. Furthermore, to mitigate the reaction distribution in composite electrodes of all-solid-state batteries using sulfide

solid electrolyte, it is necessary to clarify the dominant factor for reaction distribution behavior correlated with the three-dimensional structure of composite electrolyte in all-solid-state batteries using sulfide solid electrolyte.

In general introduction, the fundamental principle and the cathode and anode materials are briefly described. Then, the main inorganic solid electrolytes are classified into oxides, sulfides, and nitrides for a detailed description of their properties. After introducing the components of the all-solid-state battery, the limitations that restrain the practical application of the all-solid-state battery and the efforts to overcome those limitations are introduced within three different scale ranges. Among these limitations, the interfacial resistance at the electrode / solid electrolyte interfaces and the reaction distribution in composite electrolytes are discussed in detail.

In chapter 1, the hetero-interface between a typical 4 V cathode $LiCoO_2$ and sulfide solid electrolyte Li_2S-P_2S_5 are analyzed by electrochemical methods and depth-resolved X-ray absorption spectroscopy (DR-XAS), using model thin-film electrodes. The interfacial modification effect of a Li_3PO_4 interlayer between $LiCoO_2$ and Li_2S-P_2S_5 as well as the interfacial mechanism are described.

In chapter 2, the thin-film model interface between a typical 5 V cathode $LiNi_{0.5}Mn_{1.5}O_4$ and sulfide solid electrolyte Li_2S-P_2S_5 was fabricated and analyzed by electrochemical methods and DR-XAS. Since the use of a high voltage cathode is one of the main advantages of the all-solid-state battery, it is also necessary to clarify the reaction mechanism of the interface between a high voltage cathode and sulfide solid electrolyte. Therefore, the interfacial reaction mechanism and the interfacial

modification effect of a Li_3PO_4 interlayer used in a high voltage all-solid-state battery are discussed in this chapter.

In chapter 3, the Li_3PO_4 interlayer between high voltage cathode $LiNi_{0.5}Mn_{1.5}O_4$ and sulfide solid electrolyte Li_2S-P_2S_5 is replaced by a LiF interlayer. According to the results of chapter 3, the Li_3PO_4 interlayer is thermodynamically and kinetic unstable in the operating voltage range of $LiNi_{0.5}Mn_{1.5}O_4$. To achieve improved battery performance, it is necessary to find a new interlayer that is suitable for a high voltage cathode. According to theoretical calculations, LiF is considered to be effective as an interlayer for $LiNi_{0.5}Mn_{1.5}O_4$. Therefore, electrochemical methods and DR-XAS are used to clarify the effect of a LiF interlayer between $LiNi_{0.5}Mn_{1.5}O_4$ and Li_2S-P_2S_5.

In chapter 4, the reaction distribution of both in-plane direction and simulated cross-sectional direction in composite electrodes ($LiNi_{1/3}Co_{1/3}Mn_{1/3}O_2$ + Li_2S-P_2S_5 + acetylene black + binder material) of an all-solid-state battery using different binder materials are analyzed by 2D-XAS. The correlation between the dispersion state and reaction distribution of composite electrodes in all-solid-state batteries using sulfide solid electrolyte is discussed in this chapter.

In chapter 5, the conclusion obtained from the present studies and prospects for future application of the all-solid-state battery are discussed.

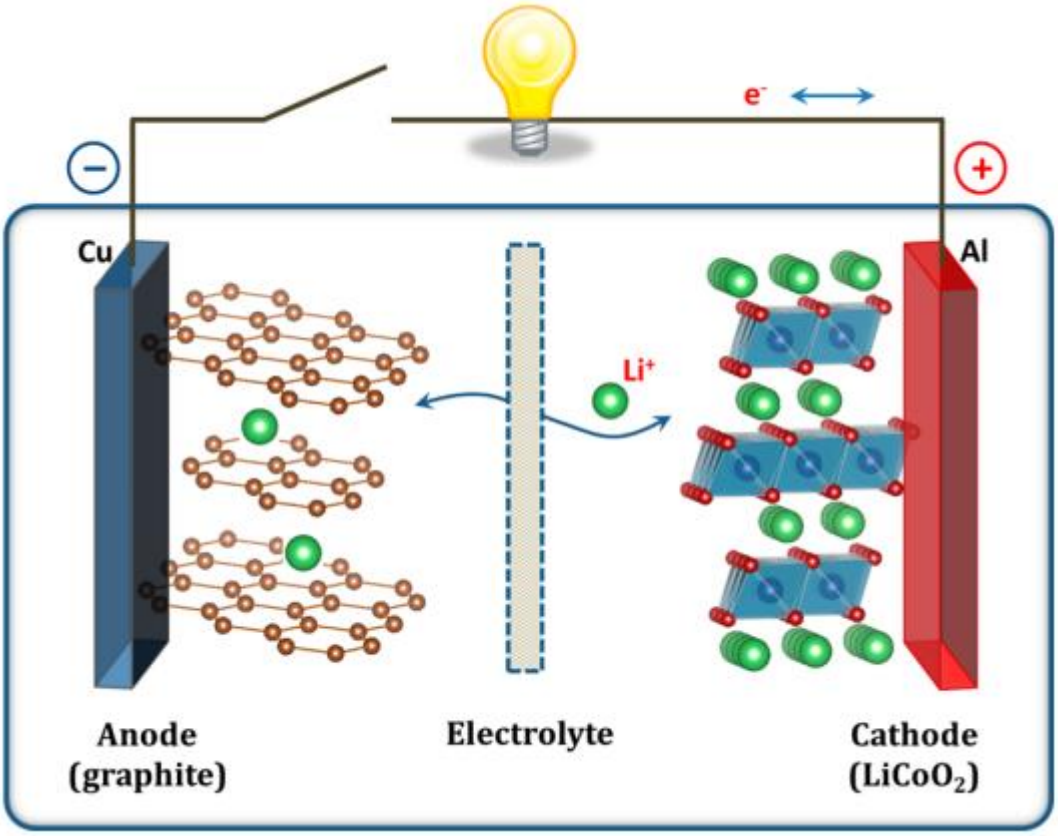

Figure 1 Schematic diagram of a representative lithium-ion secondary battery.[4]

Table 1 Various cathode materials used in lithium-ion batteries

Compound	Crystal structure	Average voltage vs Li/Li^+ (V)	Theoretical capacity ($mAh\ g^{-1}$)	Experimental Capacity ($mAh\ g^{-1}$)
$LiCoO_2$[4]	Layered	3.8	274	148
$LiFePO_4$[5]	Olivine	3.4	170	165
$LiNiO_2$[6]	Layered	3.8	275	150
$LiMn_2O_4$[7]	Spinel	4.1	148	120
Li_2MnO_3[8]	Layered	3.8	458	180
$LiNi_{0.33}Mn_{0.33}Co_{0.33}O_2$[9]	Layered	3.7	280	160
$LiNi_{0.8}Co_{0.15}Al_{0.05}O_2$[10]	Layered	3.7	279	199

Table 2 Various anode materials used in lithium-ion batteries

	Theoretical capacity (mAh g^{-1})	**Lithiation potential vs Li/Li^+ (V)**	**Delithiation potential vs Li/Li^+ (V)**	**Volume change (%)**
Graphite[12]	372	0.10	0.14	10
Li_2TiO_3 [13]	175	1.55	1.58	0.2
Si[14]	4200	0.21	0.47	270
Ge[15]	1625	0.30	0.50	240
Sn[16]	994	0.57	0.70	255

Table 3 Physical properties of some organic solvents[17]

	Melting point T_m / °C	**Boiling point T_b / °C**	**Density / g cm^{-3}**	**Dielectric constant ε**
Dimethyl carbonate (DMC)	2.4	90	1.06	3.12
Diethyl carbonate (DEC)	-43.0	126	0.9752	2.82
γ-butyrolactone (BL)	-43.3	204	1.1284	39.0
Propylene carbonate (PC)	-48.8	242	1.2047	66.14
Ethylene carbonate (EC)	36.4	248	1.3214	89.78
Ethyl methyl carbonate (EMC)	-53	110	1.006	2.958
3-Methyl-2-oxazolidone (NMO)	15	270	1.17	4.52

Table 4 Lithium salts as solute in electrolyte[17]

	Average molecular weight	**Melting point T_m / °C**	**Decomposition point T_d / °C**	**Conductivity in EC/DMC σ / mS cm^{-1}**
$LiBF_4$	93.9	293	＞100	4.9
$LiPF_6$	151.9	200	~80	10.7
$LiAsF_6$	195.9	340	＞100	11.1
$LiClO_4$	106.4	236	＞100	8.4
Li Imide	286.9	234	＞100	9.0
Li Triflate	155.9	＞300	＞100	

Table 5 Some selected polymer gel electrolytes and their conductivity values[18]

Polymer gel electrolytes	**Conductivity / S cm^{-1}**	**Temperature / °C**
PAN-EC/PC/DMF-$LiClO_4$	~4×10^{-4}	22
PMMA-EC/PC-$LiClO_4$	~1×10^{-3}	25
PAN-EC/PC-$LiClO_4$	~4×10^{-3}	25
PVC-EC/PC-$LiClO_4$	~1×10^{-3}	25
PAN-EC/PC-$LiCF_3SO_3$	~1×10^{-3}	20
PAN-EC/DEC-$LiClO_4$	~4×10^{-3}	Room temperature
PVdF-EC/PC-$LiBF_4$	~6×10^{-3}	Room temperature
PVdF-HFP-EC/DEC-$LiN(CF_3SO_2)_2$	~1×10^{-3}	Room temperature
PMMA-EC/PC/γBL-$LiCF_3SO_3$	~1×10^{-3}	Room temperature
PMMA-EC/DMC-$LiN(CF_3SO_2)_2$	~1×10^{-3}	Room temperature

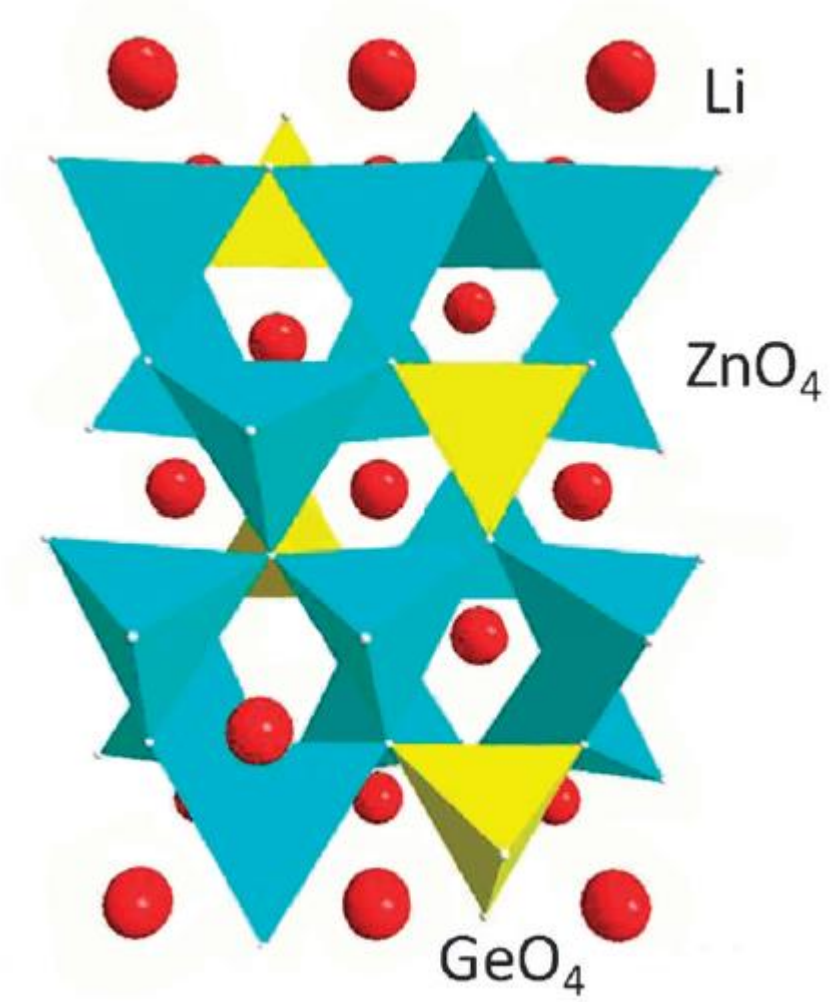

Figure 2 Schematic diagram of the crystal structure of $Li_{14}Zn(GeO_4)_4$. [20]

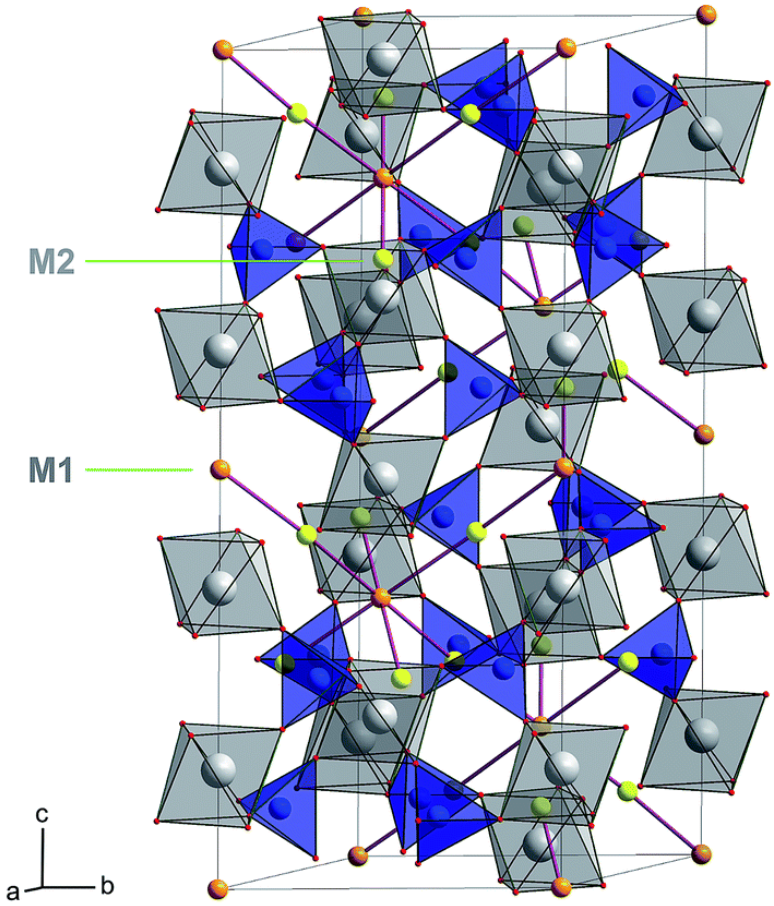

Figure 3 Schematic diagram of the crystal structure of LATP. Orange and yellow spheres represent possible Li sites the ions may use to diffuse through the crystal lattice.[26]

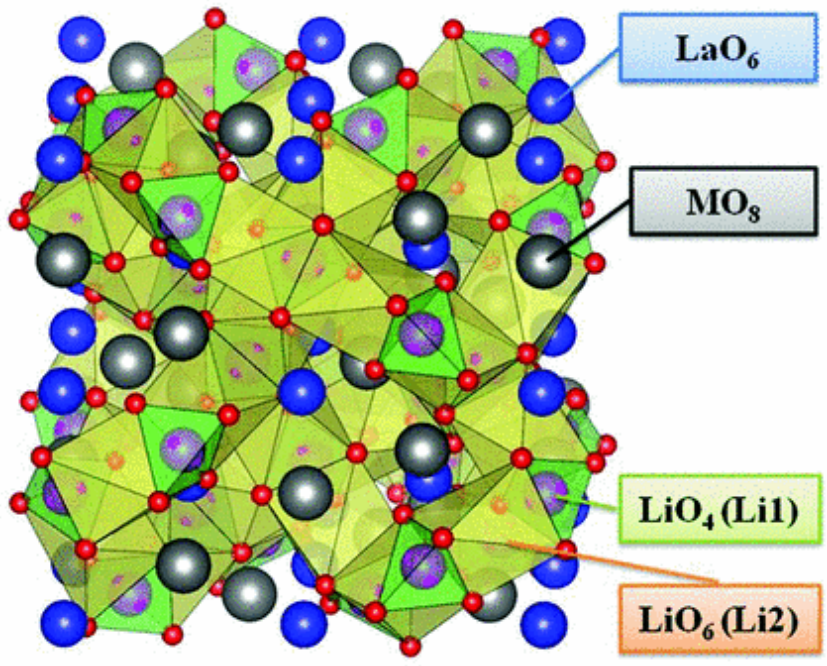

Figure 4 The crystal structure of garnet-type solid electrolyte. The green (dark gray) polyhedrons are tetrahedral Li(1) sites and the yellow (light gray) ones are octahedral Li(2) sites.[33]

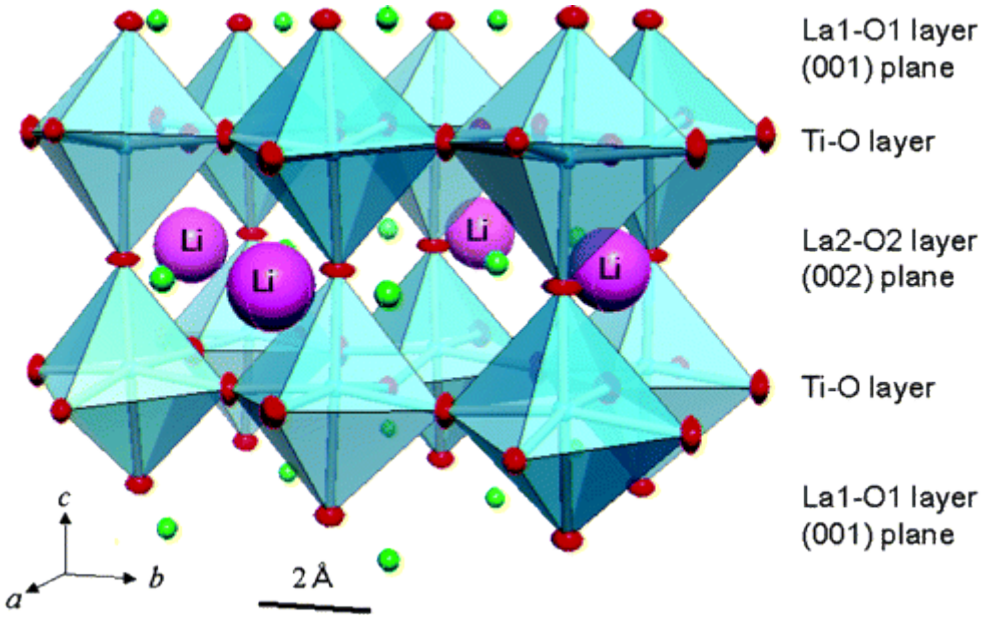

Figure 5 Schematic diagram of the crystal structure of $La_{0.62}Li_{0.16}TiO_3$. The pink, green, blue and red spheres respectively denote Li, La, Ti and O ions.[36]

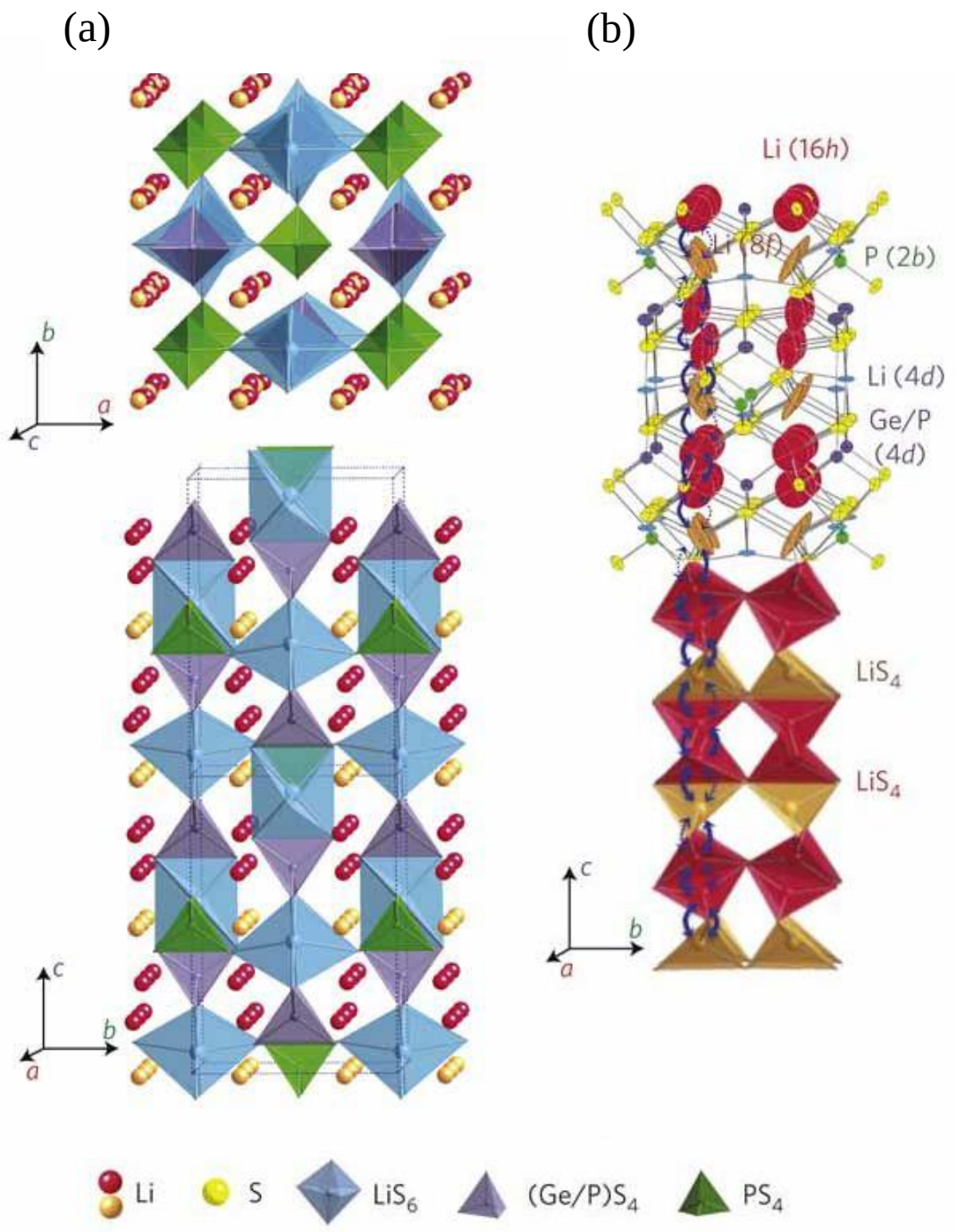

Figure 6 (a) The framework structure of $Li_{10}GeP_2S_{12}$ and lithium ions that participate in ionic conduction. (b) Conduction pathways of lithium ions. [54]

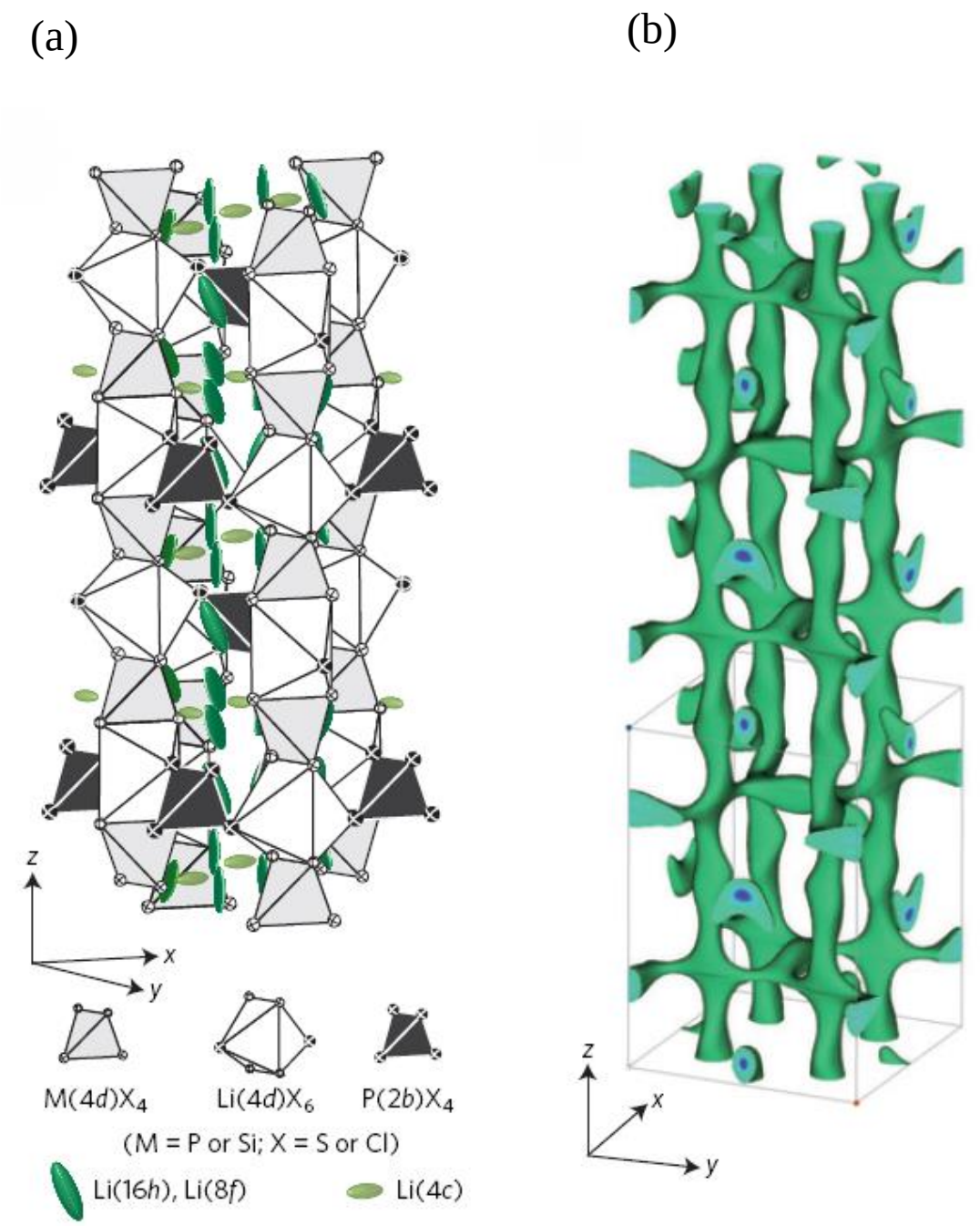

Figure 7 (a) Crystal structure of $Li_{9.54}Si_{1.74}P_{1.44}S_{11.7}Cl_{0.3}$ and lithium ions that participate in ionic conduction. (**b)** Nuclear distributions of Li atoms in $Li_{9.54}Si_{1.74}P_{1.44}S_{11.7}Cl_{0.3}$ at 25 °C. [56]

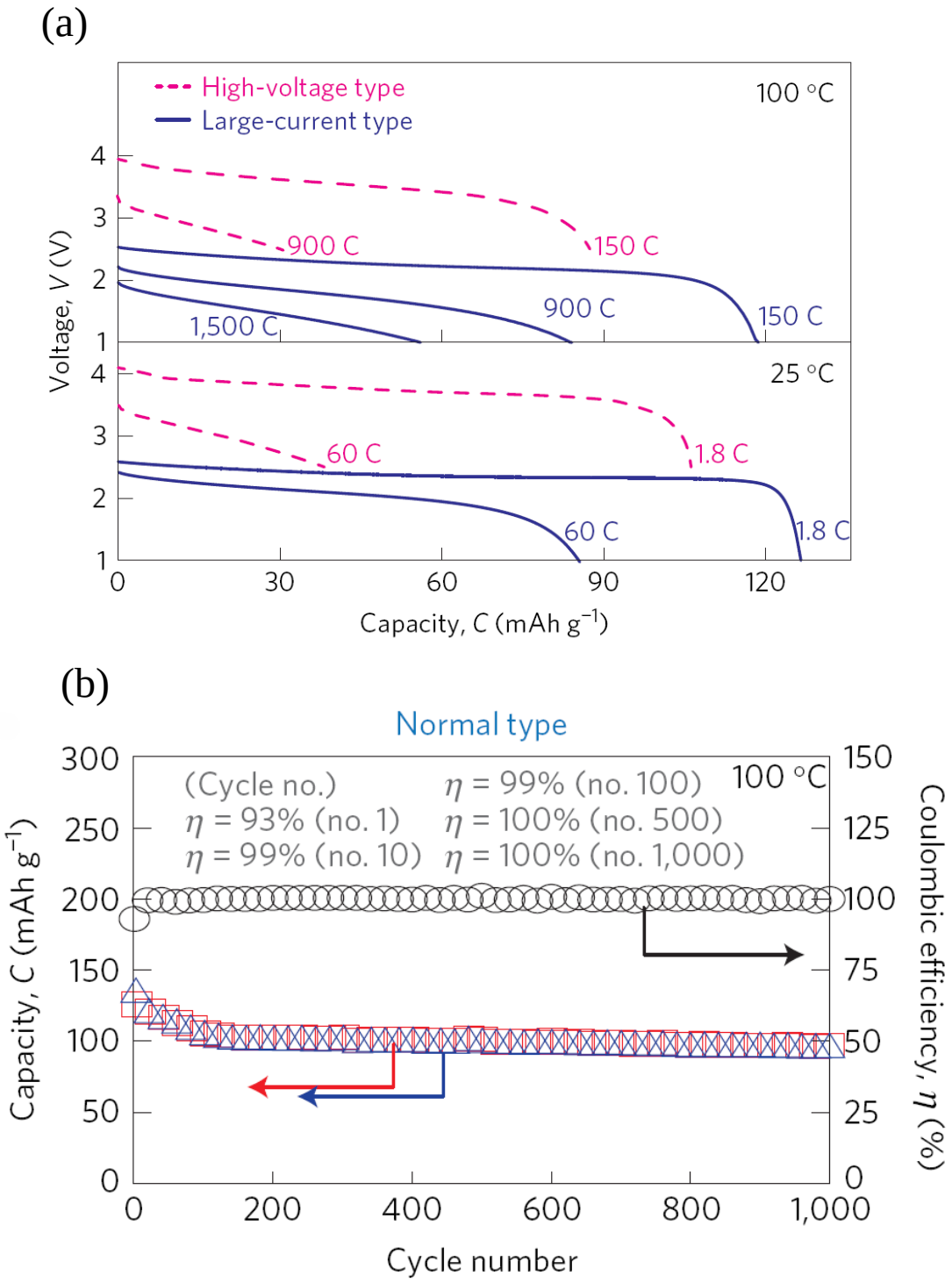

Figure 8 (a) Rate performance and (b) rate capabilities of all-solid-state cells using $Li_{9.54}Si_{1.74}P_{1.44}S_{11.7}Cl_{0.3}$ as electrolyte. [56]

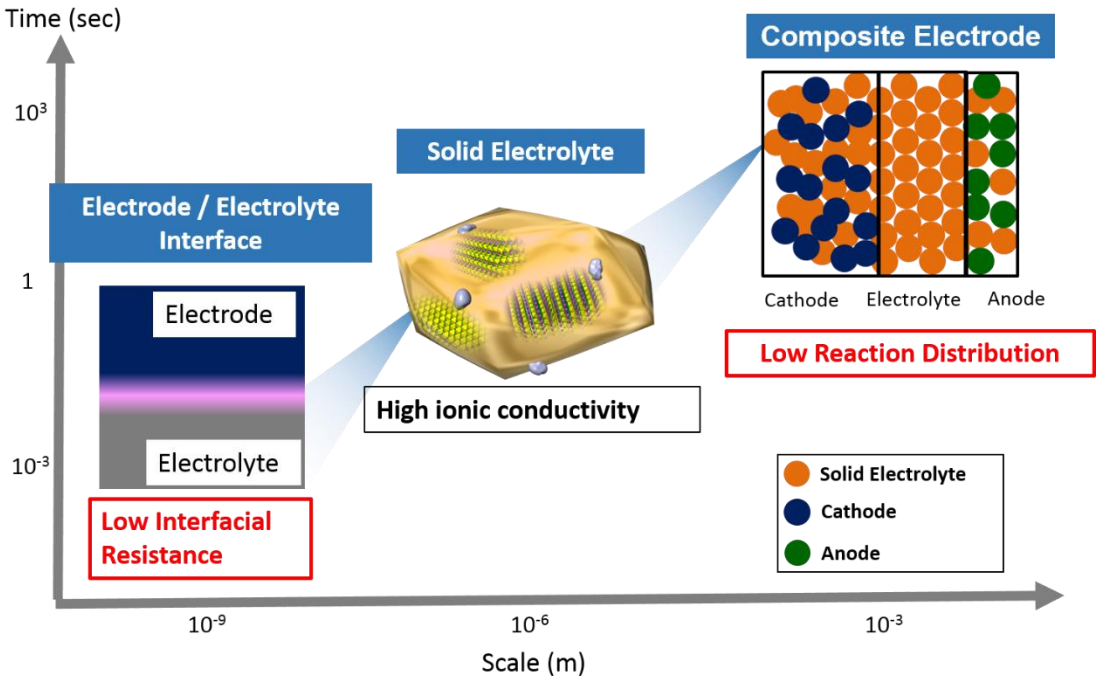

Figure 9 Limitations issues preventing application of all-solid-state batteries at different scales.

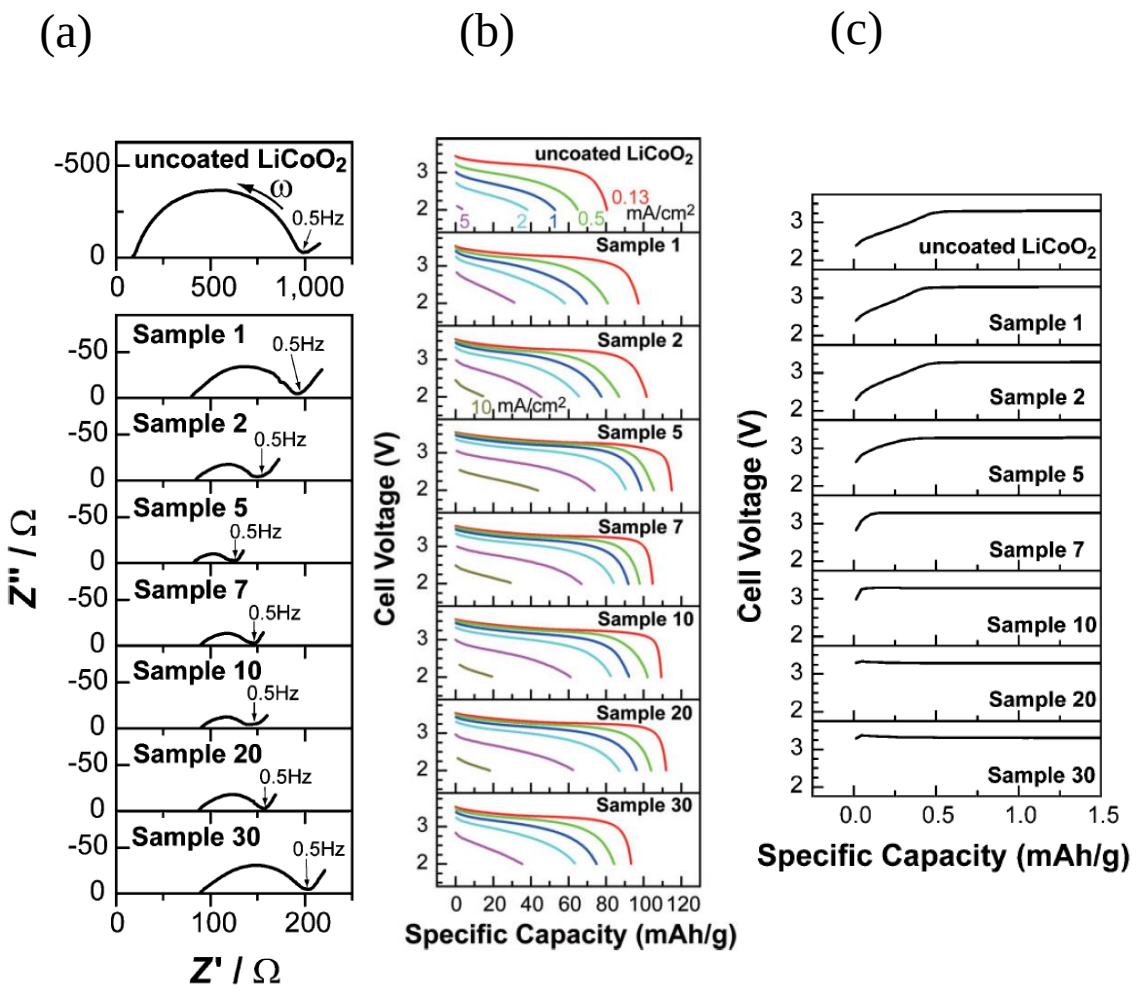

Figure 10 (a) Complex impedance plots and (b) discharge curves (c) first charge curves of uncoated In-Li/$LiCoO_2$ and coated by $Li_4Ti_5O_{12}$ with different thickness.[70]

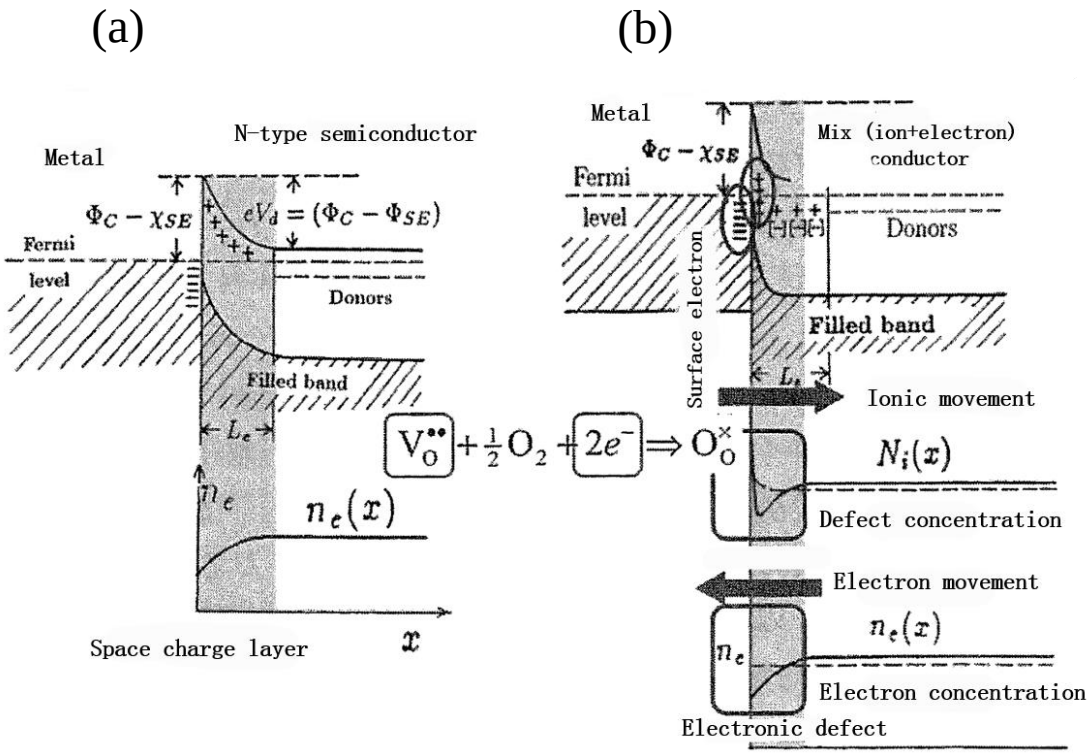

Figure 11 Schematic diagram of space charge layer (a) between metal and semiconductor, (b) between metal and mixed conductor.[72]

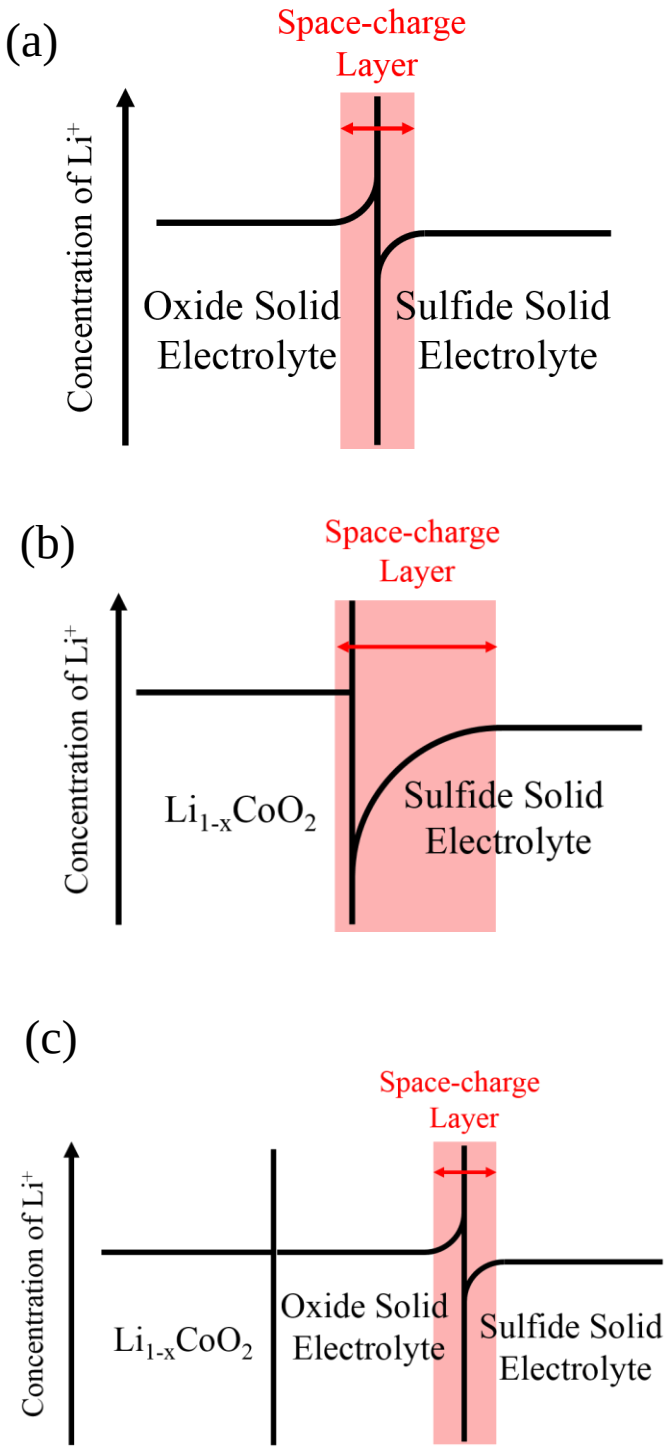

Figure 12 Schematic diagram of space charge layer at (a) oxide solid electrolyte/sulfide solid electrolyte interface, (b) cathode/sulfide solid electrolyte interface and (c) cathode/oxide solid electrolyte/sulfide solid electrolyte interface.

(a)

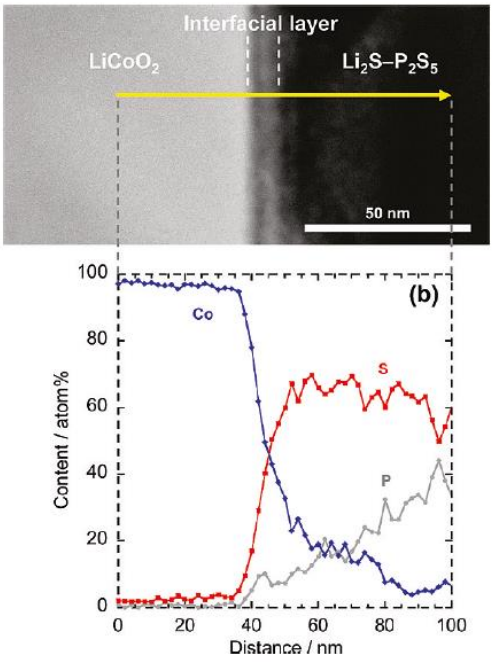

(b)

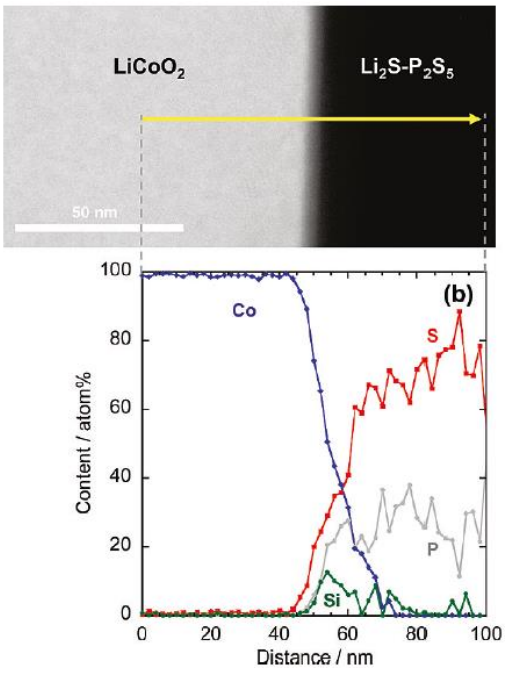

Figure 13 Cross-sectional HAADF-STEM image and EDX profile of interface of (a) $LiCoO_2/Li_2S \cdot P_2S_5$ and (b) $LiCoO_2/Li_2SiO_3/Li_2S \cdot P_2S_5$ after initial charging.[76]

(a)

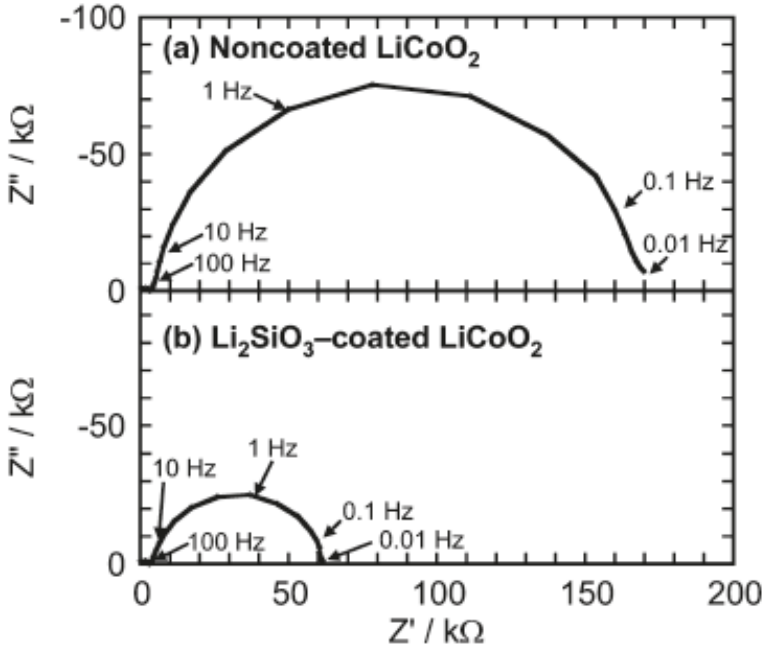

(b)

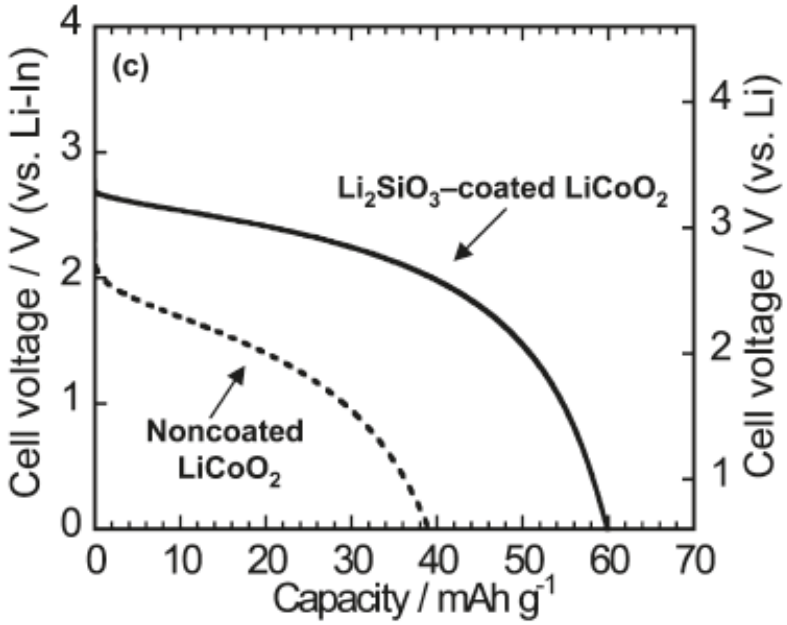

Figure 14 Impedance profiles of (a) $LiCoO_2/Li_2S\text{-}P_2S_5/In\text{-}Li$ and (b) $LiCoO_2/Li_2SiO_3/Li_2S\text{-}P_2S_5/In\text{-}Li$ at -30°C after charging to 3.6 V vs Li-In. (c) Discharge curves of the all-solid-state cells under the current density of 0.064 mA cm^{-2} at -30°C.[76]

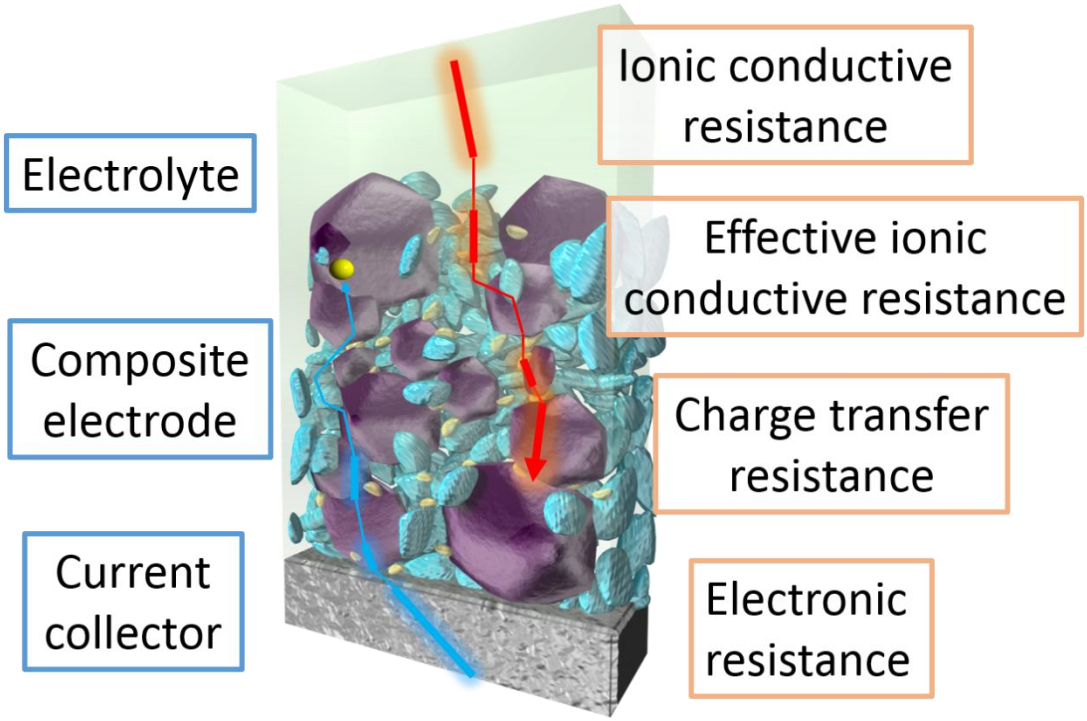

Figure 15 Schematic diagram of composite electrode.[77]

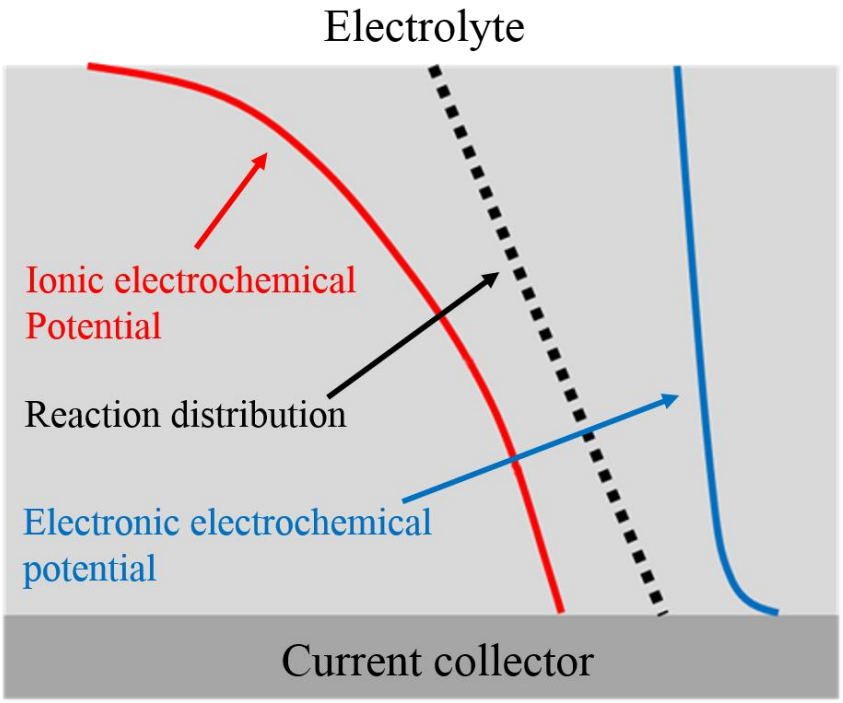

Figure 16 Ionic and electronic electrochemical potential distribution and reaction distribution in composite electrode**.**

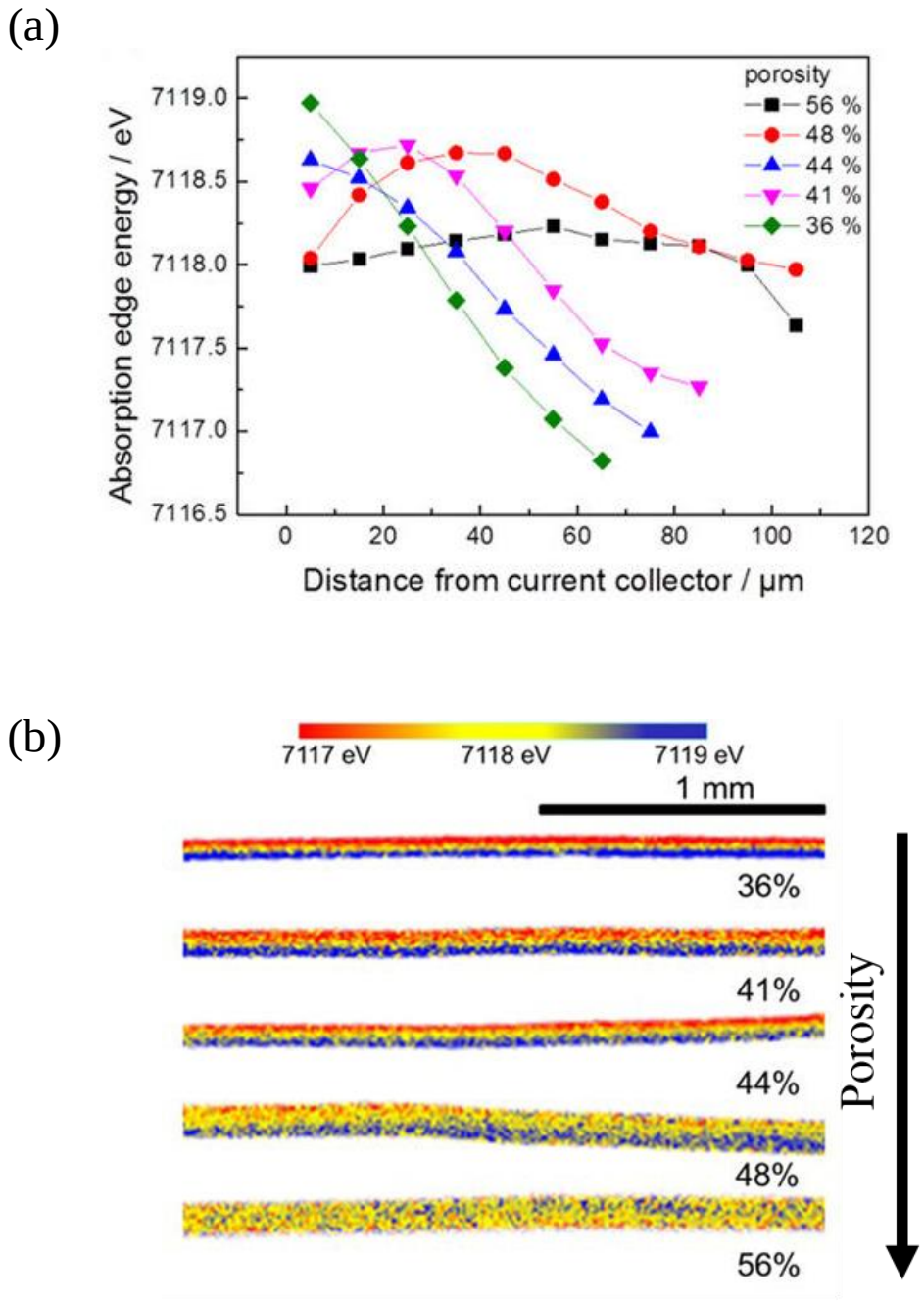

Figure 17 (a) Cross section two dimensional mapping of absorption energy at Fe *K*-edge in $LiFePO_4$ composite electrodes. Current collector is located at the bottom side. (b) Absorption edge energy as a function of distance from the current collector.[77]

Reference

(1) J. B. Goodenough and Y. Kim, *Chem. Mater.*, 2010, **22**, 587–603.

(2) J. G. Kim, B. Son, S. Mukherjee, N. Schuppert, A. Bates, O. Kwon, M. J. Choi, H. Y. Chung and S. Park, *J. Power Sources*, 2015, **282**, 299–322.

(3) K. Xu, *Chem. Rev.*, 2014, **114**, 11503–11618.

(4) V. Etacheri, R. Marom, R. Elazari, G. Salitra and D. Aurbach, *Energy Environ. Sci.* 2011, **4**, 3243-3262.

(5) E. Quartarone and P. Mustarelli, *Chem. Soc. Rev.*, 2011, **40**, 2525–2540.

(6) J. Cho, Y. W. Kim, B. K, J. G. Lee, and B. P, *Angew. Chem. Int. Ed.*, 2003, **42**, 1618-1621.

(7) A. Yamada, S. C. Chung, and K. Hinokuma, *J. Electrochem. Soc.*, 2001, **148**, A224-A229.

(8) T. Ohzuku, A. Ueda, and M. Nagayama, *J. Electrochem. Soc.*, 1993, **140**, 1862-1870.

(9) M. J. Lee, S. Lee, P. Oh, Y. Kim, and J. Cho, *Nano Lett.*., 2014, **14**, 993-999.

(10) R. Wang, X. He, L. He, F. Wang, R. Xiao, L. Gu, H. Li, and L. Chen, *Adv. Energy Mater.*, 2013, **3**, 1358-1367.

(11) F. Lin, D. Nordlund, T. C. Weng, Y. Zhu, C. Ban, R. M. Richards, and H. L. Xin, *Nat. Commun.*, 2014, 5.

(12) S. K. Martha, B. Markovsky, J. Grinblat, Y. Gofer, O. Haik, E. Zinigard, D. Aurbach, T. Drezen, D. Wang, G. Deghenghi, and I. Exnar, *J. Electrochem. Soc.*, 2009, **156**, A541-A552.

(13) M. Nagao. A. Hayashi, and M. Tatsumisago, *Energy Tech.*, 2013, **1**, 186-192.

(14) N. A. Kaskhedikar, and J. Maier, *Adv. Mater.*, 2009, **21**, 2664-2680.

(15) N. Takami, K. Hoshina, and H. Inagaki, *J. Electrochem. Soc.*, 2011, **158**, A725-A730.

(16) T. D. Hatchard, and J. R. Dahn, *J. Electrochem. Soc.*, 2004, **151**, A838-A842.

(17) L. Baggetto, and P. H. L. Notten, *J. Electrochem. Soc.*, 2009, **156**, A169-A175.

(18) I. A. Courtney, J. S. Tse, O. Mao, J. Hafner, and J. R. Dahn, *Phys. Rev. B*, 1998, **58**, 15583-15588.

(19) R. Kanno and M. Murayama, *J. Electrochem. Soc.*, 2001, **148**, A742–A746

(20) V. Thangadurai and W. Weppner, *Ionics*, 2006, **12**, 81–92.

(21) E. Quartarone and P. Mustarelli, *Chem. Soc. Rev.*, 2011, **40**, 2525–2540.

(22) H. P. Hong, *Mater. Res. Bull.*, 1978, **13**, 117–124.

(23) V. Thangadurai, S. Narayanan and D. Pinzaru, *Chem. Soc. Rev.*, 2014, **43**, 4714–4727.

(24) P. G. Bruce, *J. Electrochem. Soc.*, 1983, **130**, 662–669.

(25) R. Bouchet, S. Maria, R. Meziane, A. Aboulaich, L. Lienafa, J.-P. Bonnet, T. N. Phan, D. Bertin, D. Gigmes and D. Devaux, *Nat. Mater.*, 2013, **12**, 452–457.

(26) J. Goodenough, H. P. Hong and J. Kafalas, *Mater. Res. Bull.*, 1976, **11**, 203–220.

(27) T. Takahashi and H. Iwahara, *Energy Convers.*, 1971, **11**, 105–111.

(28) S. Breuer, D. Prutsch, Q. L. Ma, V. Epp, F. P. Pflugl, F. Tietz, M. Wilkening, *J. Mater. Chem. A*, 2015, **3**, 21343-21350.

(29) J. Fu, *Solid State Ionics*, 1997, **96**, 195–200.

(30) X. Xu, Z. Wen, X. Yang, J. Zhang and Z. Gu, *Solid State Ionics*, 2006, **177**, 2611–

2615.

(31) B. Kumar, D. Thomas and J. Kumar, *J. Electrochem. Soc.*, 2009, **156**, A506–A513.

(32) J. K. Feng, L. Lu and M. O. Lai, *J. Alloys Compd.*, 2010, **501**, 255–258.

(33) V. Thangadurai, H. Kaack and W. J. Weppner, *J. Am. Ceram. Soc.*, 2003, **86**, 437–440.

(34) V. Thangadurai and W. Weppner, *Adv. Funct. Mater.*, 2005, **15**, 107–112.

(35) M. Xu, M. S. Park, J. M. Lee, T. Y. Kim, Y. S. Park and E. Ma, *Phys. Rev. B: Condens. Matter Mater. Phys.*, 2012, **85**, 052301.

(36) E. J. Cussen, *Chem. Commun.*, 2006, 412–413.

(37) Y. Inaguma, C. Liquan, M. Itoh, T. Nakamura, T. Uchida, H. Ikuta and M. Wakihara, *Solid State Commun.*, 1993, **86**, 689–693.

(38) M. Yashima, M. Itoh, Y. Inaguma and Y. Morii, *J. Am. Chem. Soc.*, 2005, **127**, 3491–3495.

(39) S. Stramare, V. Thangadurai and W. Weppner, *Chem. Mater.*, 2003, **15**, 3974–3990.

(40) Y. Deng, C. Eames, J. N. Chotard, F. Lalere, V. Seznec, S. Emge, O. Pecher, C. P. Grey, C. Masquelier and M. S. Islam, *J. Am. Chem. Soc.*, 2015, **137**, 9136–9145.

(41) R. Mercier, J. P. Malugani, B. Fahys and G. Robert, *Solid State Ionics*, 1981, **5**, 663–666.

(42) J. H. Kennedy and Z. Zhang, *J. Electrochem. Soc.*, 1988, **135**, 859–862.

(43) A. Hayashi, S. Hama, H. Morimoto, M. Tatsumisago and T. Minami, *J. Am. Ceram. Soc.*, 2001, **84**, 477–479.

(44) T. Minami, A. Hayashi and M. Tatsumisago, *Solid State Ionics*, 2006, **177**, 2715–2720.

(45) S. S. Berbano, M. Mirsaneh, M. T. Lanagan and C. A. Randall, *Int. J. Appl. Glass Sci.*, 2013, **4**, 414–425.

(46) A. Hayashi, *J. Ceram. Soc. Jpn.*, 2007, **115**, 110–117.

(47) S. Kondo, K. Takada and Y. Yamamura, *Solid State Ionics*, 1992, **53**, 1183–1186.

(48) H. Morimoto, H. Yamashita, M. Tatsumisago and T. Minami, *J. Am. Ceram. Soc.*, 1999, **82**, 1352–1354.

(49) J. Kim, Y. Yoon, M. Eom and D. Shin, *Solid State Ionics*, 2012, **225**, 626–630.

(50) M. Tachez, J. P. Malugani, R. Mercier and G. Robert, *Solid State Ionics*, 1984, **14**, 181–185.

(51) R. Kanno, T. Hata, Y. Kawamoto and M. Irie, *Solid State Ionics*, 2000, **130**, 97–104.

(52) Y. Wang, Z. Liu, X. Zhu, Y. Tang and F. Huang, *J. Power Sources*, 2013, **224**, 225–229.

(53) A. Hayashi, K. Minami, S. Ujiie and M. Tatsumisago, *J. Non-Cryst. Solids*, 2010, **356**, 2670–2673.

(54) N. Kamaya, K. Homma, Y. Yamakawa, M. Hirayama, R. Kanno, M. Yonemura, T. Kamiyama, Y. Kato, S. Hama, K. Kawamoto and A. Mitsui, *Nat. Mater.*, 2011, **10**, 682–686.

(55) Y. Mo, S. P. Ong and G. Ceder, *Chem. Mater.*, 2012, **24**, 15–17.

(56) Y. Kato, S. Hori, T. Saito, K. Suzuki, M. Hirayama, A. Mitsui, M. Yonemura, H. Iba, R. Kanno, *Nature Energy,* 2016, **1**, 16030.

(57) B. Boukamp and R. Huggins, *Phys. Lett. A*, 1976, **58**, 231–233.

(58) M. Wolf, *J. Phys. C: Solid State Phys.*, 1984, **17**, L285–L288.

(59) H. J. Beister, S. Haag, R. Kniep, K. Strössner and K. Syassen, *Angew. Chem., Int. Ed. Engl.*, 1988, **27**, 1101–1103.

(60) W. Li, G. Wu, C. M. Araújo, R. H. Scheicher, A. Blomqvist, R. Ahuja, Z. Xiong, Y. Feng and P. Chen, *Energy Environ. Sci.*, 2010, **3**, 1524–1530.

(61) K. Iio, A. Hayashi, H. Morimoto, M. Tatsumisago and T. Minami, *Chem. Mater.*, 2002, **14**, 2444–2449.

(62) J. Bates, N. Dudney, G. Gruzalski, R. Zuhr, A. Choudhury, C. Luck and J. Robertson, *J. Power Sources*, 1993, **43**, 103–110.

(63) S. D. Jones, J. R. Akridge and F. K. Shokoohi, *Solid State Ionics*, 1994, **69**, 357–368.

(64) Y. Su, J. Falgenhauer, A. Polity, T. Leichtweiß, A. Kronenberger, J. Obel, S. Zhou, D. Schlettwein, J. Janek and B. K. Meyer, *Solid State Ionics*, 2015, **282**, 63–69.

(65) J. B. Goodenough and K. S. Park, *J. Am. Chem. Soc.*, 2013, **135**, 1167–1176.

(66) Y. S. Jung, D. Y. Oh, Y. J. Nam and K. H. Park, *Isr. J. Chem.*, 2015, **55**, 472–485.

(67) J. W. Fergus, *J. Power Sources*, 2010, **195**, 4554–4569.

(68) H. Morimoto, H. Awano, J. Terashima, Y. Shindo, S. Nakanishi, N. Ito, K. Ishikawa and S. Tobishima, *J. Power Sources*, 2013,**240**, 636–643.

(69) N. Machida, J. Kashiwagi, M. Naito, T. Shigematsu, *Solid State Ionics*, 2012, **225**, 354–358.

(70) N. Ohta, K. Takada, L. Zhang, R. Ma, M. Osada, T. Sasaki, *Adv. Mater*, 2006, **18**, 2226-2229.

(71) T. Ohzuku, A. Ueda, N. Yamamoto, *J. Electrochem. Soc.*, 1995, **142**, 1431-1435.

(72) J. Maier, *Nature Materials,* 2005, **4**, 805-815.

(73) A. L. Despotuli and V. I. Nikolaichic, *Solid State Ionics,* 1993, **60**, 275.

(74) S. Bredikhin, T. Hattori, and M. Ishigame, *Phys. Rev. B,* 1994, **50**, 2444.

(75) K. Takada, *Electrochemistry,* 2011, **4**, 270-274.

(76) A. Sakuda, A. Hayashi and M. Tatsumiago, *Chem. Mater.,* 2010, **22**, 949-956.

(77) Y. Orikasa, Y. Gogyo, H. Yamashige, M. Katayama, K. Z. Chen, T. Mori, K. Yamamoto, T. Masese, Y. Inada, T. Ohata, Z. Siroma, S. Kato, H. Kinoshita, H. Arai, Z. Ogumi and Y. Uchimoto, *Scientific Reports,* 2016, 26382.

(78) D. A. G. Bruggeman, *Annalen der Physik,* 1935, **24**, 636-664.

(79) I. V. Thorat, D. E. Stephenson, N. A. Zacharias, K. Zaghib, J. N. Harb and D. R. Wheeler, *J. Power Sources,* 2009, **188**, 592-600.

(80) T. F. Fuller, M. Doyle and J. Newman, *J. Electrochem. Soc.,* 1994, **141**, 1-10.

(81) K. C. Hess, W. K. Epting and S. Litster, *Anal. Chem.,* 2011, **83**, 9492-9498.

(82) K. C. Hess, J. F. Whitacre and S. Litster, *J. Electrochem. SOC.,* 2012, **159**, A1351-A1359.

(83) J. Liu, M. Kunz, K. Chen, N. Tamura and T. J. Richardson, *J. Phys. Chem. Lett.,* 2010, **1**, 2120-2123.

(84) M. Doyle, J. Newman, A. S. Gozdz, C. N. Schmutz and J. M. Tarascon, *J. Electrochem. Soc.,* 1996, **143**, 1890-1903.

(85) V. D. Diwakar and V. R. Subramanian, *J. Electrochem. Soc.,* 2005, **152**, A984-A988.

(86) C. Fongy, A. C. Gaillot, S. Jouanneau, D. Guyomard and B. Lestriez, *J. Electrochem. Soc.,* 2010, **7**, A885-A891.

(87) C. Fongy, S. Jouanneau, D. Guyomard, J. C. Badot and B. Lestriez, *J. Electrochem. Soc.*, 2010, **12**, A1347-A1353.

(88) S. H. Ng, F. L. Mantia and P. Novak, *Angew. Chem. Int. Ed*., 2009, **48**, 528-532.

(89) K. C. Hess, J. F. Whitacre and S. Litster, *J. Electrochem. Soc*., 2012, 159, A1351-A1359.

(90) J. Nanda, J. Remillard, A. O'Neill, D. Bernardi, T. Ro, K. E. Nietering, J. Go and T. J. Miller, *Adv. Funct. Mater.*, 2011, **21**, 3282-3290.

(91) Z. Siroma, T. Sato, T. Takeuchi, R. Nagai, A. Ota and T. Ioroi, *J. Power Sources*, 2016, **316**, 215-223.

(92) Z. Siroma, J. Hagiwara, K. Yasuda, M. Inaba and A. Tasaka, *J. Electroanal. Chem.*, 2010, **648**, 92-97.

(93) T. Nakamura, T. Watanabe, Y. Kimura, K. Amezawa, K. Nitta, H. Tanida, K. Ohara, Y. Uchimoto, Z. Ogumi, *J. Phys. Chem. C*, 2017, **121**, 2118-2124.

Chapter 1. Elucidation of the Effect of Introducing Li_3PO_4 Interlayer into $LiCoO_2/Li_2S$-P_2S_5 Interface in All-Solid-State Battery

1.1. Introduction

In recent years, rechargeable lithium-ion batteries are being widely used in applications such as portable electronic devices and electric vehicles because of their higher energy density than that of other batteries.[1-3] However, the poor safety of lithium-ion batteries due to the usage of flammable organic liquid electrolytes has become a serious concern, especially for electric vehicles.[4] It has been reported that the use of nonflammable inorganic solid electrolytes allows the fabrication of all-solid-state batteries with outstanding safety and potential for application in new battery systems.[5] Of the different kinds of lithium-ion solid electrolytes, sulfide solid electrolytes have attracted increasing attention owing to their high ionic conductivity, of the order of 10^{-3} S cm^{-1}.[6] However, the high interfacial resistance resulting from the solid-solid interface between the cathode and the electrolyte remains one of the main drawbacks of all-solid-state batteries. Since Takada *et al.* reported the effect of interface modification,[8] interface modification has been used as an effective method to minimize this interfacial resistance.[7] By introducing interlayers such as $LiNbO_3$,[8] Li_3PO_4,[9]

Li_2SiO_3,[10] $Li_4Ti_5O_{12}$,[11] ZrO_2,[12] and Al_2O_3[13] between cathodes and electrolyte, a lower interfacial resistance and better battery performance have been achieved.

Although the effects of introducing the interlayer were confirmed in the previous studies,[8-13] the mechanism responsible for the interlayer effect remains controversial. To date, two main hypotheses have been proposed as the reasons for the interfacial resistance: (1) the space-charge layer mechanism,[11] and (2) the reaction-product layer mechanism.[10] The space-charge layer has been investigated through electrochemical analyses[11] and theoretical calculations,[14] and the space-charge layer was believed to form at the interface owing to the difference in the lithium electrochemical potential between the oxide cathode and that of sulfide electrolyte. However, Haruta *et al.* reported that the space-charge layer does not cause high resistance at $LiCoO_2$/LiPON interface.[15] To investigate the reaction-product layer, X-ray photoelectron spectroscopy[16] and *in situ* scanning transmission electron microscopy coupled with electron energy loss spectroscopy[17,18] were carried out. Transmission electron microscopy coupled with energy dispersive X-ray spectrometry analyses[10] were also performed, and the reaction-product layer was considered to form at the interface owing to the mutual diffusion of elements between the cathode and electrolyte during the charge/discharge process. In order to provide information about the interfacial electronic and local structures which are very important for further discussion of the interfacial reaction mechanism, we have developed novel technique of depth-resolved X-ray absorption spectroscopic (DR-XAS) measurements[19] to analyze the effect of introducing interlayers into the cathode/oxide electrolyte interface.

In this work, we used thin-film electrodes as models to analyze the effect of introducing an interlayer to a cathode/sulfide electrolyte interface for electronic and local structures because focusing on the interfacial reaction at cathode/electrolyte in composite electrode is difficult due to the complex three-dimensional structure. $LiCoO_2$ and $80Li_2S{\cdot}20P_2S_5$ were chosen as the cathode and solid-state electrolyte, respectively. As the interlayer for interfacial modification, we chose Li_3PO_4, which has been demonstrated to be effective for the $LiCoO_2/80Li_2S{\cdot}20P_2S_5$ interface.[8] First, two types of thin-film electrodes of $LiCoO_2/80Li_2S{\cdot}20P_2S_5$ and $LiCoO_2/Li_3PO_4/80Li_2S{\cdot}20P_2S_5$ were prepared by pulsed-laser deposition (PLD). Then, their electrochemical performances were studied using cyclic voltammetry (CV) and electrochemical impedance spectroscopy (EIS). Finally, the interface statuses of both thin-film electrodes were compared before and after the charge/discharge cycle using DR-XAS measurements. Our study revealed that the Li_3PO_4 interlayer stabilizes the interfacial structure between $LiCoO_2/80Li_2S{\cdot}20P_2S_5$, which leads to a lower interfacial resistance and higher durability during the charge/discharge processes.

1.2. Experimental Section

1.2.1. Sample Preparation

Both thin-film electrodes (with and without the Li_3PO_4 interlayer) were prepared using the PLD method. The diagrammatic sketch of the thin-film model electrodes is shown in Figure 1.1. In order to avoid sulfur contamination to $LiCoO_2$ thin-film, we used two different chambers for the PLD processes. One chamber is for preparation for

$LiCoO_2$ thin film, and the other chamber is for preparation for Li_3PO_4 and $80Li_2S{\cdot}20P_2S_5$ thin films. To supply a sufficient amount of Li during PLD deposition, the PLD targets for $LiCoO_2$ thin films consisted of $LiCoO_2$ (Sigma-Aldrich Co., LLC) with 15 wt% Li_2O (Sigma-Aldrich Co., LLC.). The targets were sintered at 773 K for 6 h. The $LiCoO_2$ thin films were deposited on mirror-polished polycrystalline platinum substrates (15 mm × 15 mm × 2 mm) under an oxygen pressure of 0.01 Pa for 30 min. The substrates were heated and maintained at a temperature of 873 K. A Nd:YAG laser (λ = 266 nm) with a repeating frequency of 10 Hz was used for laser ablation. The laser energy density was set to 3.5 J cm^{-2} at the target.[20] Then, the prepared $LiCoO_2$ thin-film was transported to the other chamber and annealed at 300°C for 2 h under argon atmosphere. Li_3PO_4 and $80Li_2S{\cdot}20P_2S_5$ were deposited on the $LiCoO_2$ thin-film in the other chamber. The PLD target for Li_3PO_4 interlayers was prepared by sintering Li_3PO_4 (98%, Wako Pure Chemical Industries Ltd.) at 873 K for 6 h. The Li_3PO_4 thin films were deposited on the $LiCoO_2$ films at room temperature under an argon pressure of 0.01 Pa for 120 s. A KrF excimer laser (λ = 248 nm) with a repeating frequency of 5 Hz was used for laser ablation. The laser energy density was set to 2 J cm^{-2} at the target.[21] The PLD target for the $80Li_2S{\cdot}\ 20P_2S_5$ layer consisted of Li_2S (99.9%, Idemitsu Kosan Co. Ltd.) and P_2S_5 (99%, Aldrich Chemical Co., Inc.) with a molar ratio of 80:20. The $80Li_2S{\cdot}20P_2S_5$ thin films were deposited on $LiCoO_2$ films or the Li_3PO_4 interlayer at room temperature under an argon pressure of 5 Pa for 140 s. A KrF excimer laser (λ = 266 nm) with a repeating frequency of 10 Hz was used for laser ablation. The laser energy density was set to 2 J cm^{-2} at the target.[22] The Li_3PO_4 protective layer was

deposited on the $80Li_2S \cdot 20P_2S_5$ thin film at room temperature under an argon pressure of 0.01 Pa for 140 s.

1.2.2. Electrochemical Measurement

CV was carried out for thin-film electrodes with and without the Li_3PO_4 interlayer by using a three-electrode cell. The thin-film electrode was used as a working electrode. Lithium metals were used as both the counter electrode and reference electrode. To understand the reaction mechanism between the cathode and solid electrolyte, the cell was simplified using the liquid electrolyte 1 M $LiClO_4$ in propylene carbonate to minimize the influence of the interface between the anode and solid electrolyte (Figure 1.2). The Li_3PO_4 protective layers were deposited on the top to prevent the dissolution of $80Li_2S \cdot 20P_2S_5$ into liquid electrolyte. The CV measurement was carried out for 10 cycles from 3.2 V to 4.4 V at a sweep speed of 0.1 mV s^{-1}. Then, only for the 1st cycle of the CV measurement, the sweep-start potential is the open-circuit potential of the cathode. To investigate the change of the interfacial resistance during charge/discharge process, EIS was carried out using the same cell configuration as in the CV measurement for four cycles. The procedure of the EIS measurements was shown in Figure 1.3. The potential was swept in the region between 3.2 V and 4.4 V with sweeping rate of 0.1 mV/sec. The EIS measurements were carried out at 3.2 V and at each potential by 0.1 V in the potential region between 3.6 V and 4.4 V during charge/discharge processes. The potential was kept at the target potential for 30 min before EIS measurements to wait for the charge or discharge current to decrease to a

constant value. The amplitude of the EIS measurements was 30 mV and the frequency range was set from 10^{-2} Hz to 10^{6} Hz.

1.2.3. Depth-Resolved X-Ray Absorption Spectroscopy Measurement

To compare the change in the interface before and after the charge/discharge process, thin-film electrodes both with and without an interlayer were analyzed by DR-XAS at two measurement points: (1) before the 1st cycle of CV measurement and (2) after the 1st cycle of CV measurement. The thin-films after the 1st cycle of the CV measurement were the one charged from an open-circuit potential to 4.4 V Li/Li^{+}, and then discharged to 3.2 V vs Li/Li^{+}. DR-XAS measurements of the Co *K*-edge in the $LiCoO_2$ cathode were obtained in BL37XU (SPring-8, Japan) using a two-dimensional pixel-array detector, Pilatus (Dectris Ltd.), to determine the exit X-ray fluorescence. After the charge/discharge process, thin-film electrodes were taken from the three-electrode cells, washed by PC, dried, and then installed into a specially made cell that can be vacuumed to 10^{-3} Pa and transmitted via incident and exit X-rays. All of the above-mentioned operations were carried out in glovebox with argon protective atmosphere.

1.3. Results and Discussion

1.3.1. Electrochemical Measurement

The CV curves (1st cycle) of both thin-film electrodes are shown in Figure 1.4. The subsequent cycles of CV curves are shown in Figure 1.5. The anodic and cathodic peaks corresponding to the first-order phase transition between two hexagonal phases of $LiCoO_2$ were detected at 3.9 V. Two more pairs of reversible redox peaks were observed at 4.07 V and 4.17 V, which represent lithium-ion diffusion during phase transition between the hexagonal and monoclinic phases of $LiCoO_2$.[23,24] Compared to the thin-film electrode with the Li_3PO_4 interlayer, the CV curve (1st cycle) of the thin-film electrode without the Li_3PO_4 interlayer showed a broad current peak around 3.2 V (the inset figure in Figure 1.4). Because $LiCoO_2$ does not exhibit insertion/extraction reactions of lithium ion around 3.2 V, this current peak may be caused by the reaction between the cathode and solid electrolyte.

The discharge capacities of both thin-film electrodes based on CV measurements are plotted against the cycle number in Figure 1.6. The discharge capacity of the thin-film electrode without the Li_3PO_4 interlayer gradually decreased from 5.4 to 4.9 mC during repeated cycling (2nd–10th cycle). In contrast, the thin-film electrode with the Li_3PO_4 interlayer kept an almost constant discharge capacity of about 6.0 mC. The thickness of the prepared $LiCoO_2$ thin-film was approximately 50 nm because we prepared for the thin-film in the same condition as our previous report.[25] We estimated the weight of $LiCoO_2$ as 9.7×10^{-6} g from the film-thickness (50 nm), the geometrical

reaction area (0.38 cm^2) and the bulk density of $LiCoO_2$ (5.05 g/cm^3), respectively. The discharge capacity of the $LiCoO_2$ thin-film without interlayer was 5.4 mC at 4.4 V, which corresponds to 155 mAh/g. The discharge of the $LiCoO_2$ thin-film with interlayer was 6.0 mC at 4.4 V, which corresponds to 172 mAh/g. Thin-film electrodes with Li_3PO_4 interlayers showed higher discharge capacities than those without the interlayer. These results indicate that the interface modification with the Li_3PO_4 interlayer can improve the cyclability of $LiCoO_2$ cathodes when using $80Li_2S \cdot 20P_2S_5$ solid electrolyte.

The interfacial resistance between the cathode and solid electrolyte during the charge/discharge process was examined by performing EIS measurements. The Nyquist plots of the charge process in the 1st CV cycle are shown in Figure 1.7. The equivalent circuit for the EIS fitting and fitting sample is shown in Figure 1.8. Comparing the change of the interfacial resistance during the charge/discharge process, interfacial resistance values at 3.9 V, 4.0 V, 4.1 V, 4.2 V, 4.3 V, and 4.4 V (vs Li/Li^+) from the 1st to the 4th cycles are plotted in Figure 1.9. The change of interfacial resistance in a single cycle was in accordance with the previous report.[26]

The interfacial resistance of the thin-film electrode without the interlayer was lower than that of the thin-film electrode with the interlayer at the initial state. However, the interfacial resistance of the thin-film electrode without the interlayer became higher during the 1st cycle. Then the resistance increased in subsequent charge/discharge processes, and increased significantly in the 4th cycle. Although the resistance of the thin-film with the interlayer was higher owing to the presence of the Li_3PO_4 interlayer

at the initial state, it remained nearly constant at about 250 Ω cm^{-2} during charge/discharge processes. These results indicate that the introduction of the Li_3PO_4 interlayer can limit the increase of the interfacial resistance during the charge/discharge process. From the results of both CV and EIS measurement, it can be concluded that interfacial modification by the Li_3PO_4 interlayer can maintain a more stable interface between the $LiCoO_2$ cathode and $80Li_2S{\cdot}20P_2S_5$ solid electrolyte.

1.3.2. Depth-Resolved X-Ray Absorption Spectroscopy Measurement

In order to investigate the electronic and local structures of the cathode/electrolyte interface before and after the charge/discharge process, cobalt ions in the cathode were analyzed by DR-XAS for the Co *K*-edge.[19] In the DR-XAS measurement, which has a depth resolution of about 3 nm, XAS spectra obtained at lower exit angles provide more information about the surface of a thin film, while XAS spectra obtained at higher exit angles provide more information about the bulk properties(Figure 1.10).[29] The X-ray near-edge fine structure (XANES) spectra of both thin-film electrodes measured before and after the charge/discharge process are shown in Figure 1.11. The observed absorption edge feature is attributed to a transition from a Co 1*s* orbital to Co 4*p* orbital.[27,28] In general, an energy shift of the absorption edge toward lower energy means that the oxidation state of the ions decreased. For a clearer view, the energy shift from the XANES spectrum of bulk (exit angle = 0.438°) to the XANES spectrum obtained from each exit angle was calculated at half of the normalized absorbance. The

energy shift of the XANES spectrum of the thin-film electrodes before 1st cycle of CV without and with interlayer are plotted against the exit angle in Figure 1.12. Before the charge process, both types of thin-film electrodes showed an energy shift toward lower energy at a lower exit angle. The energy shift of the thin-film electrode with the interlayer was smaller than that of the thin-film electrode without the interlayer. These results indicate that Co ions near the interface for both the electrodes reduced at the cathode/electrolyte interface before the charge process and the degree of the reduction was suppressed with the interlayer.

The energy shift of the XANES spectrum of both thin-film electrodes before and after the 1st cycle of CV measurement is also plotted against the exit angle in Figure 1.13. After the 1st cycle of the CV measurement, the thin-film electrode without the interlayer showed an intense energy shift toward lower energy near the interface. Meanwhile, the energy shift of the thin-film electrode with the interlayer remained almost unchanged. These results indicate that the Co ions near the interface between $LiCoO_2$ and $80Li_2S{\cdot}20P_2S_5$ reduced after the charge/discharge process, and the interlayer can suppress the reduction of the Co ions through the charge/discharge process.

The refined interatomic distance and Debye-Waller (DW) factor for the Co-O bands derived from extended X-ray absorption fine structure (EXAFS) in both thin-films electrodes before and after the 1st cycle of CV measurement were calculated from k = 4 to 12 $Å^{-1}$ range. The k^3-weighted EXAFS oscillation and the curve fitting of the

EXAFS oscillations of both thin-film electrodes before and after the 1st cycle of CV measurement are plotted in Figure 1.14, Figure 1.15, Figure 1.16, and Figure 1.17. The radial-structure functions of the local atomic environments around Co atoms show two peaks at 1.5 Å and 2.6 Å, which correspond to the six-coordinated Co-O bonds in CoO_6 octahedra and six-coordinated Co-Co interactions along the CoO_2 layer, respectively.[28] The distance and DW factor of the Co-O bonds in both thin-film electrodes are plotted against the exit angle in Figure 1.18 and Figure 1.19. The DW factor corresponds to static local distortion. In the EXAFS analysis, the standard error of the Co-O distance is less than 0.012 Å, and that of the Co-O DW factor is less than 0.020 Å. Although the depth-resolved EXAFS analysis includes relatively large standard errors, one can discuss the tendencies of the Co-O distance and DW factor from the bulk to the interface.[29]

For the thin-film without the interlayer, the Co-O distance near the interface was shorter than the distance of the bulk before the 1st cycle of the CV measurement. After the 1st cycle of the CV measurement, the Co-O distance near the interface expanded and became almost the same as the distance of the bulk. The DW factor of Co-O bonds near the interface was higher than that of the bulk before the 1st cycle of CV measurement. The DW factor did not change after the 1st cycle of CV measurement. For the thin film with the interlayer, no significant difference was observed in the distance and DW factor of the Co-O bonds between the region near the interface and the bulk before the 1st cycle of CV measurement. Even after the 1st cycle of the CV measurement, these parameters remained unchanged.

These results indicate that the local structure around Co ions is different from the interface to the bulk before the 1st cycle of the CV measurement, and changed near the interface after the 1st cycle of the CV measurement. The Li_3PO_4 interlayer can limit the change in the local structure around the Co ions near the interface of the cathode before the 1st cycle of CV measurement, and it can also maintain a stable interface during the charge/discharge process.

1.3.3. Effect of Li_3PO_4 Interlayer

The results from the DR-XAS and electrochemical measurements show that the introduction of the Li_3PO_4 interlayer stabilizes the electronic and local structures at the $LiCoO_2$/$80Li_2S{\cdot}20P_2S_5$ interface during the charge/discharge processes and also improves the electrochemical performance. The mechanism of improvement realized by introducing the Li_3PO_4 interlayer can be explained from the perspective of the suppression of the reaction between the cathode and the electrolyte at the interface by the electrochemical potential gap between $LiCoO_2$ and $80Li_2S{\cdot}20P_2S_5$.

The potential gap between $LiCoO_2$ and $80Li_2S{\cdot}20P_2S_5$ is large to cause the reaction between the cathode and the electrolyte at the interface before charge/discharge processes. The interfacial structure change between the cathode and electrolyte in the initial state, which is caused by the electrochemical potential gap, has been reported previously.[11] However, in the thin-film with the interlayer, the Li_3PO_4 compensates the potential gap between $LiCoO_2$ and $80Li_2S{\cdot}20P_2S_5$, which suppresses the reaction between the cathode and the electrolyte at the interface. Therefore, the change in the

electronic and local structures near the interface in the thin film with the interlayer is smaller than that in the thin film without the interlayer.

In the thin film without the interlayer, the interfacial resistance increased after the 1st cycling of the CV measurement. In addition, the electronic and local structures around Co ions near the interface drastically changed. According to the TEM observation of the interface,[10] the reaction of the sulfide solid electrolyte will lead to a mutual diffusion of elements S, P, and Co through the interface to form a reaction product layer. By first-principles calculation, the reaction product is believed to be the compound containing CoS_2.[30] Figure 1.13 and 1.18 show that the edge energy of Co *K*-edge XANES shift to lower energy and the distance Co-O bond distance increase near the interface in the thin-film without the interlayer after the 1st cycling. The edge energy of Co *K*-edge XANES of CoS_2 is lower than that of $LiCoO_2$, because of high covalence of Co-S bond and Co-S bond length in CoS_2 is 2.34 Å that is larger than that of $LiCoO_2$.[31]

The XANES shift toward low energy and the Co-O bond distance increase near the interface in the thin-film without the interlayer could be explained by the formation of CoS_2. The formed CoS_2 on the interface should increase the interfacial resistance during the 1st potential cycling. In the subsequent charge/discharge processes, the interfacial resistance gradually increased and then rapidly increased after a few cycles. This behavior implies that the reaction product forms at the partial area on the interface during initial charge/discharge processes, and then the formation area expanded at the

entire interface after the subsequent charge/discharge process (Figure 1.20(a)). The behavior may also imply the rate difference between the CoS_2 nucleation and the growth from CoS_2 nuclear. The formation of the reaction product layer continuously consumes the Co ion in the cathode near the interface, decreasing the discharge capacity during the charge process.

In the case of the thin-film with the interlayer (Figure 1.20(b)), no reaction was observed in the early stage during the charge process, and the interfacial resistance remained constant after the 1st cycling of the CV measurement. In addition, the change in the electronic and local structures around Co ions near the interface was suppressed. Compared to the sulfide solid electrolyte, Li_3PO_4 has a wider electrochemical window (0.69–4.21 V vs. Li/Li^+) and higher thermodynamic stability in the operation voltage range of $LiCoO_2$.[30,32] Because the thermodynamically stable Li_3PO_4 interlayer compensates for the potential gap between $LiCoO_2$ and $80Li_2S{\cdot}20P_2S_5$, the reaction between $LiCoO_2$ and $80Li_2S{\cdot}20P_2S_5$ is suppressed, which leads to a lower interfacial resistance and better battery performance.

1.4. Conclusion

Thin-film model electrodes were fabricated using the PLD method, and the well-defined cathode/electrolyte ($LiCoO_2/80Li_2S{\cdot}20P_2S_5$) interfaces were investigated by performing both electrochemical and DR-XAS measurements. The introduction of the Li_3PO_4 interlayer improved the cyclability and decreased the interfacial resistance, which led to a better cell performance. The effect of the Li_3PO_4 interlayer is attributed

to its wider electrochemical window and higher thermodynamic stability than that of sulfide electrolyte within the operation voltage range of $LiCoO_2$. The Li_3PO_4 interlayer can suppress the reaction of sulfide electrolyte and limit the formation of the irreversible reaction-product layer during cell cycling. Our study provides a new perspective for the analysis of the cathode/sulfide electrolyte solid–solid interface, and offers valuable information that would help in selecting an appropriate interlayer material to design a better all solid-state battery.

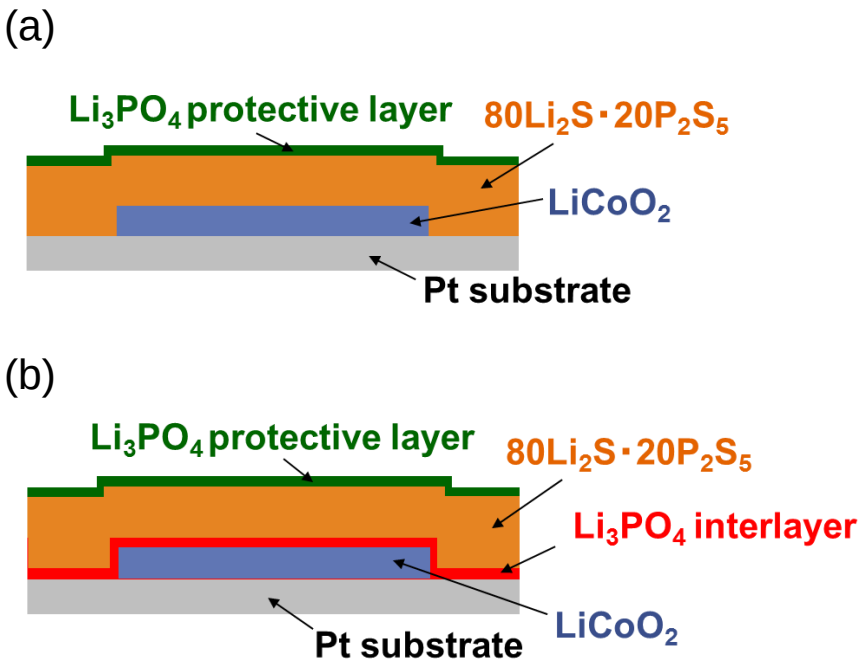

Figure 1.1 Diagrammatic sketch of thin-film model electrodes (a) without and (b) with Li_3PO_4 interlayer.

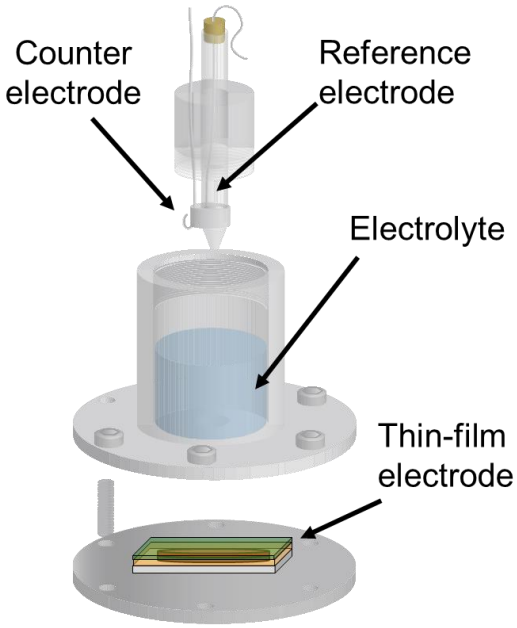

Figure 1.2 Diagrammatic sketch of the three-electrode cell used for electrochemical measurement.

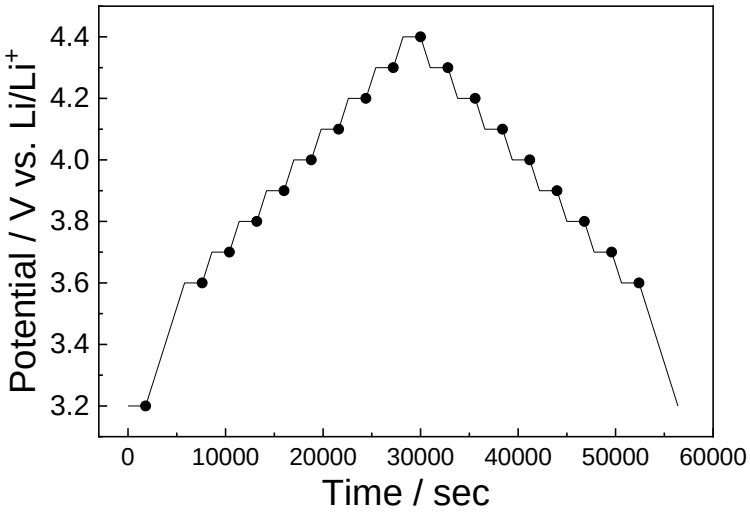

Figure 1.3 The procedure of the EIS measurements. The potential was swept in the region between 3.2 V and 4.4 V with sweeping rate of 0.1 mV/sec. The EIS measurements were carried out at 3.2 V and at each potential by 0.1 V in the potential region between 3.6 V and 4.4 V during charge/discharge processes. The potential was kept at the target potential for 30 min before EIS measurements. The circles exhibit the measurement points.

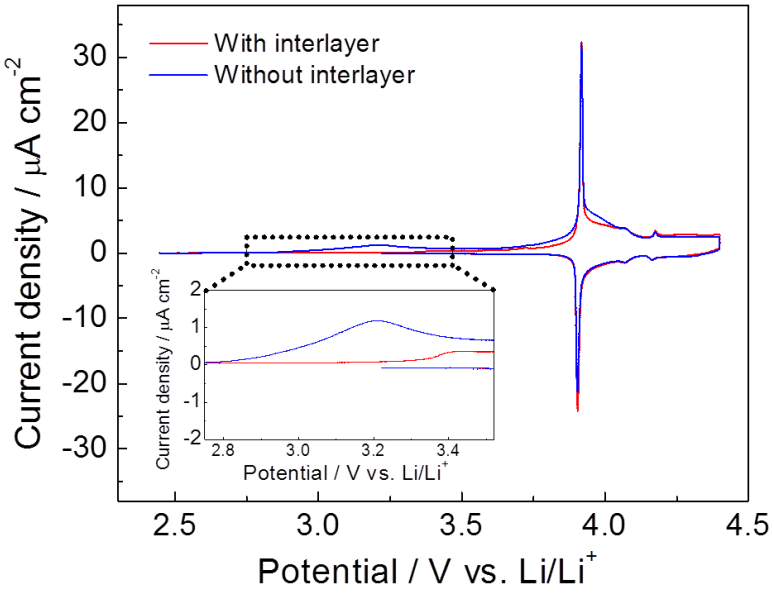

Figure 1.4 First cycle of CV curves for $LiCoO_2/80Li_2S{\cdot}20P_2S_5$ thin-films without and with the Li_3PO_4 interlayer at 298 K. The potential sweeping rate was 0.1 mV/sec. The inset figure is the enlarged figure the potential range between open circuit potential and 4.4 V.

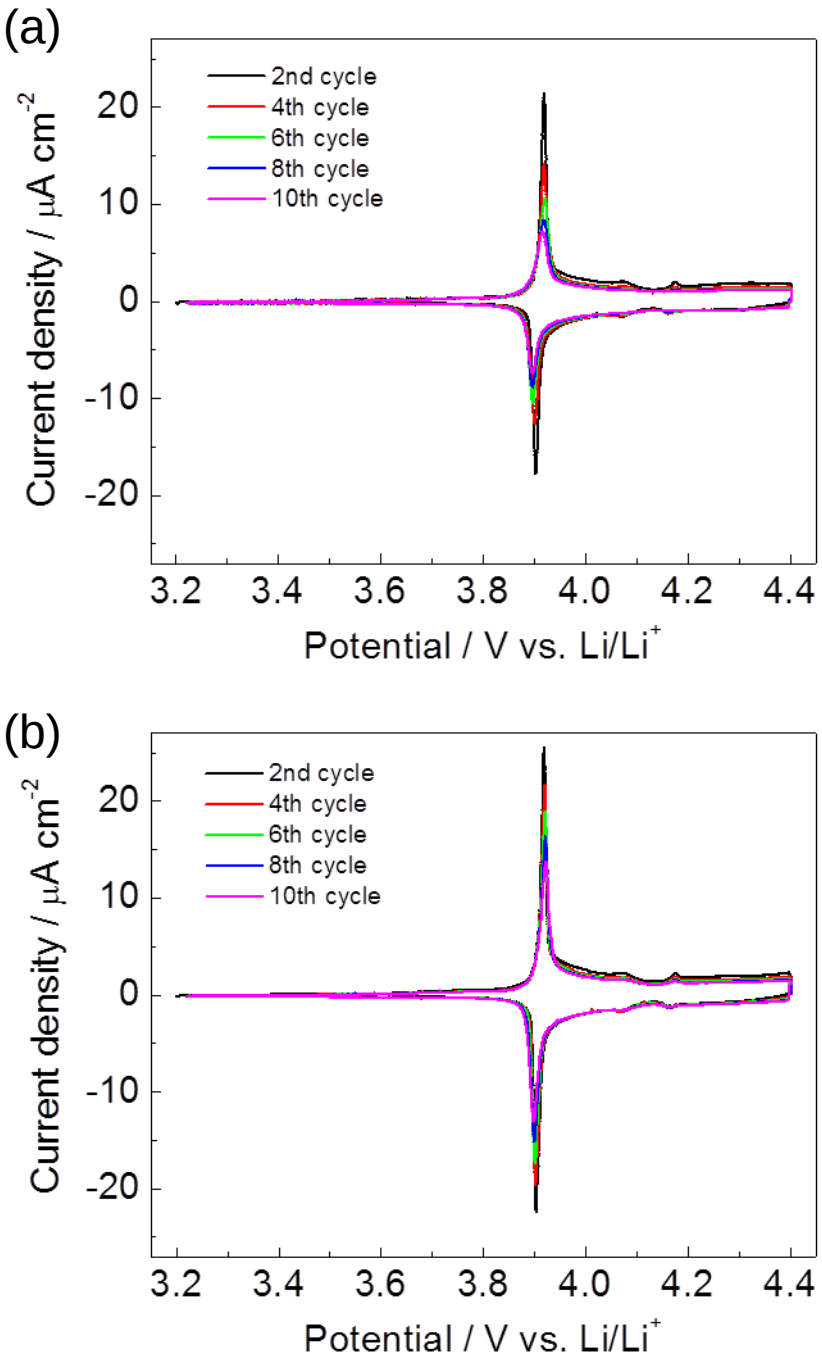

Figure 1.5 CV curves from 2nd cycle to 10th cycle for $LiCoO_2/80Li_2S{\cdot}20P_2S_5$ thin-films (a) without and (b) with the Li_3PO_4 interlayer at 298 K. The potential sweeping rate was 0.1 mV/sec. The potential range was between 3.2 V and 4.4 V

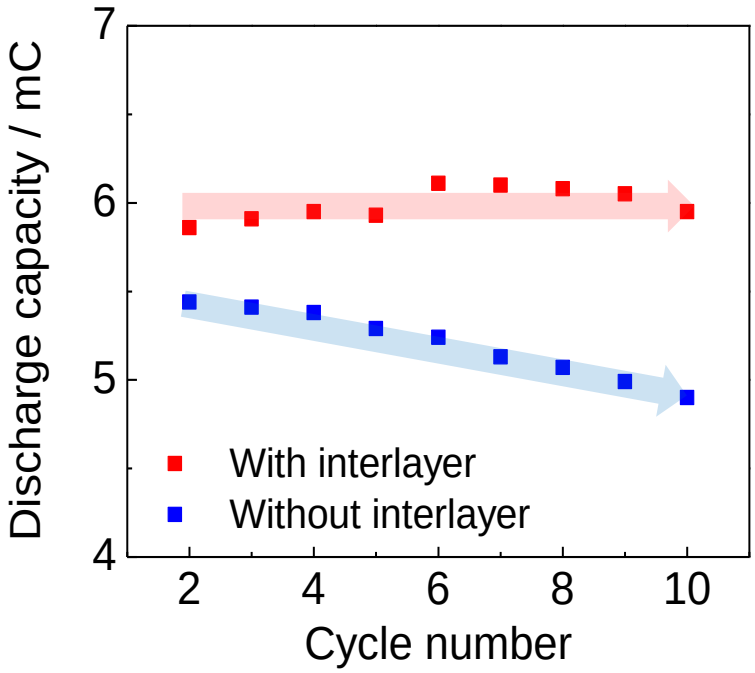

Figure 1.6 Discharge capacity estimated from CV measurements of the thin-film electrodes without and with the Li_3PO_4 interlayer.

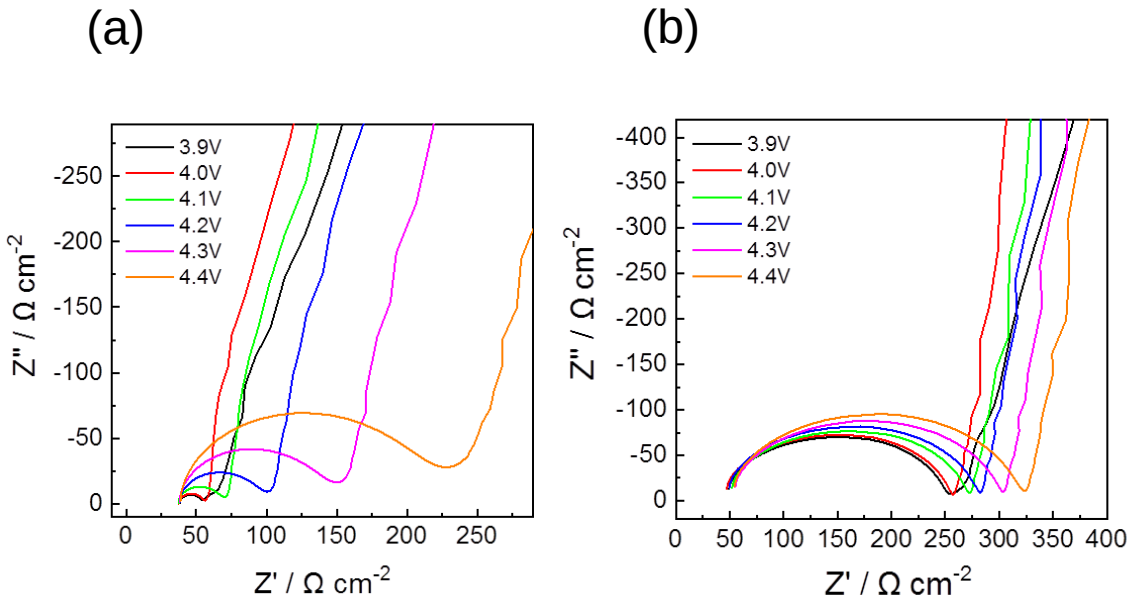

Figure 1.7 Nyquist plots of thin-film electrode (a) without and (b) with interlayer at 3.9 V, 4.0 V, 4.1 V, 4.2 V, 4.3 V and 4.4 V during the charge process in the 1st cycle of CV measurement. The potential sweeping rate was 0.1 mV/sec.

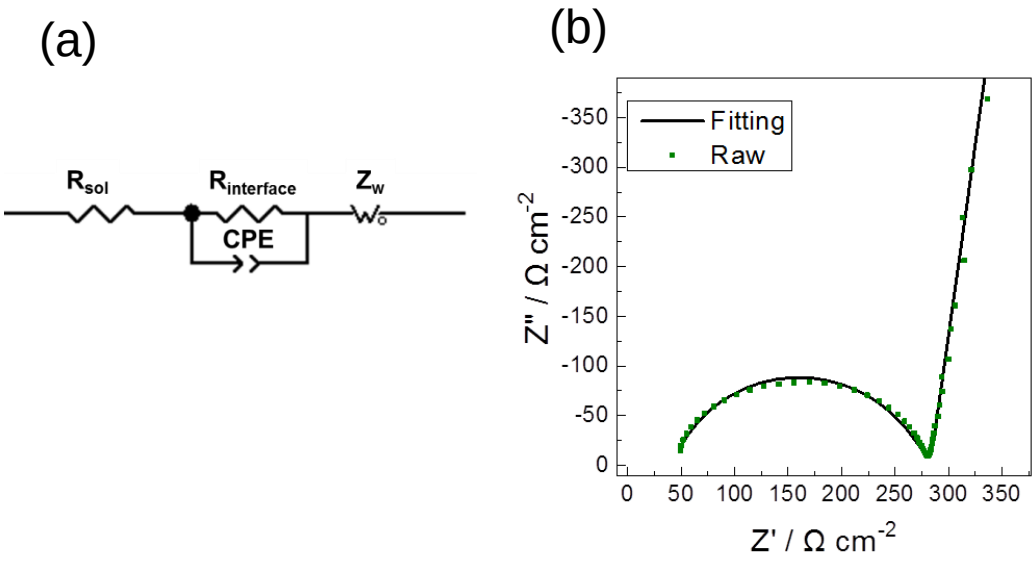

Figure 1.8 (a) Equivalent circuit for EIS fitting and (b) fitting result for 4.2 V during the charge process in the 1st cycle of CV measurement.

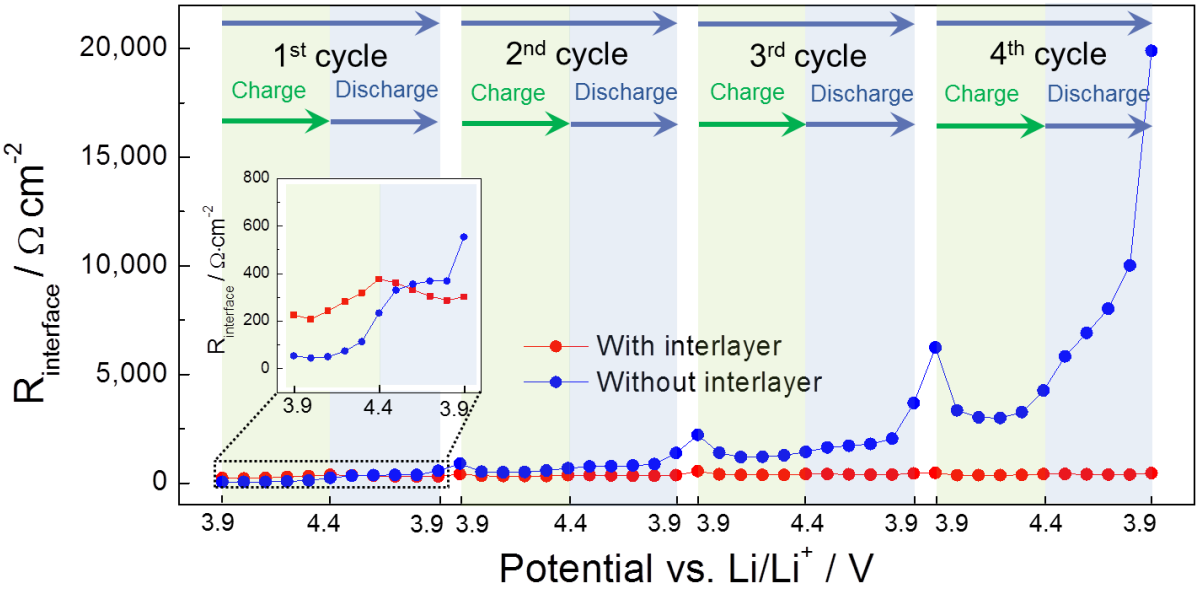

Figure 1.9 Potential-dependent interfacial resistance of the thin-film electrodes without and with the interlayer from the 1st cycle to the 4th cycle at 298 K. The sweeping potential range was between 3.2 V and 4.4 V. The resistance was measured every 0.1 V between 3.9 V and 4.4 V.

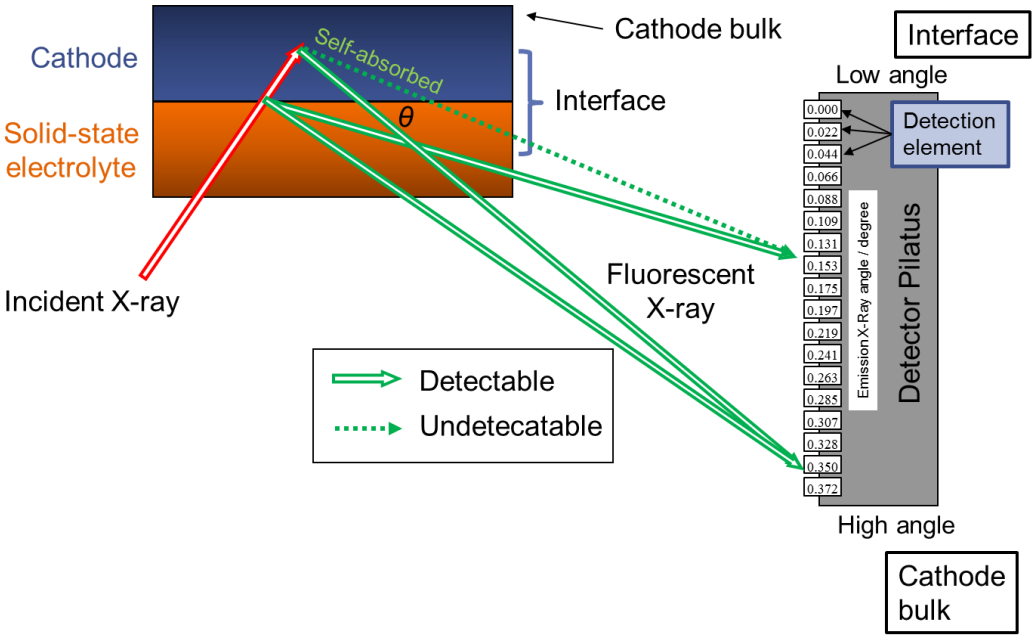

Figure 1.10 Schematic diagram of DR-XAS measurement. Because of the self-absorbed effect, the fluorescent X-ray from deeper place of the cathode cannot be detected by detection element at low angle.

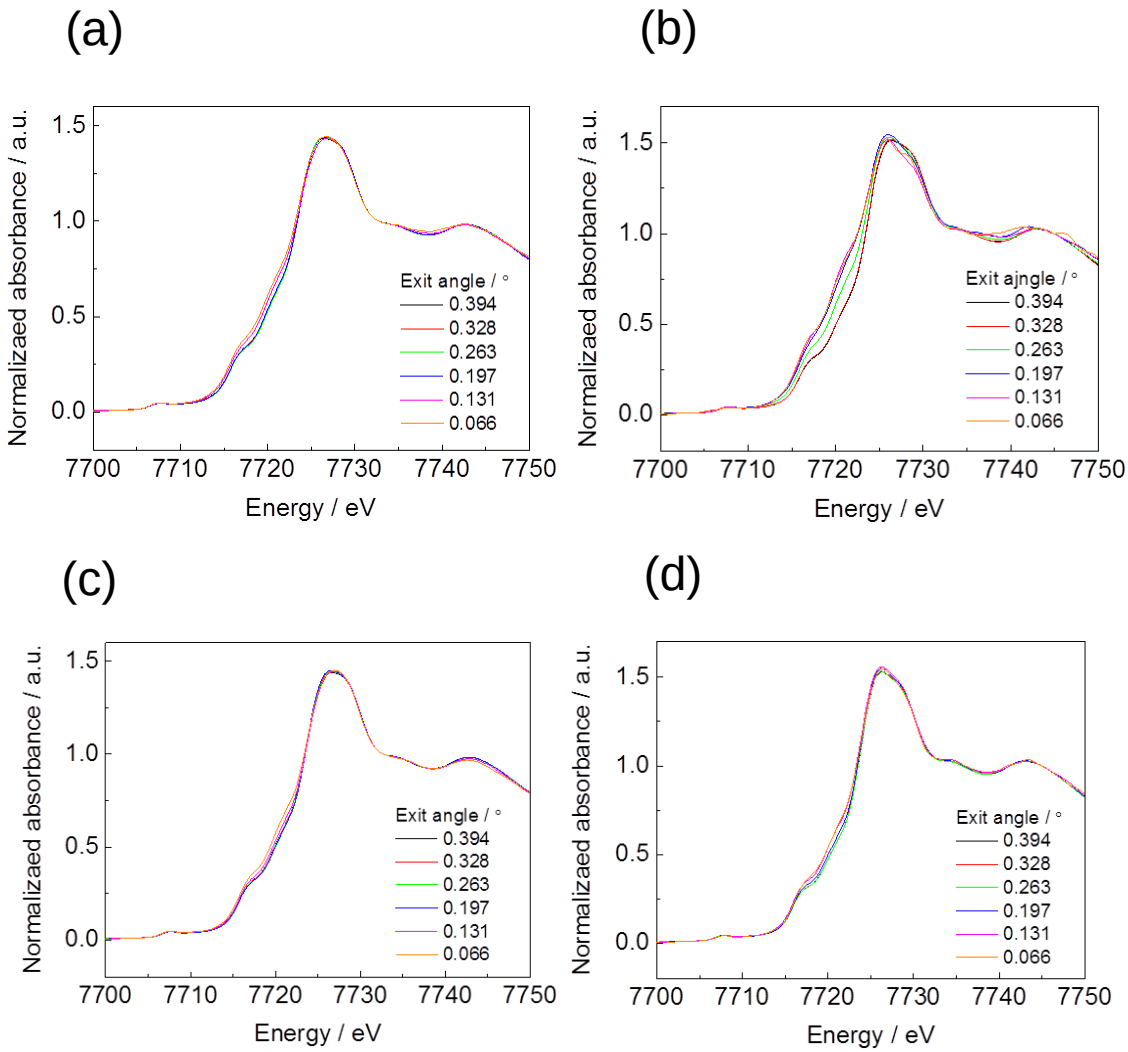

Figure 1.11 XANES spectra of two types of thin-film electrodes measured (a) before 1st cycle of CV measurement without interlayer (b) after 1st cycle of CV measurement without interlayer (c) before 1st cycle of CV measurement with interlayer (d) after 1st cycle of CV measurement with interlayer.

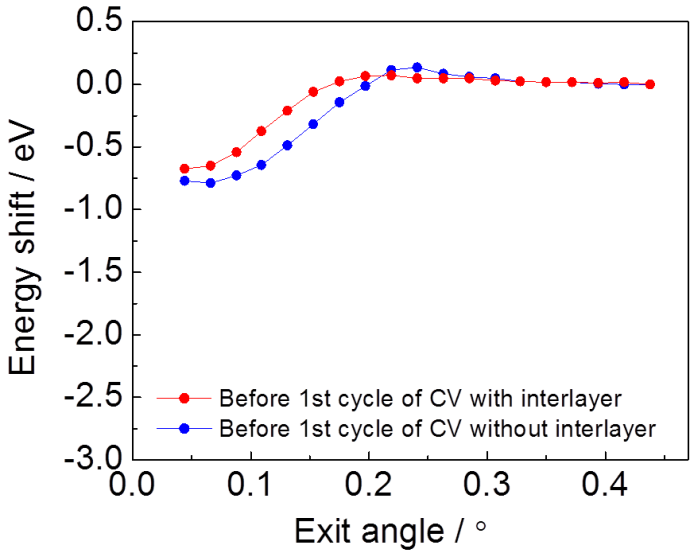

Figure 1.12 Energy shift at half of the normalized absorbance of XANES spectra from different exit angle for the thin-film electrodes without and with the interlayer before 1st cycle of CV measurement.

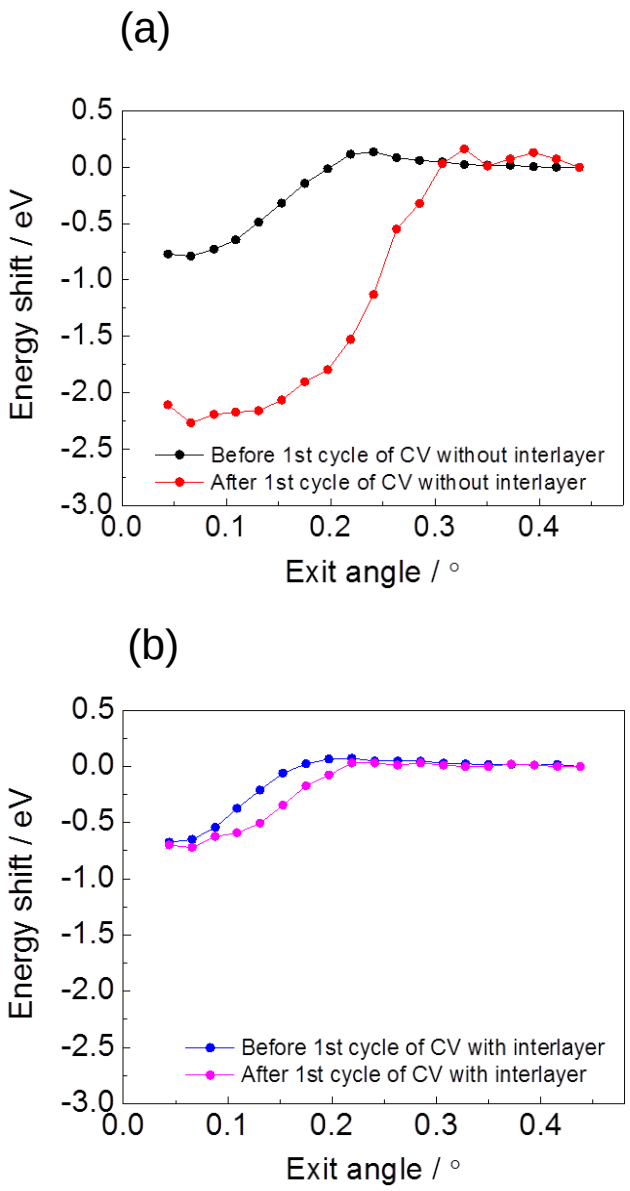

Figure 1.13 Energy shift at half of the normalized absorbance of XANES spectra from different exit angle for the thin-film electrodes (a) without and (b) with the interlayer before and after 1st cycle of CV measurement.

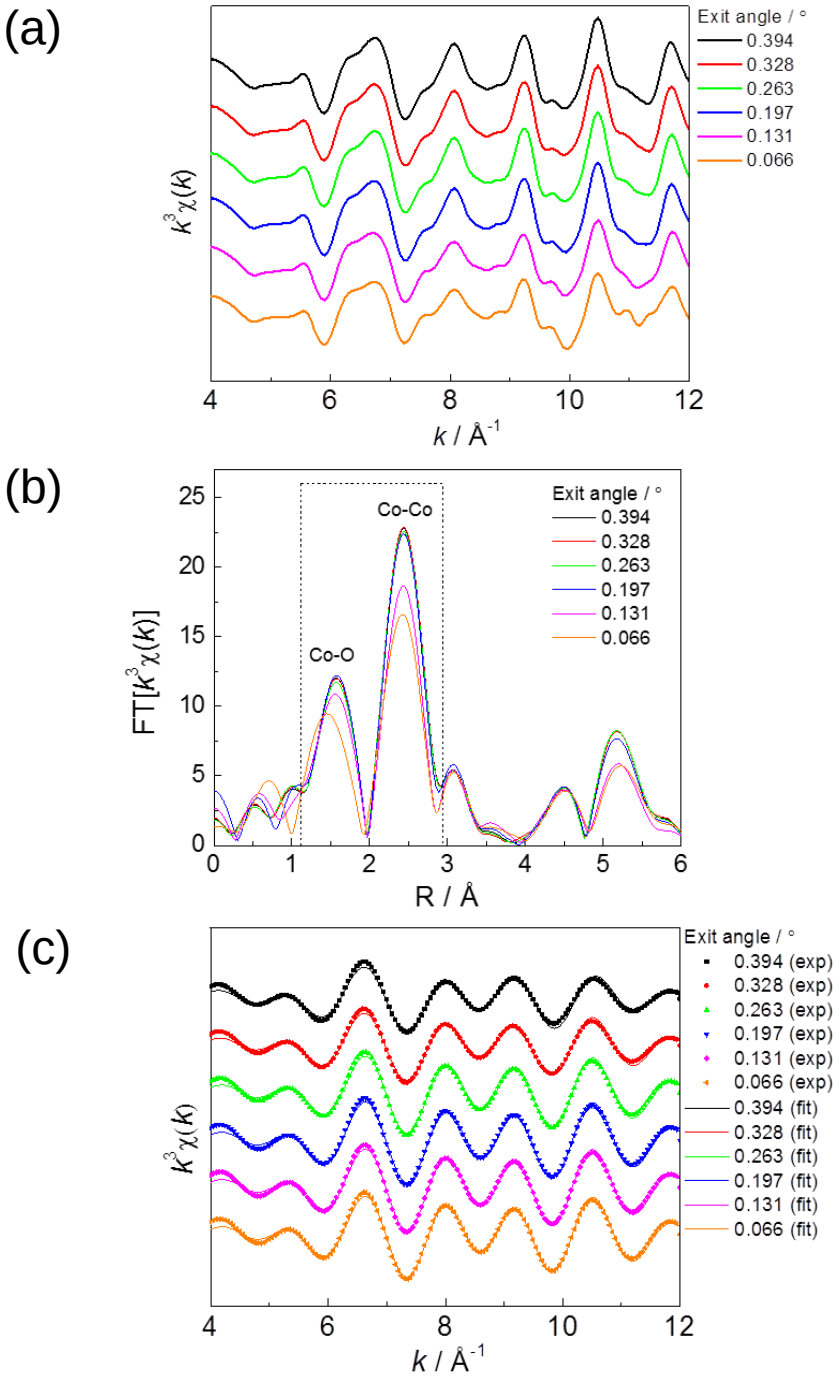

Figure 1.14 The fitting procedure of EXAFS for various exit angles of thin-film electrodes before 1st cycle of CV measurement without interlayer. (a) The k^3-weighted EXAFS raw spectra. (b) Fourier transform of the k^3-weighted EXAFS. The dot line represents the fitting range. (c) The curve fitting of the EXAFS oscillations.

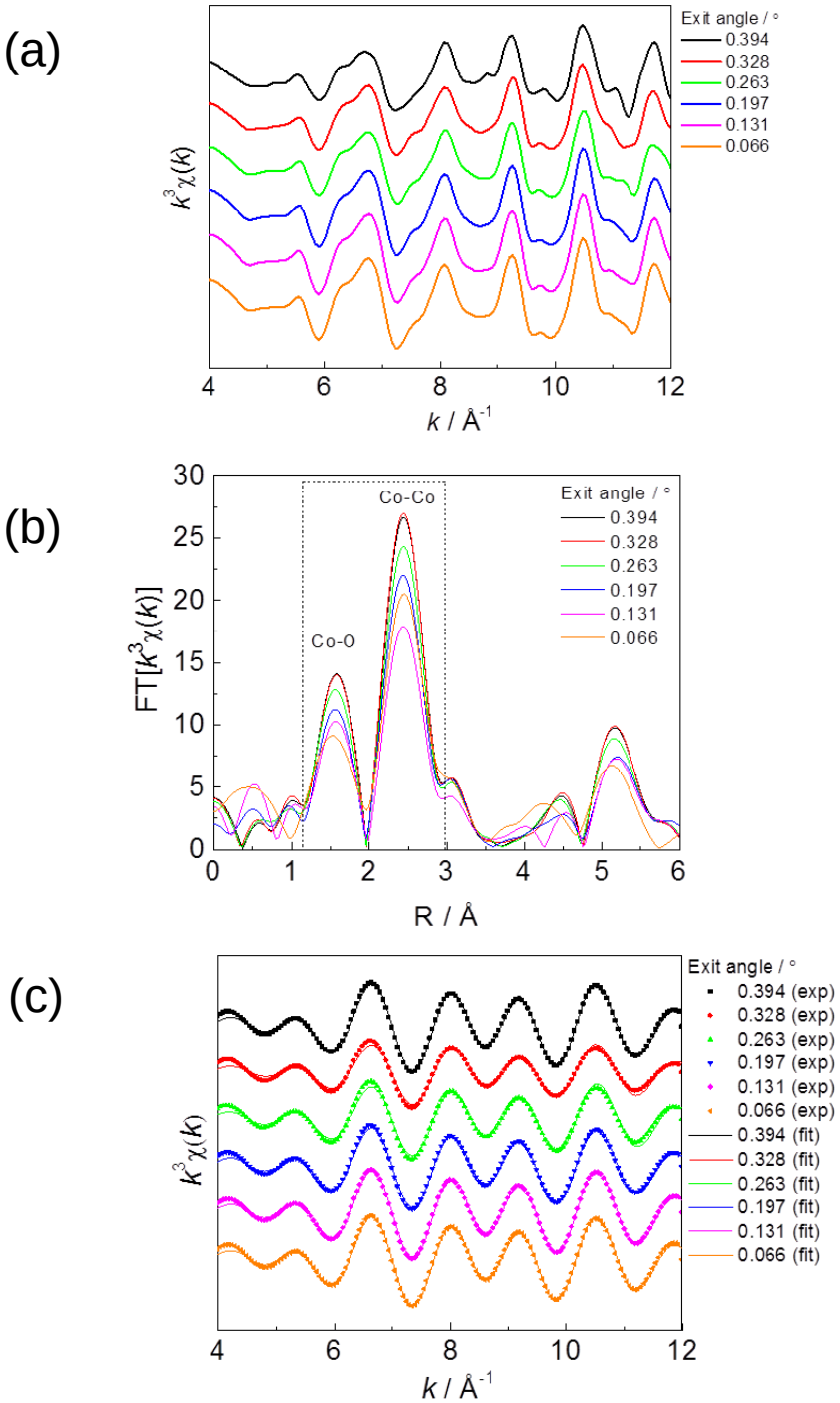

Figure 1.15 The fitting procedure of EXAFS for various exit angles of thin-film electrodes after 1st cycle of CV measurement without interlayer. (a) The k^3-weighted EXAFS raw spectra. (b) Fourier transform of the k^3-weighted EXAFS. The dot line represents the fitting range. (c) The curve fitting of the EXAFS oscillations.

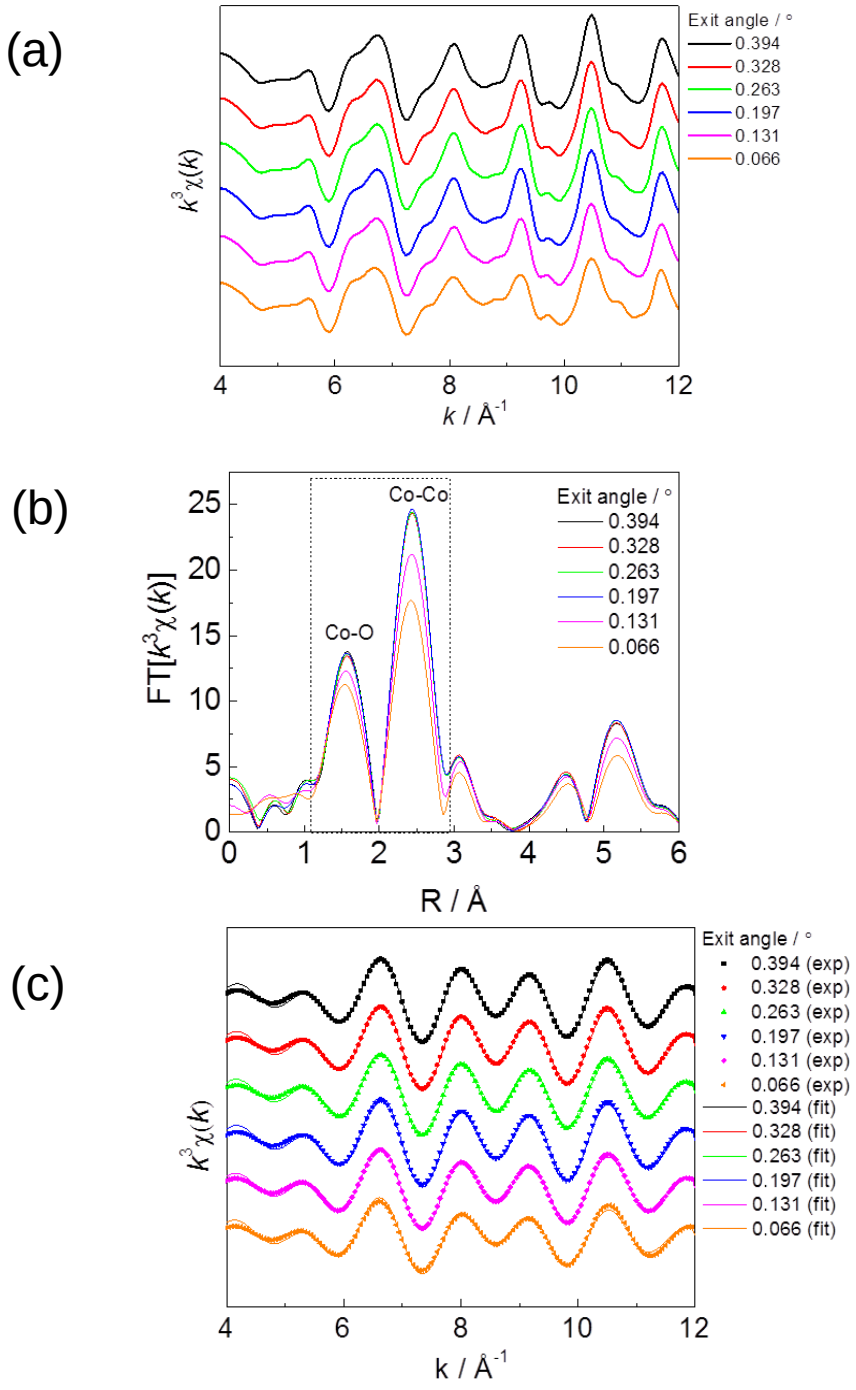

Figure 1.16 The fitting procedure of EXAFS for various exit angles of thin-film electrodes before 1st cycle of CV measurement with interlayer. (a) The k^3-weighted EXAFS raw spectra. (b) Fourier transform of the k^3-weighted EXAFS. The dot line represents the fitting range. (c) The curve fitting of the EXAFS oscillations.

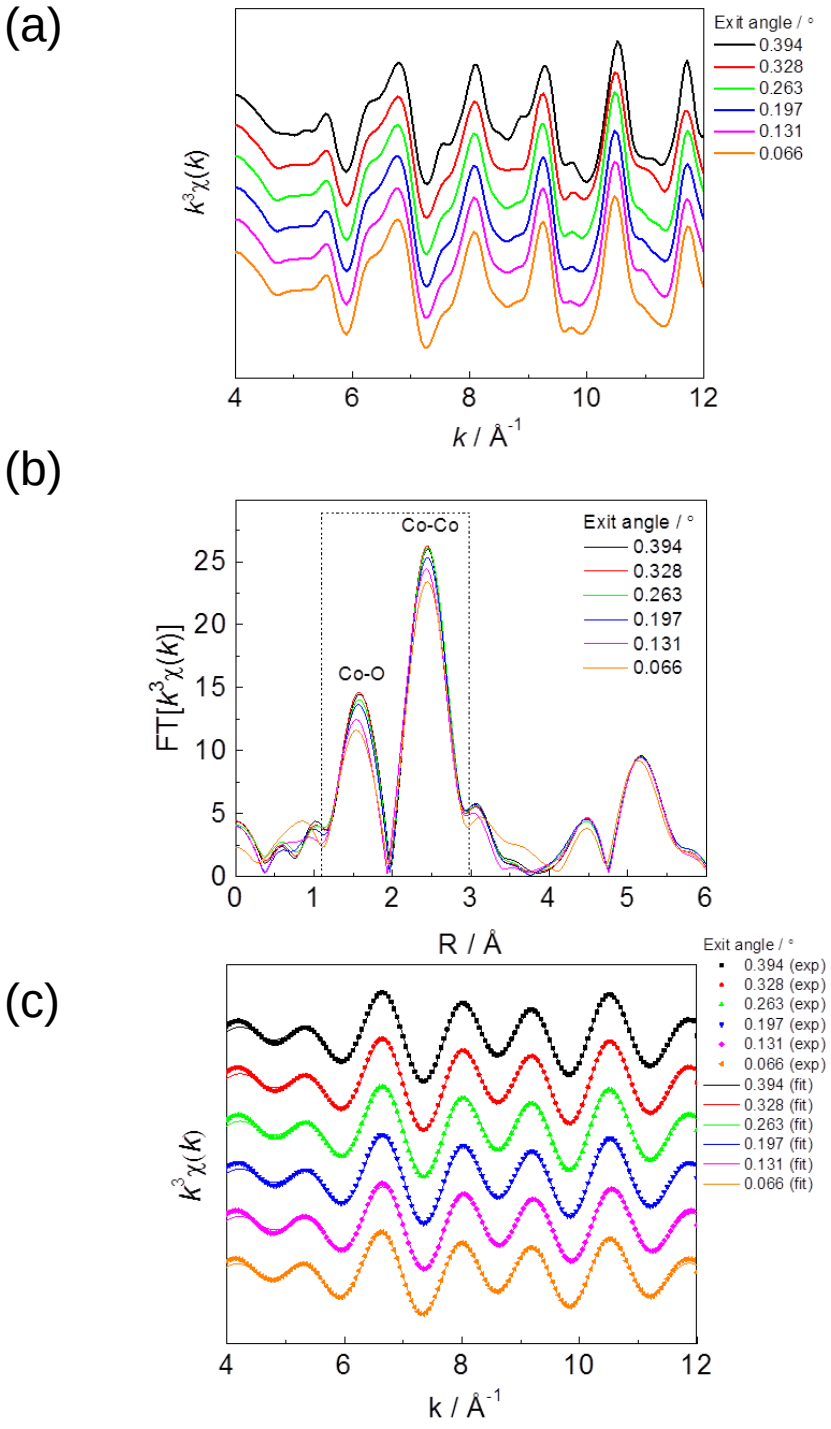

Figure 1.17 The fitting procedure of EXAFS for various exit angles of thin-film electrodes after 1st cycle of CV measurement with interlayer. (a) The k^3-weighted EXAFS raw spectra. (b) Fourier transform of the k^3-weighted EXAFS. The dot line represents the fitting range. (c) The curve fitting of the EXAFS oscillations.

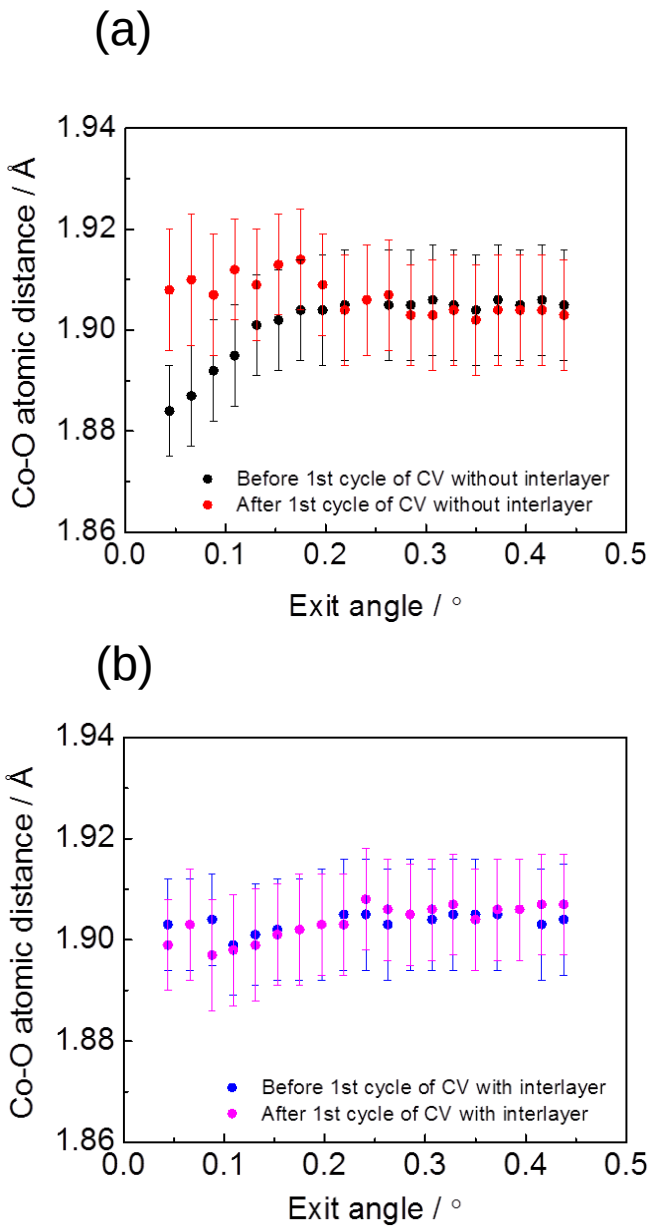

Figure 1.18 Co-O bond distance for the thin-film electrodes (a) without and (b) with the interlayer from different exit angle before and after 1st cycle of CV measurement.

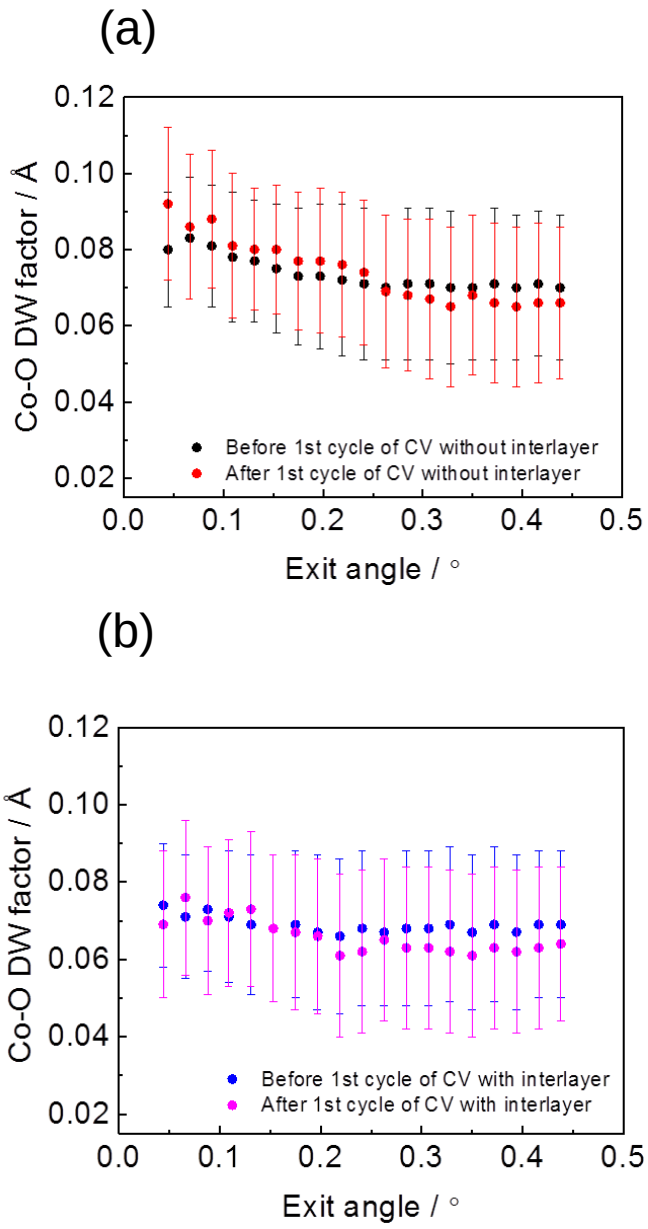

Figure 1.19 DW factor of Co-O bond for the thin-film electrodes (a) without and (b) with the interlayer from different exit angle before and after 1st cycle of CV measurement.

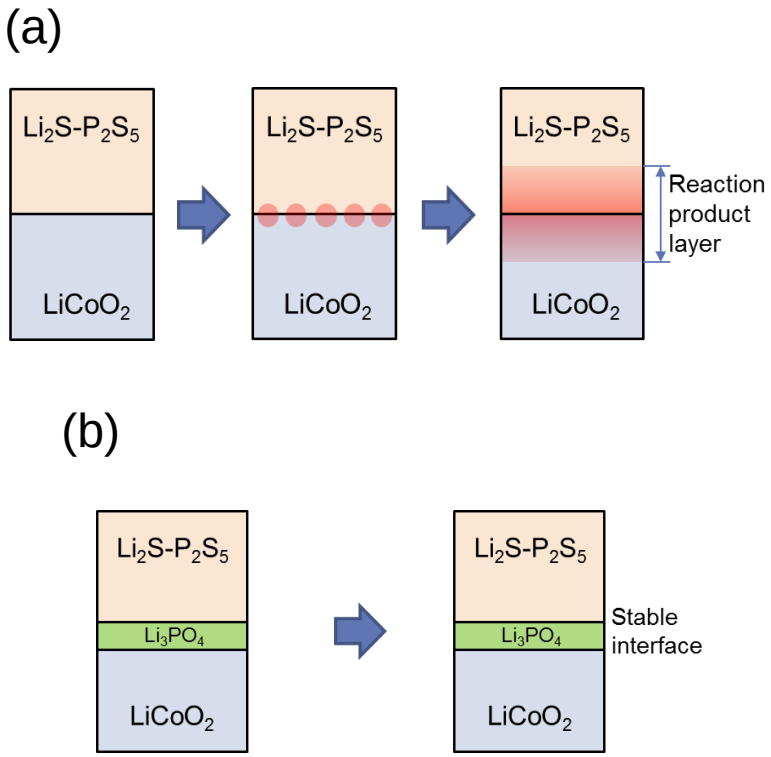

Figure 1.20 Reaction mechanism of the thin-film electrodes (a) without and (b) with the interfacial modification during charge and discharge processes.

Reference

(1) J. B. Goodenough, K. S. Park, *J. Am. Chem. Soc.* 2013, **135**, 1167–1176.

(2) B. Scrosati, J. Hassoun, Y. K. Sun, *Energy Environ. Sci.* 2011, **4**, 3287–3295.

(3) D. A. Notter, M. Gauch, R. Windmer, P. Wager, A. Stamp, R. Zah, H. J. Althaus, *Environ. Sci. Technol. Lett.* 2010, **44**, 6550–-6556.

(4) A. M. Haregewoin, A. S. Wotango, B. J. Hwang, *Energy Environ. Sci.* 2016, **9**, 1955–1988.

(5) S. F. Wang, X. W. Yu, A. Manthiram, *Nat. Rev. Mater.* 2017, **2**, 16103.

(6) Y. Kato, S. Hori, K. Sukuzi, M. Hirayama, A. Mitsui, M. Yonemura, H. Iba, R. Kanno, *Nat. Energy* 2016, **1**, 16030.

(7) M. Tatsumisago, M. Nagao, A. Hayashi, *J. Asian Ceramic Societies* 2013, **1**, 17–25.

(8) N. Ohta, K. Takada, I. Sakaguchi, L. Zhang, R. Ma, K. Fukuda, M. Osada, T. Sasaki, *Electrochem. Commun.* 2007, **9**, 1486−1490.

(9) Y. Ito, Y. Sakurai, S. Yubuchi, A. Sakuda, A. Hayashi, M. Tatsumisago, *J. Electrochem. Soc.* 2015, **162**, A1610–A1616.

(10) A. Sakuda, A. Hayashi, M. Tatsumisago, *Chem. Mater.* 2010, **22**, 949−956.

(11) K. Takada, N. Ohta, L. Zhang, K. Fukuda, I. Sakaguchi, R. Ma, M. Osada, T. Sasaki, *Solid State Ionics* 2008, **179**, 1333−1337.

(12) N. Machida, J. Kashiwagi, M. Naito, T. Shigematsu, *Solid State Ionics* 2012, **225**, 354−358.

(13) S. T. Myung, K. Izumi, S. Komaba, Y. K. Sun, H. Yashiro, N. Kumagai, *Chem. Mater.* 2005, **17**, 3695–3704.

(14) J. Haruyama, K. Sodeyama, L. Han, K. Takada, Y. Tateyama, *Chem. Mater.* 2014, **26**, 4248–4255.

(15) M. Haruta, S. Shiraki, T. Suzuki, A. Kumatani, T. Ohsawa, Y. Takagi, R. Shimizu, T. Hitosugi, *Nano Lett.* 2015, **15**, 1498−1502.

(16) M. Zarabian, M. Bartolini, P. Pereira-Almao, V. Thangadurai, *J. Electrochem. Soc.* 2017, **164**, A1133–A1139.

(17) Z, Y. Wang, D. Santhanagopalan, W. Zhang, F. Wang, H. L. Xin, K. He, J. C. Li, N. Dudney, Y. S. Meng, *Nano Lett.* 2016, **16**, 3760–3767.

(18) D. Santhanagopalan, D. Qian, T. McGilvray, Z. Y. Wang, F. Wang, F. Camino, J. Graetz, N. Dudney, Y. S. Meng, *J. Phys. Chem. Lett.* 2014, **5**, 298–303.

(19) T. Okumura, T. Nakatsutsumi, T. Ina, Y. Orikasa, H. Arai, T. Fukutsuka, Y. Iriyama, T. Uruga, H. Tanida, Y. Uchimoto, Z. Ogumi, *J. Mater. Chem.* 2011, **21**, 10051−10060.

(20) Y. Orikasa, D. Takamatsu, K. Yamamoto, Y. Koyama, S. Mori, T. Masese, T. Mori, T. Minato, H. Tanida, T. Uruga, Z. Ogumi, Y. Uchimoto, *Adv. Mater. Interfaces* 2014, **1**, 1400195.

(21) S. Yubuchi, Y. Ito, T. Matsuyama, A. Hayashi, M. Tatsumisago, *Solid State Ionics* 2016, **285**, 79–82.

(22) A. Sakuda, A. Hayashi, S. Hama, M. Tatsumisago, *J. Am. Ceram. Soc.* 2010, **93**, 765–768.

(23) J. N. Reimers, J. R. Dahn, *J. Electrochem. Soc.* 1992, **139**, 2091–2097.

(24) N. A. Abdul Aziz, M. D. Cunha, T. K. Abdullah, A. A. Moamad, *Int. J. Energy Res.* 2016, **41**, 289–296.

(25) D. Takamatsu, Y. Koyama, Y. Orikasa, S. Mori, T. Nakatsutsumi, T. Hirano, H. Tanida, H. Arai, Y. Uchimoto, Z. Ogumi, *Angew. Chem., Int. Ed.* 2012, **51**, 11597−11601.

(26) X. Y. Qiu, Q. C. Zhuang, Q. Q. Zhang, R. Cao, P. Z. Ying, Y. H. Qiang, S. G. Sun, *Phys. Chem. Chem. Phys.* 2012, **14**, 2617–2630.

(27) I. Nakai,; K. Takahashi, Y. Shiraishi, T. Nakagome, F. Nishikawa, *J. Solid State Chem.* 1998, **140**, 145–148.

(28) Y. Koyama, H. Arai, Z. Ogumi, I. Tanaka, Y. Uchimoto, *Phys. Rev. B* 2012, **85**, 075129.

(29) D. Takamatsu, T. Nakatsutsumi, S. Mori, Y. Orikasa, M. Mogi, H. Yamashige, K. Sato, T. Fujimoto, Y. Takamashi, H. Murayama, M. Oishi, H. Tanida, T. Uruga, H. Arai, Y. Uchimoto, Z. Ogumi, *J. Phys. Chem. Lett.* 2011, **2**, 2511–2514.

(30) W. D. Richards, L. J. Miara, Y. Wang, J. C. Kim, G. Ceder, *Chem. Mater.* 2016, **28**, 266–273.

(31) W. Liu, E. Hu, H. Jiang, Y. Xiang, Z. Weng, M. Li, Q. Fan, X. Yu, E. I. Altman, H. Wang, *Nat. Commun.* 2016, **7**, 10771.

(32) Y. Z. Zhu, X. F. H, Y. F. Mo, *ACS Appl. Mater. Interfaces* 2015, **7**, 23685–23693.

Chapter 2. Elucidation of the Effect of Introducing Li_3PO_4 Interlayer into $LiNi_{0.5}Mn_{1.5}O_4$/Li_2S-P_2S_5 Interface in All-Solid-State Battery

2.1. Introduction

All-solid-state lithium-ion batteries using sulfide solid electrolytes are considered as one of the promising alternative batteries due to their outstanding safety, high gravimetric and volumetric energy density comparison to traditional liquid electrolyte based systems. In order to vaimprove the energy density, application of high-voltage cathode materials to all-solid-state lithium-ion batteries has been investigated.[1,2]

The $LiNi_{0.5}Mn_{1.5}O_4$ with spinel structure is one of the most promising candidates for high voltage cathode used in all-solid-state batteries[3-5] because of high operating voltage of 4.7 V (vs Li/Li^+) and free of toxic metal. However, the high interfacial resistance between cathode and solid electrolyte occurs during charging process in all-solid-state batteries, impeding the battery performance.[6] In order to achieve the attractive battery performance, it is important to design the interface between cathode and solid electrolyte with the low interfacial resistance.

Interfacial modification has been used as an effective method to minimize the interfacial resistance.[7] Ohta *et al.* first reported that $LiNbO_3$ and $Li_4Ti_5O_{12}$ coatings

could improve the rate performance of $LiCoO_2$ in all-solid-state batteries.[8,9] Sakurai *et al.*[10] and Ito *et al.*[11] demonstrated that Li_3PO_4 and Li_4SiO_4 coatings could improve the rate performance of $LiCoO_2$ in all-solid-state batteries. For $LiCoO_2$, many other materials such as ZrO_2,[12] Al_2O_3[13] and MgO[14] were also used as interlayers between cathode and solid electrolyte, which were proved effective for reducing interfacial resistance cathode/solid electrolyte interface. For $LiNi_{0.5}Mn_{1.5}O_4$, the interlayer materials may need higher electrochemical stability because of the high potential gap between cathode and interlayer. Yubuchi *et al.*[15] reported that Li_3PO_4-coated $LiNi_{0.5}Mn_{1.5}O_4$ exhibited improve interfacial resistance and rate performance in all-solid-state battery using $80Li_2S{\cdot}20P_2S_5$ sulfide solid electrolyte. Oh *et al.*[16] demonstrated that $LiNbO_3$ was also effective for suppressing the interfacial resistance of the interface between $LiNi_{0.5}Mn_{1.5}O_4$ and $Li_{10}GeP_2S_{12}$. Although the interfacial modification has been proved to be effective for reducing interfacial resistance, the battery performance such as capacity and/or cycle ability is still low.[15,16] The reason for the low battery performance has still remained unclear.

As the origin of the interfacial resistance, two main hypotheses have been proposed previously: (1) space-charge layer theory and (2) reaction product layer theory. For space-charge layer theory, based on electrochemical analysis[17] and theoretical calculation,[18] a space-charge layer was considered to form at the interface due to the gap of lithium electrochemical potential between oxide cathode and sulfide electrolyte. For product layer theory, based on transmission electron microscopy (TEM) observation and energy dispersive X-ray spectrometry (EDX) analysis of the

interface,[19] a reaction product layer was considered to form at interface due to the mutual diffusion of elements between cathode and electrolyte during charge/discharge process.

Although electrochemical analysis and TEM observation are powerful techniques for understanding the interfacial phenomenon, they do not obtain the information of interfacial electronic and local structures that are important information for a further discussion of interfacial reaction mechanism. X-ray absorption spectroscopy (XAS) is an useful method to analyze electronic and local structures of a certain atom, and especially depth-resolved XAS (DR-XAS) technique has been proved to be an effective method to examine those structures at the interface.[26]

In this work, we prepared model thin-film electrodes to analyze the effect of introducing interlayer into cathode/electrolyte interface in the respect of electronic and local structures at high voltage using DR-XAS technique. We chose $LiNi_{0.5}Mn_{1.5}O_4$ and $80Li_2S{\cdot}20P_2S_5$ as cathode and solid electrolyte, and Li_3PO_4 as the interlayer material, which is effective for reducing the interfacial resistance between $LiNi_{0.5}Mn_{1.5}O_4$ and $80Li_2S{\cdot}20P_2S_5$.[15] First, two types of thin-film electrodes of $LiNi_{0.5}Mn_{1.5}O_4/80Li_2S{\cdot}20P_2S_5$ and $LiNi_{0.5}Mn_{1.5}O_4/Li_3PO_4/80Li_2S{\cdot}20P_2S_5$ were prepared by pulsed laser deposition. Then, their electrochemical performances were studied by using cyclic voltammetry (CV) and electrochemical impedance spectroscopy (EIS). Finally, the interface status of both thin-film electrodes was compared before and after charge/discharge cycle using DR-XAS technique. Our study

revealed that Li_3PO_4 interlayer stabilizes the interfacial structure between $LiNi_{0.5}Mn_{1.5}O_4$/$80Li_2S{\cdot}20P_2S_5$, which leads to lower interfacial resistance and higher durability during charge/discharge processes.

2.2. Experimental Section

2.2.1. Sample Preparation

Both thin-film electrodes (with and without Li_3PO_4 interlayer) were prepared by pulsed laser deposition (PLD) method. The diagrammatic sketch of the thin-film model electrodes is shown in Figure 2.1. To supply the sufficient Li amount during PLD deposition, the PLD targets for $LiNi_{0.5}Mn_{1.5}O_4$ thin films consisted of $LiNi_{0.5}Mn_{1.5}O_4$ (Sigma-Aldrich Co., LLC) with 5 w% Li_2O (Sigma-Aldrich Co., LLC.). The targets were sintered at 773 K for 6 h. The $LiNi_{0.5}Mn_{1.5}O_4$ thin films were deposited on mirror-polished polycrystalline platinum substrates (15 mm × 15 mm × 2 mm) under an oxygen pressure of 26 Pa for 30 min. The substrates were heated at a temperature of 873 K. A Nd:YAG laser (λ = 266 nm) with a repeating frequency of 10 Hz were used for the laser ablation. The laser energy density was set to 3.5 J cm^{-2} at the target. The PLD target for Li_3PO_4 interlayers were prepared by sintering Li_3PO_4 (98%, Wako Pure Chemical Industries Ltd.) at 873 K for 6 h. The Li_3PO_4 thin films were deposited on the $LiNi_{0.5}Mn_{1.5}O_4$ films at room temperature under an argon pressure of 0.01 Pa for 120 s. A KrF excimer laser (λ = 248 nm) with a repeating frequency of 5 Hz was used for the laser ablation. The laser energy density was set to 2 J cm^{-2} at the target.[21] The PLD target for $80Li_2S{\cdot}\ 20P_2S_5$ layer consisted of Li_2S (99.9%, Idemitsu Kosan Co. Ltd.) and

P_2S_5 (99%, Aldrich Chemical Co., Inc.) with a molar ratio of 80:20. The $80Li_2S{\cdot}20P_2S_5$ thin films were deposited on $LiNi_{0.5}Mn_{1.5}O_4$ films or Li_3PO_4 interlayer at room temperature under an argon pressure of 5 Pa for 140 s. A KrF excimer laser (λ = 266 nm) with a repeating frequency of 5 Hz was used for the laser ablation. The laser energy density was set to 2 J cm^{-2} at the target.[22]

2.2.2. Characterization of LiNi0.5Mn1.5O4 Thin Film

After deposition of $LiNi_{0.5}Mn_{1.5}O_4$ thin-film electrode on mirror-polished Pt substrate, the $LiNi_{0.5}Mn_{1.5}O_4$ thin film was characterized by X-ray diffraction (XRD) and atomic force microscope (AFM). The XRD measurement was carried out by Ultima IV (Rigaku Co., LLC.). The AFM measurement was carried by AFM5200S (HITACHI Co., LLC.). The scan area was 1000 nm ×1000 nm.

2.2.3. Electrochemical Measurement

Cyclic voltammetry (CV) were carried out for the thin-film electrodes with and without Li_3PO_4 interlayer by using a three-electrode cell as shown in Figure 1.2. To minimize the influence of interface between anode and solid electrolyte, the cell were simplified by using liquid electrolyte. The thin-film electrode was used as working electrode. The Li_3PO_4 protective layers were deposited on the top to restrain the dissolving of $80Li_2S{\cdot}20P_2S_5$ into the liquid electrolyte. Lithium metals were used as both counter electrode and reference electrode. A 1 M $LiPF_6$ in ethylene carbonate and ethyl methyl carbonate (EC : EMC = 3:7 v/v %) was used as the liquid electrolyte.

The CV measurement was carried out for 10 cycles from 3.5 V to 5.0 V with a sweep speed of 0.1 mV s^{-1}. Electrochemical impedance spectroscopy (EIS) was carried out for analyzing the change of interfacial resistance during charge/discharge process by using the same cell configuration as CV measurement during four charge/discharge cycles. The amplitude was 30 mV and the scan range was from 10^{-2} Hz to 10^{6} Hz. The potential of EIS measurement points were 4.4 V-5.0 V versus Li/Li^{+} during both charge/discharge, respectively. Before each EIS measurement point, the cathode was set at the target potential by linear sweep voltammetry and kept at that potential for 30 min by the charge or discharge current change becomes sufficient small.

2.2.4. Depth-Resolved X-Ray Absorption Spectroscopy Measurement

In this study, to compare the change of interface before and after charge/discharge process, the thin-film electrodes with and without interlayer were both analyzed by DR-XAS at two measurement points: (1) as-prepared and (2) after the 1st cycle of CV measurement. Thin-films after 1st cycle of CV measurement refers to thin-films that were charged from open circuit potential (OCP) to 5.0 V (vs. Li/Li^{+}) and then discharged to 3.5 V (vs. Li/Li^{+}). DR-XAS measurements of Ni *K*-edge and Mn *K*-edge in $LiNi_{0.5}Mn_{1.5}O_4$ cathode were carried out in BL37XU (SPring-8, Japan) with a two-dimensional pixel array detector, Pilatus (Dectris Ltd.) for detecting the exit X-ray fluorescence. Thin-film electrodes after charge/discharge process were taken out from the three-electrodes cells, washed by EC:EMC and dried, then set into a custom-made

cell which can be vacuumed to 10^{-3} Pa and can pass incident and exit X-ray. All of the operations mentioned above were carried out in glovebox with argon atmosphere.

2.3. Results and Discussion

2.3.1. Characterization of $LiNi_{0.5}Mn_{1.5}O_4$ Thin Film

XRD pattern of the $LiNi_{0.5}Mn_{1.5}O_4$ thin-film electrode deposited on Pt substrate by PLD was shown in Figure 2.2(a). The all peaks were indexed to the peaks attributed to $LiNi_{0.5}Mn_{1.5}O_4$ and Pt substrate without any impurity. The AFM image of the $LiNi_{0.5}Mn_{1.5}O_4$ thin-film was shown in Figure 2.2(b). The average surface roughness is 6.6 nm. Based on the XRD and AFM results, a smooth $LiNi_{0.5}Mn_{1.5}O_4$ thin-film electrode was successfully fabricated by PLD.

2.3.2. Electrochemical Measurement

Electrochemical properties of the prepared thin-film electrodes with or without Li_3PO_4 interlayer were evaluated with CV and EIS measurements. The cyclic voltammograms of both thin-film electrodes after second cycle were shown in Figure 2.3. The small anodic and cathodic peaks corresponding to a redox reaction of Mn^{3+}/Mn^{4+} were detected at 4.0 V. Another two pairs of reversible redox peaks observed at 4.7 V and 4.8 V represent the redox reactions of Ni^{2+}/Ni^{3+} and Ni^{3+}/Ni^{4+}, respectively.[23,24] Also, the anodic current was observed at high voltage range (4.8 V ~ 5.0 V).

Comparing the thin-film without Li_3PO_4 interlayer, the current attributed to the redox reactions of Ni^{2+}/Ni^{3+} and Ni^{3+}/Ni^{4+} became larger for the thin-film with Li_3PO_4 interlayer during cycling, which shows reduction of the interfacial resistance by introduction of the Li_3PO_4 interlayer. In addition, the anodic current at high voltage range (4.8 V ~ 5.0 V) was reduced for the thin-film with Li_3PO_4 interlayer, meaning that interlayer suppressed the oxidation. The discharge capacities and coulombic efficiency of both thin-film electrodes based on CV measurements were plotted against the cycle number in Figure 2.4(a) and Figure 2.4(b), respectively. The discharge capacity of thin-film electrode without Li_3PO_4 interlayer gradually decreased from 0.35 to 0.14 mC with cycling (1st cycle ~ 9th cycle). In contrast, although the discharge capacity of the thin-film electrode with Li_3PO_4 interlayer also showed a decrease from 0.51 to 0.46 mC (1st cycle ~ 9th cycle), it showed higher discharge capacity retention than thin-film electrode without Li_3PO_4 interlayer. Although the introduction of the Li_3PO_4 interlayer improves the coulombic efficiency of $LiNi_{0.5}Mn_{1.5}O_4$, the coulombic efficiency is still less than 50% from 2nd cycle to 10th cycle. These results suggest that interface modification with Li_3PO_4 interlayer can improve the cyclability of $LiNi_{0.5}Mn_{1.5}O_4$ cathode when using $80Li_2S{\cdot}20P_2S_5$ solid electrolyte. However, even at the interface modified by Li_3PO_4 interlayer, the coulombic efficiency is still low of about 40%.

The interfacial resistance between cathode and solid electrolyte during charge/discharge process was examined by EIS measurement. The Nyquist plots of charge process in the 1st potentistatic cycle was shown in Figure 2.5(a) and 2.5(b).

Equivalent circuit for EIS fitting was shown in Figure 2.5(c). The interfacial resistance obtained by the fitting at 4.4 V, 4.5 V, 4.6 V, 4.7 V and 4.8 V from 1st to 4th cycles were plotted in Figure 2.6. The curve fitting cannot be conducted at the potential range from 4.9 to 5.0 V because both thin-film behaved like blocking electrode. The interfacial resistance of the thin-film electrode without Li_3PO_4 interlayer was lower than that of thin-film electrode with Li_3PO_4 interlayer at initial state. However, it showed an increasing trend from 1st cycle to 4th cycle. Although the interfacial resistance of the thin-film with Li_3PO_4 interlayer was higher due to the existence of Li_3PO_4 interlayer at initial state, it kept decreasing during charge/discharge processes. These results indicates that introduction of Li_3PO_4 interlayer can restrain the increase of interfacial resistance during charge/discharge process. According to the results of both CV and EIS measurement, it suggests that the interfacial modification by Li_3PO_4 interlayer can reduce the reaction at the interface between $LiNi_{0.5}Mn_{1.5}O_4$ cathode and $80Li_2S{\cdot}20P_2S_5$ solid electrolyte and improve the electrochemical performance.

2.3.3. Depth-Resolved X-Ray Absorption Spectroscopy Measurements

In order to investigate the electronic and local structures of the cathode/electrolyte interface before and after charge/discharge process, DR-XAS measurements for Mn *K*-edge and Ni *K*-edge was conducted for both thin-films. In the DR-XAS measurement, which has a depth resolution of 3-4 nm, XAS spectra gained at lower exit angles provide

more information about the surface of a thin film, whereas XAS spectra gained at higher exit angles provide more information about the bulk properties.[20,26]

The X-ray near-edge fine structure (XANES) for Mn *K*-edge and Ni *K*-edge of both thin-film electrodes measured before and after charge/discharge process were shown in Figure 2.7 and Figure 2.8, respectively. The relative energy in the half of the normalized absorbance of the XANES obtained from each exit angle to the XANES obtained from the exit angle of 0.438°, from which reflected sufficiently on the bulk information, was plotted against each exit angle. The relative energy of the Mn *K*-edge XANES of both thin-film electrodes before and after 1st cycle of CV measurement was shown in Figure 2.9(a) and 2.9(b), respectively. The relative energy of the Ni *K*-edge XANES of both thin-film electrodes before and after 1st cycle of CV measurement was shown in Figure 2.10(a) and 2.10(b), respectively. For both Mn *K*-edge and Ni *K*-edge, there was no obvious change of the relative energy before and after 1st cycle of CV measurement between cathode bulk and interface in both thin-films. These results mean that the oxidation state of Mn ions and Ni ions almost kept steady from the interface to the bulk before and after 1st cycle of CV measurement neither with or without Li_3PO_4 interlayer.

The Fourier-transform of extended X-ray absorption fine structure (EXAFS) oscillation for Mn *K*-edge and Ni *K*-edge in both thin-films electrodes before and after one potentiostatic cycle was shown in Figure 2.11 and Figure 2.12, respectively. In Figure 2.11, the radial structure functions of the local atomic environments around Mn

atoms show two peaks at 1.6 Å and 2.5 Å which are corresponding to the six-coordinated Mn-O bonds in MnO_6 octahedra and three-coordinated Mn-Mn bonds, respectively. In Figure 2.12, the radial structure functions of the local atomic environments around Ni atoms show two peaks at 1.6 Å and 2.5 Å which are corresponding to the six-coordinated Ni-O bonds in NiO_6 octahedra and three-coordinated Ni-Mn bonds, respectively. [25]

The refined interatomic distance and Debye-Waller (DW) factor for the Mn-O and Ni-O bands derived from the obtained EXAFS oscillation were calculated from k = 4 to 12 $Å^{-1}$ range. The DW factor corresponds to static local distortion. The distance and DW factor of Mn-O bonds in both thin-film electrode before and after one potentiostatic cycle are plotted against each exit angle in Figure 2.13 and Figure 2.14, respectively. The distance and DW factor of Ni-O bonds in both thin-film electrodes before and after one potentiostatic cycle are plotted against each exit angle in Figure 2.15 and Figure 2.16, respectively. In the EXAFS analysis, the standard error of the Mn-O and Ni-O distance is less than 0.003 nm, and that of the Mn-O and Ni-O DW factor is less than 0.002 nm. There was no obvious change of the interatomic distance and DW factor before and after one potentiostatic cycle difference between cathode bulk and interface in both thin-films. no matter with nor without Li_3PO_4 interlayer. These results indicate that the local structure around Mn ions and Ni ions almost kept steady from the interface to the bulk before and after 1st cycle of CV measurement neither with or without Li_3PO_4 interlayer.

2.3.4. Effect of Li_3PO_4 Interlayer

Here, we discuss the interfacial phenomenon between $LiNi_{0.5}Mn_{1.5}O_4$/Li_2S-P_2S_5, and the effect of the introducing Li_3PO_4 interlayer into the interface. Summary of the interfacial phenomenon mechanism that we propose is diagrammatically shown in Figure 2.17.

For the thin-film without Li_3PO_4 interlayer, the electrochemical measurements showed that the interfacial resistance increased and the discharge capacity decreased with cycling number. The DR-XAS measurement showed that the electronic and local structures at the interface did not change after cycling. These results indicate that the cathode material did not change during the cycling even at interface. Therefore the degradation of the electrochemical performance is caused by change of the solid electrolyte, namely, oxidation of the electrolyte (Figure 2.17(a)). First principle calculation results shows that Li_2S-P_2S_5 is thermodynamically unstable at the redox potential of $LiNi_{0.5}Mn_{1.5}O_4$ (4.7 V vs. Li/Li^+) because the potential window of Li_2S-P_2S_5 is 2.1 V ~ 2.6 V.[25] Figure 2.6 indicates the interfacial resistance increase in the period of charge.

For the thin-film with Li_3PO_4 interlayer, although the electronic and local structures at the interface also did not change after cycling, the increase of the interfacial resistance and the degradation with cycle number were suppressed. These results indicate that the Li_3PO_4 interlayer suppresses the oxidation of Li_2S-P_2S_5, leading to better electrochemical performance. Although Li_3PO_4 has a wider potential window

(0.69 ~ 4.2 V vs. Li/Li^+) than the sulfide solid electrolyte,[25] the Li_3PO_4 interlayer become thermodynamically unstable in the redox potential of $LiNi_{0.5}Mn_{1.5}O_4$.[26] Thus, we suggest that the Li_3PO_4 interlayer also oxidize at the high redox potential of $LiNi_{0.5}Mn_{1.5}O_4$ to form the productive layer, which stabilizes the interfacial structure kinetically to suppress the increase of the interfacial resistance (Figure 2.17(b)). However because the productive layer is thermodynamically unstable at the high potential, the decomposition reaction of the Li_3PO_4 interlayer proceeds during charge/discharge process, resulting in insufficient coulombic efficiency. Therefore it is necessary to find new interlayer materials with higher stability for high voltage cathode materials.

2.4. Conclusion

We examined the interfacial reaction between $LiNi_{0.5}Mn_{1.5}O_4$ cathode and $80Li_2S{\cdot}20P_2S_5$ electrolyte, and also effect of introducing Li_3PO_4 interlayer into the interface using electrochemical and DR-XAS measurements. The introduction of Li_3PO_4 interlayer improved the cyclability and decreased the interfacial resistance. Although the Li_3PO_4 interlayer decomposes under operating potential of $LiNi_{0.5}Mn_{1.5}O_4$, the productive layer derived from the Li_3PO_4 can restrain kinetically the decomposition of sulfide electrolyte, resulting in improvement of the electrochemical performance. However the Li_3PO_4 interlayer is thermodynamically unstable, and the irreversible decomposition reaction restrain its further application as interlayer in all-solid-state battery using high voltage cathode materials. Therefore, new

interlayer materials with wider electrochemical window need to construct more stable interface in all-solid-state battery.

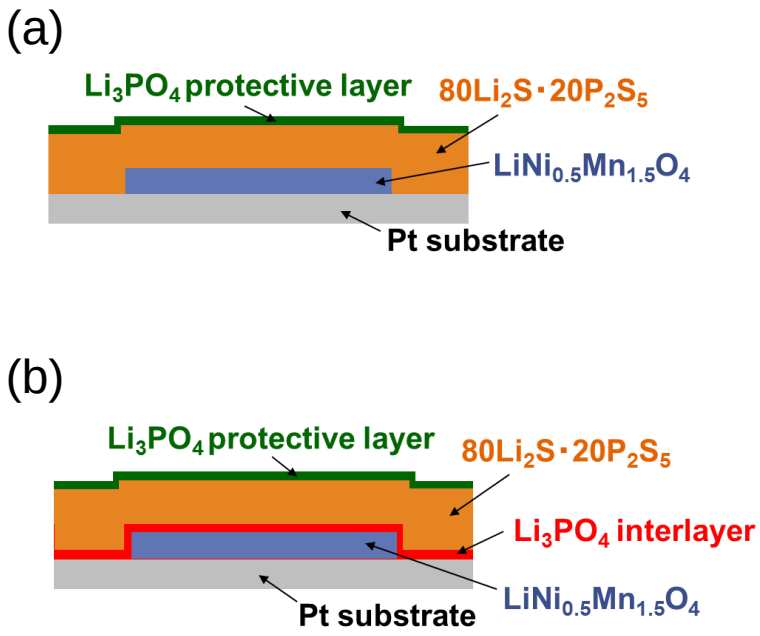

Figure 2.1 Diagrammatic sketch of the thin-film model electrodes (a) without and (b) with Li_3PO_4 interlayer.

(a)

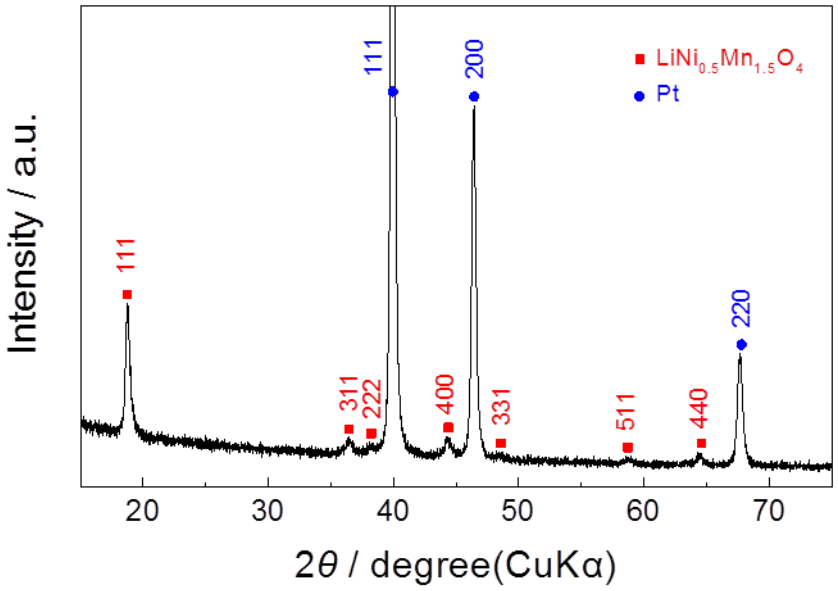

(b)

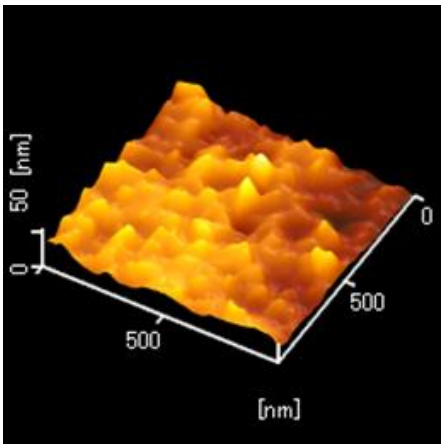

Figure 2.2 (a) XRD pattern of the $LiNi_{0.5}Mn_{1.5}O_4$ thin-film electrode deposited on Pt substrate. (b) AFM images of the $LiNi_{0.5}Mn_{1.5}O_4$ thin-film electrode.

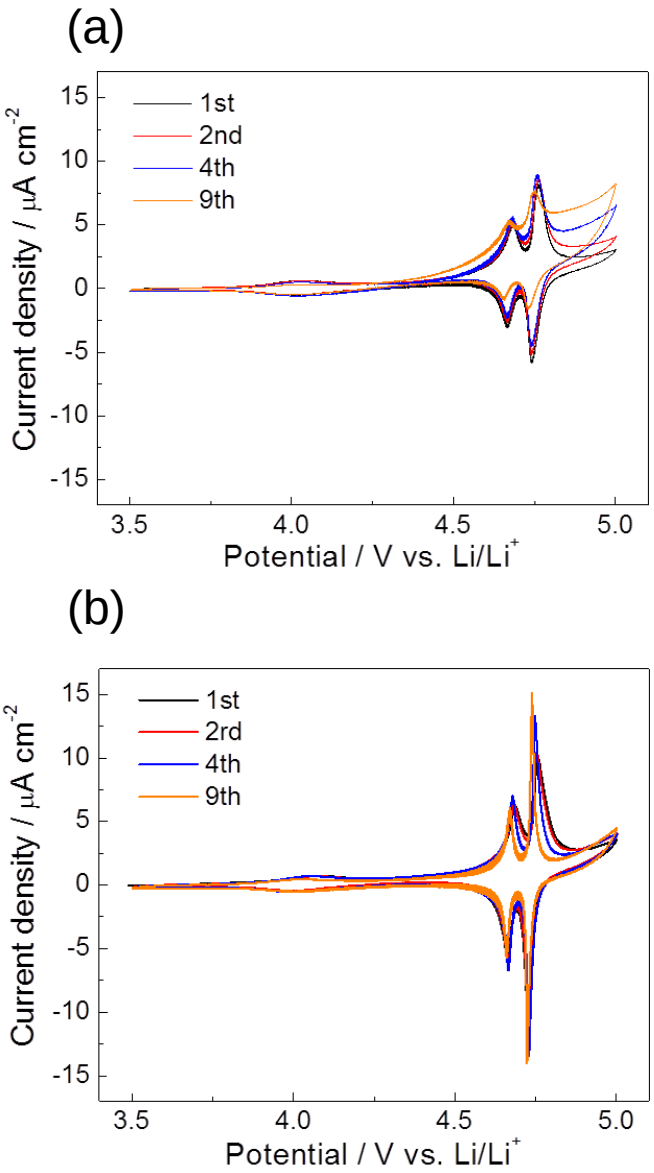

Figure 2.3 CV curves of thin-film electrodes (a) without and (b) with interlayer.

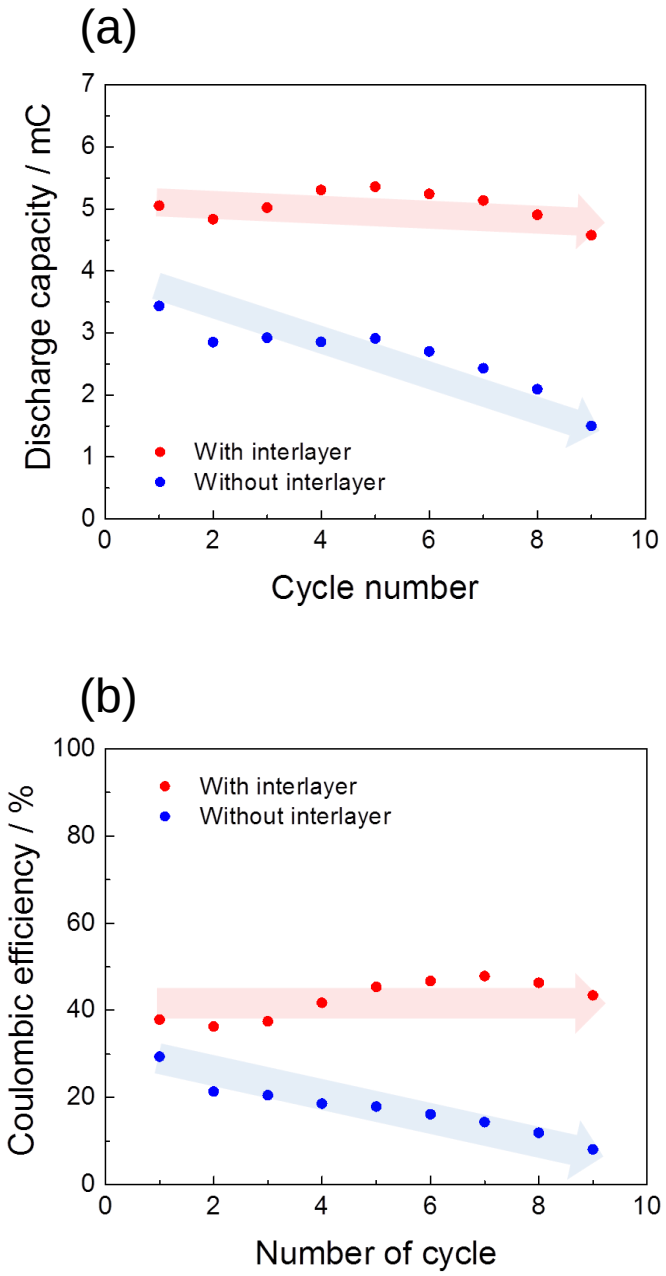

Figure 2.4 (a) Discharging capacity and (b) coulombic efficiency of electrodes with and without interlayer.

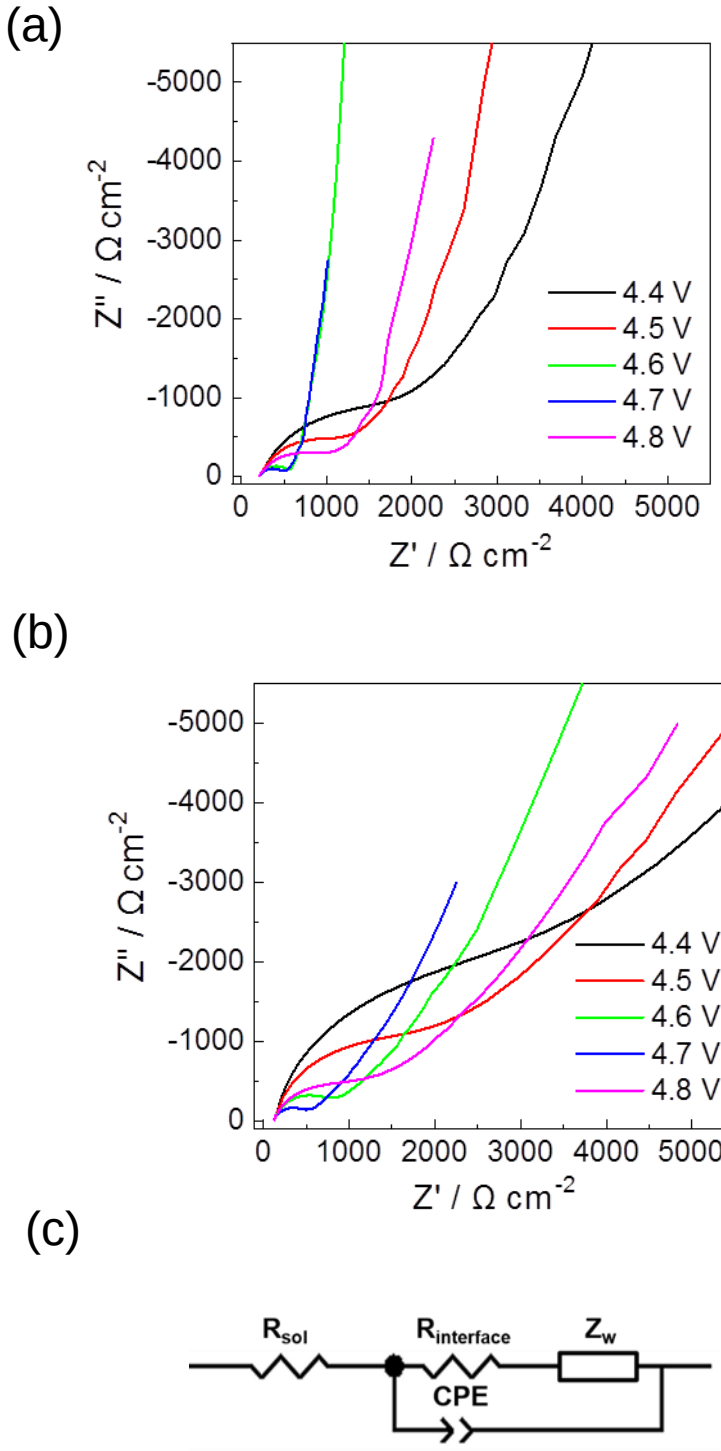

Figure 2.5 Nyquist plots of thin-film electrode (a) without and (b) with interlayer at different potential in charge process of first cycle of CV measurement. (c) Equivalent circuit for EIS fitting.

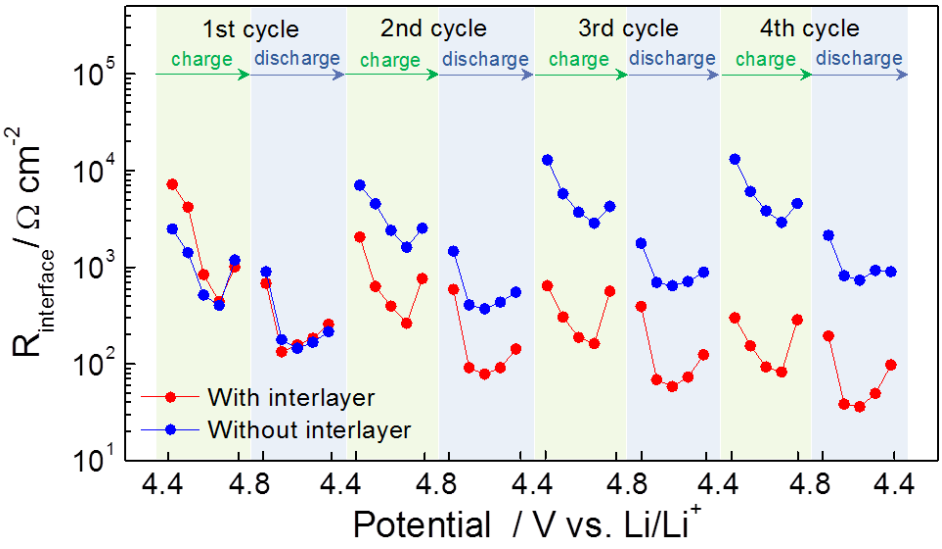

Figure 2.6 Potential-dependent interfacial resistance of thin-film electrodes without and with interlayer from 1st cycle to 4th cycle.

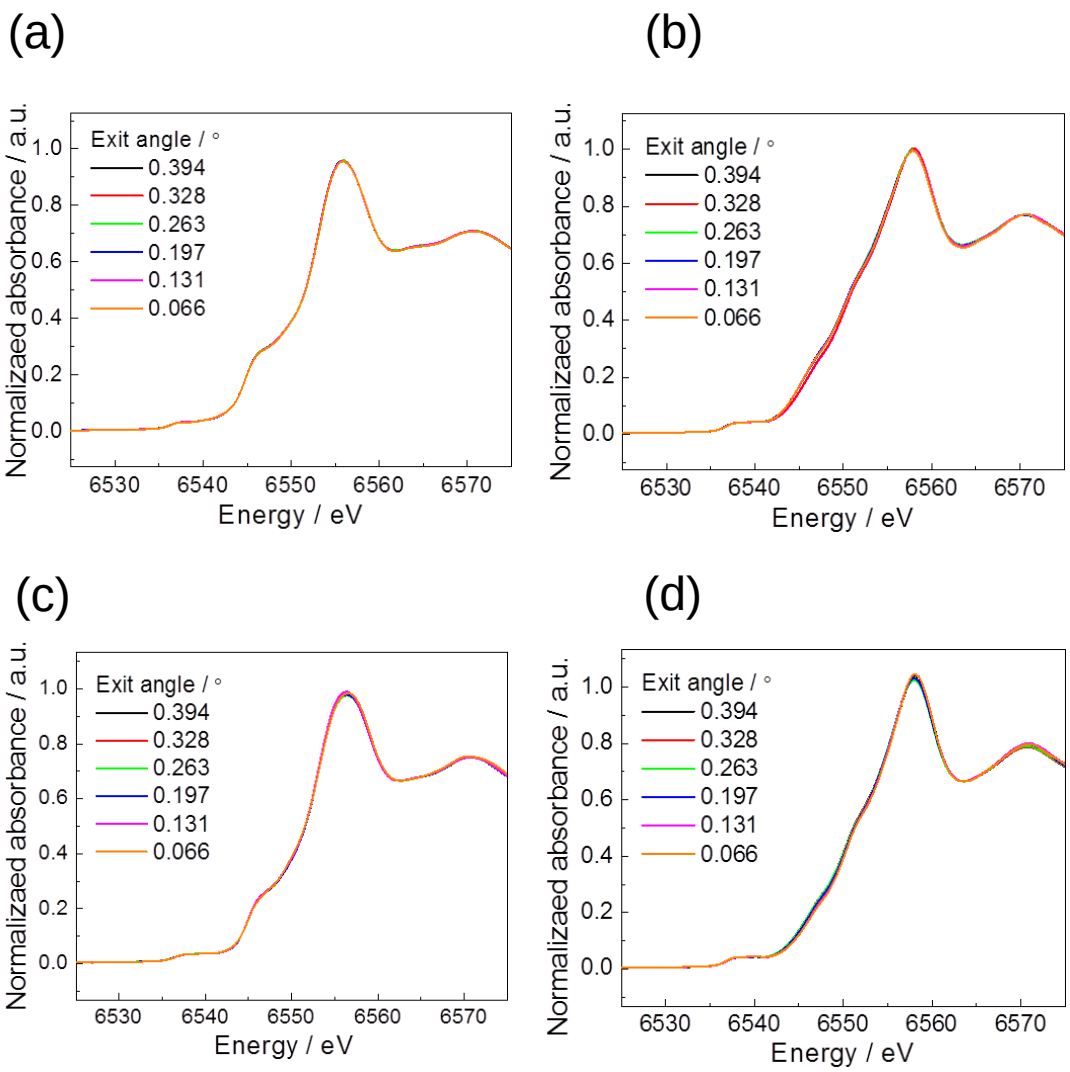

Figure 2.7 Mn *K*-edge XANES spectra of two types of thin-film electrodes measured before and after charging/discharging processes: (a) before 1st cycle of CV measurement with interlayer, (b) after 1st cycle of CV measurement with interlayer, (c) before 1st cycle of CV measurement without interlayer, (d) after 1st cycle of CV measurement without interlayer.

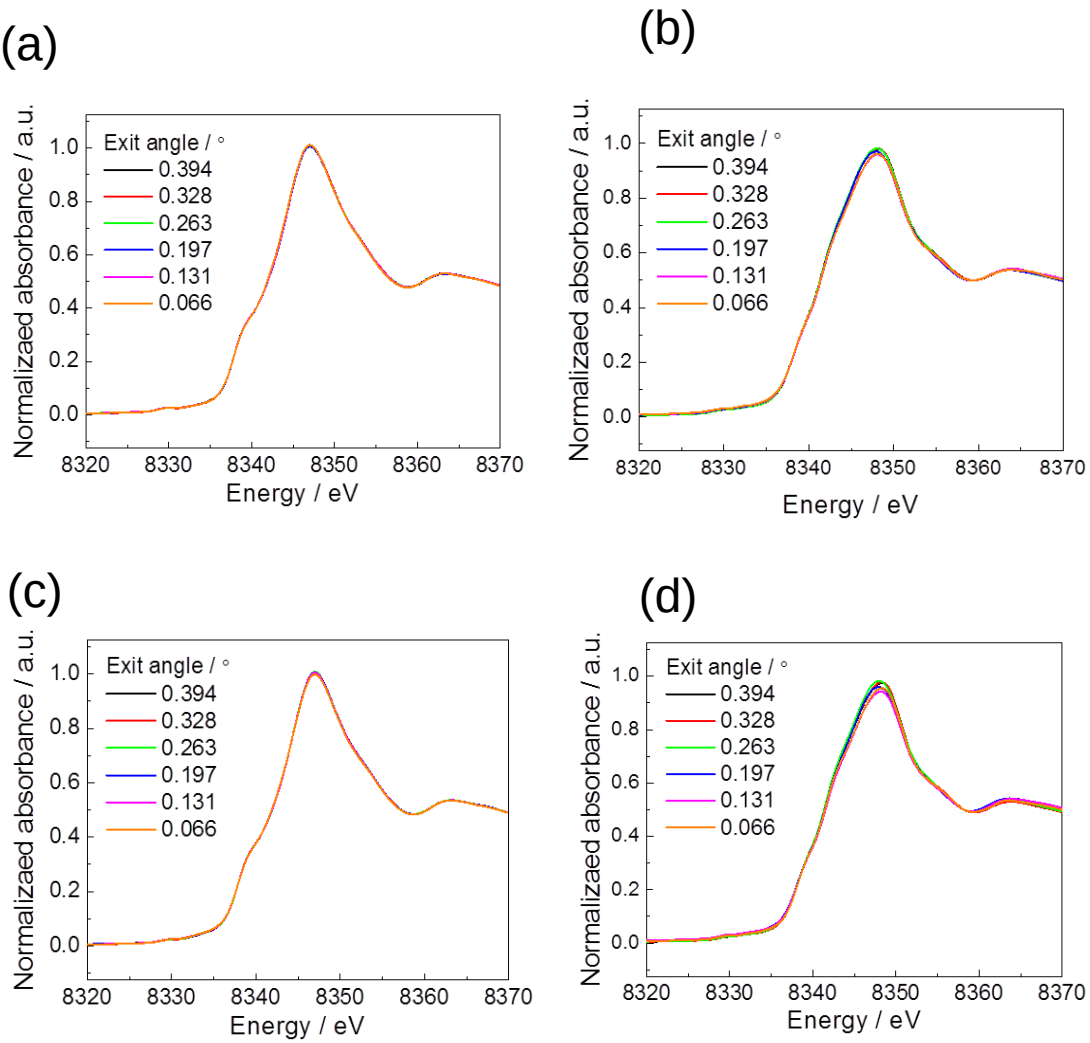

Figure 2.8 Ni *K*-edge XANES spectra of two types of thin-film electrodes measured before and after charging/discharging processes: (a) before 1st cycle of CV measurement with interlayer, (b) after 1st cycle of CV measurement with interlayer, (c) before 1st cycle of CV measurement without interlayer, (d) after 1st cycle of CV measurement without interlayer.

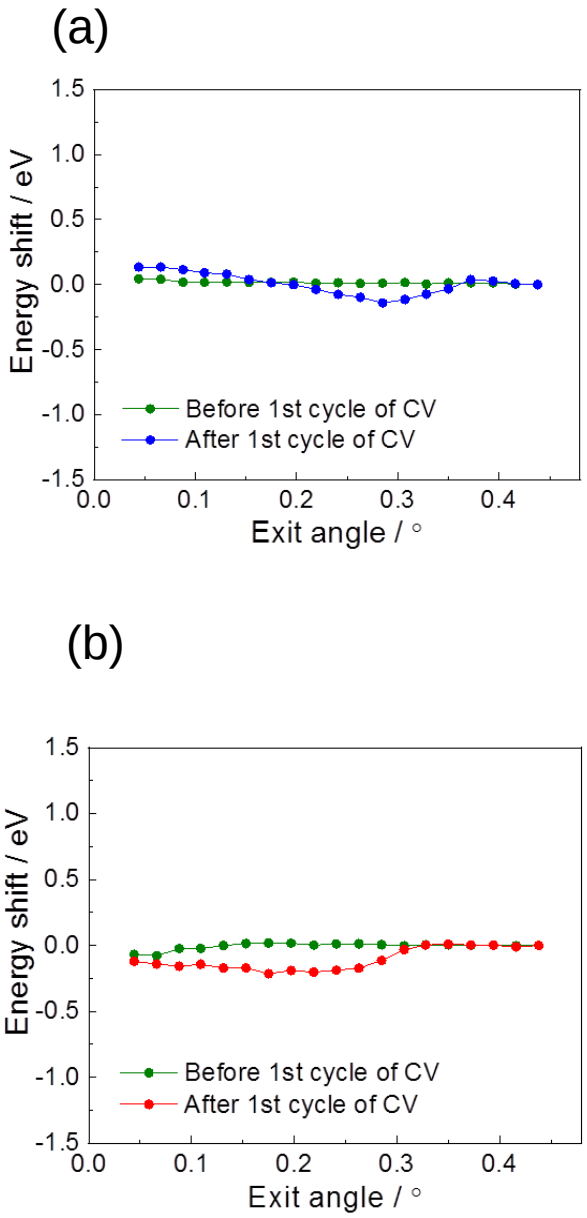

Figure 2.9 Energy shift of that before and after 1st cycle of CV measurement for both thin-film electrodes (a) without and (b) with interlayer at Mn *K*-edge.

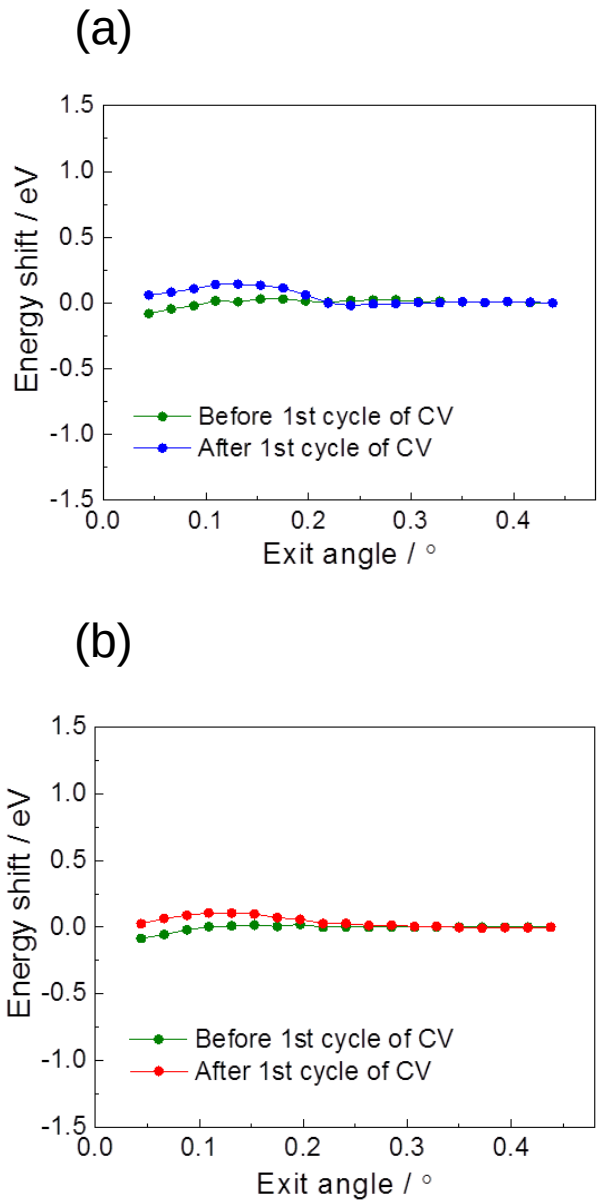

Figure 2.10 Energy shift of that before and after 1st cycle of CV measurement for both thin-film electrodes (a) without and (b) with interlayer at Ni *K*-edge.

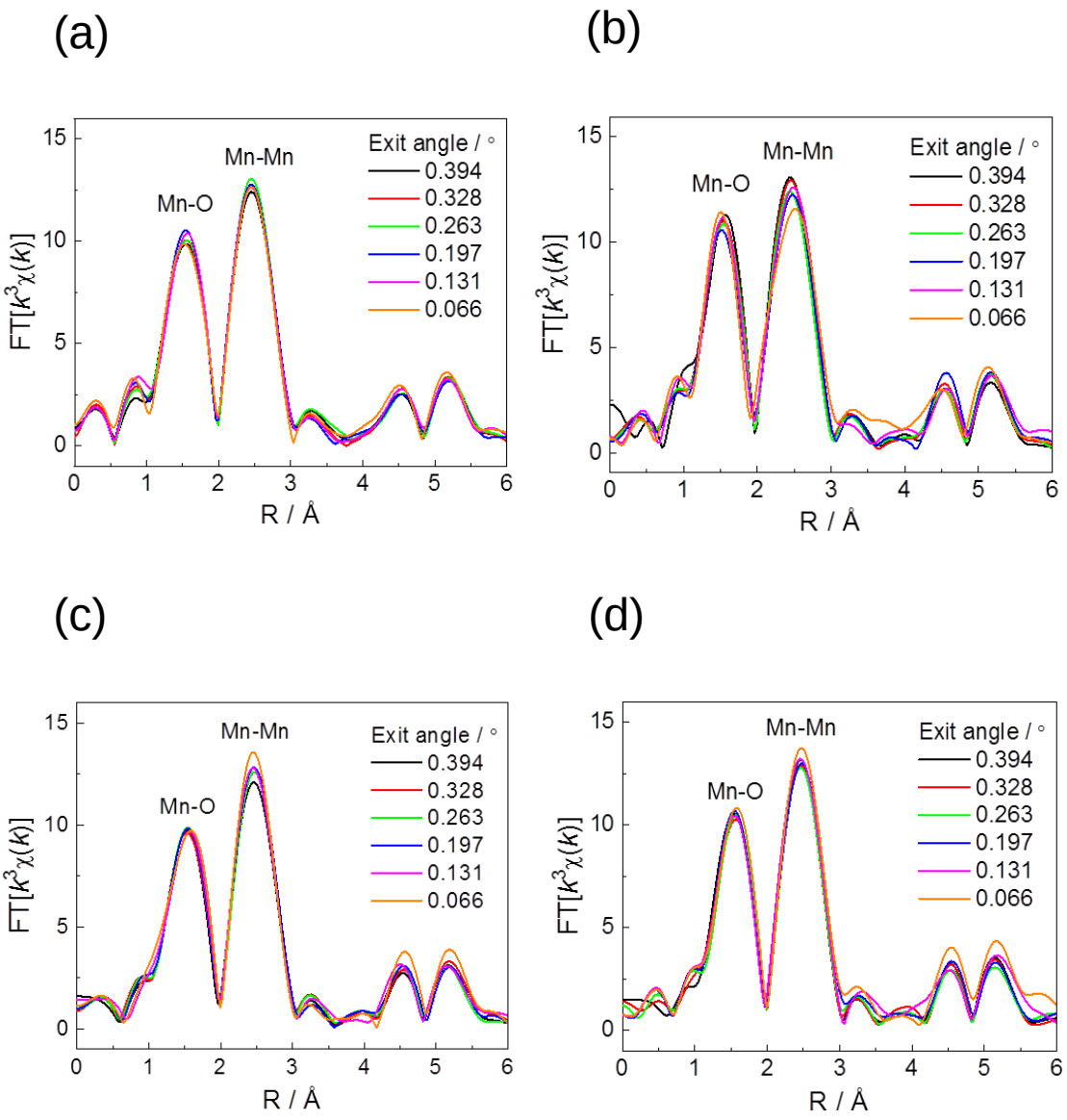

Figure 2.11 Fourier transform of the k^3-weighted DR-EXAFS of Mn *K*-edge in$LiNi_{0.5}Mn_{1.5}O_4$ thin film electrode before charging (a) before 1st cycle of CV measurement with interlayer (b) after 1st cycle of CV measurement with interlayer (c) before 1st cycle of CV measurement without interlayer (d) after 1st cycle of CV measurement without interlayer.

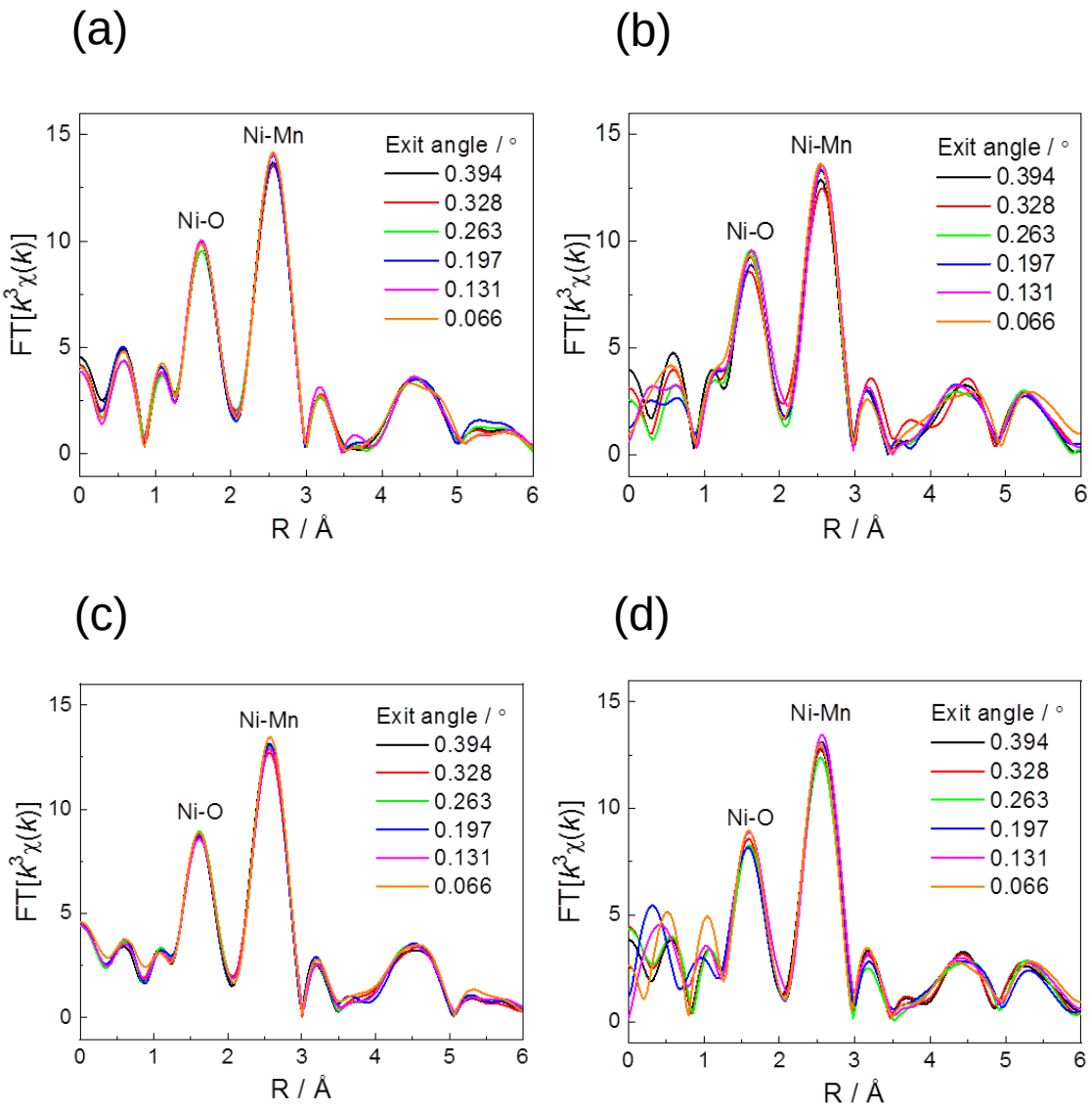

Figure 2.12 Fourier transform of the k^3-weighted DR-EXAFS of Ni *K*-edge in$LiNi_{0.5}Mn_{1.5}O_4$ thin film electrode before charging (a) before 1st cycle of CV measurement with interlayer (b) after 1st cycle of CV measurement with interlayer (c) before 1st cycle of CV measurement without interlayer (d) after 1st cycle of CV measurement without interlayer.

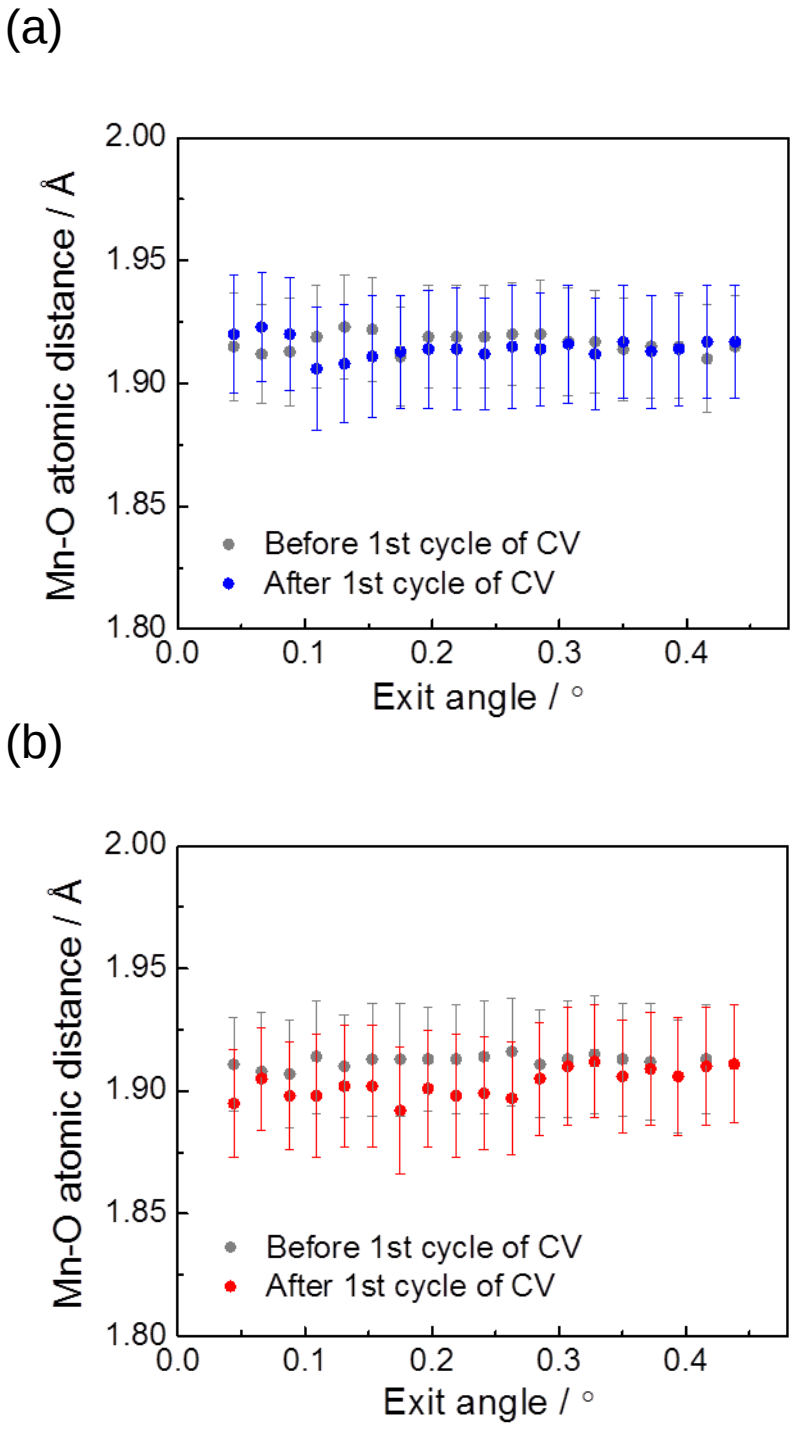

Figure 2.13 Mn-O bond distance of thin-film electrodes (a) without interlayer and (b) with interlayer measured before and after 1st cycle of CV measurement.

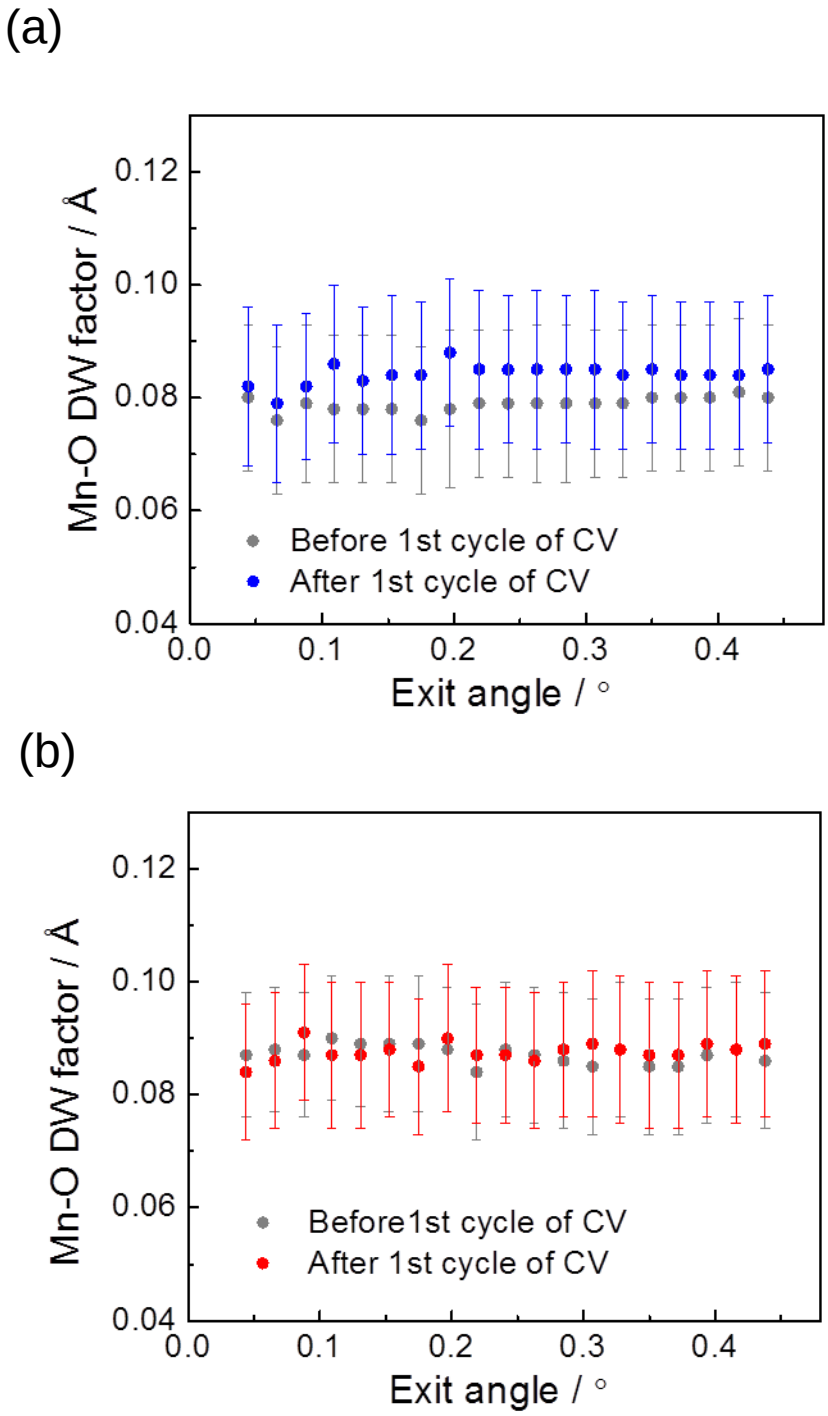

Figure 2.14 DW factor of Mn-O bond of thin-film electrodes (a) without interlayer and (b) with interlayer measured before and after 1st cycle of CV measurement.

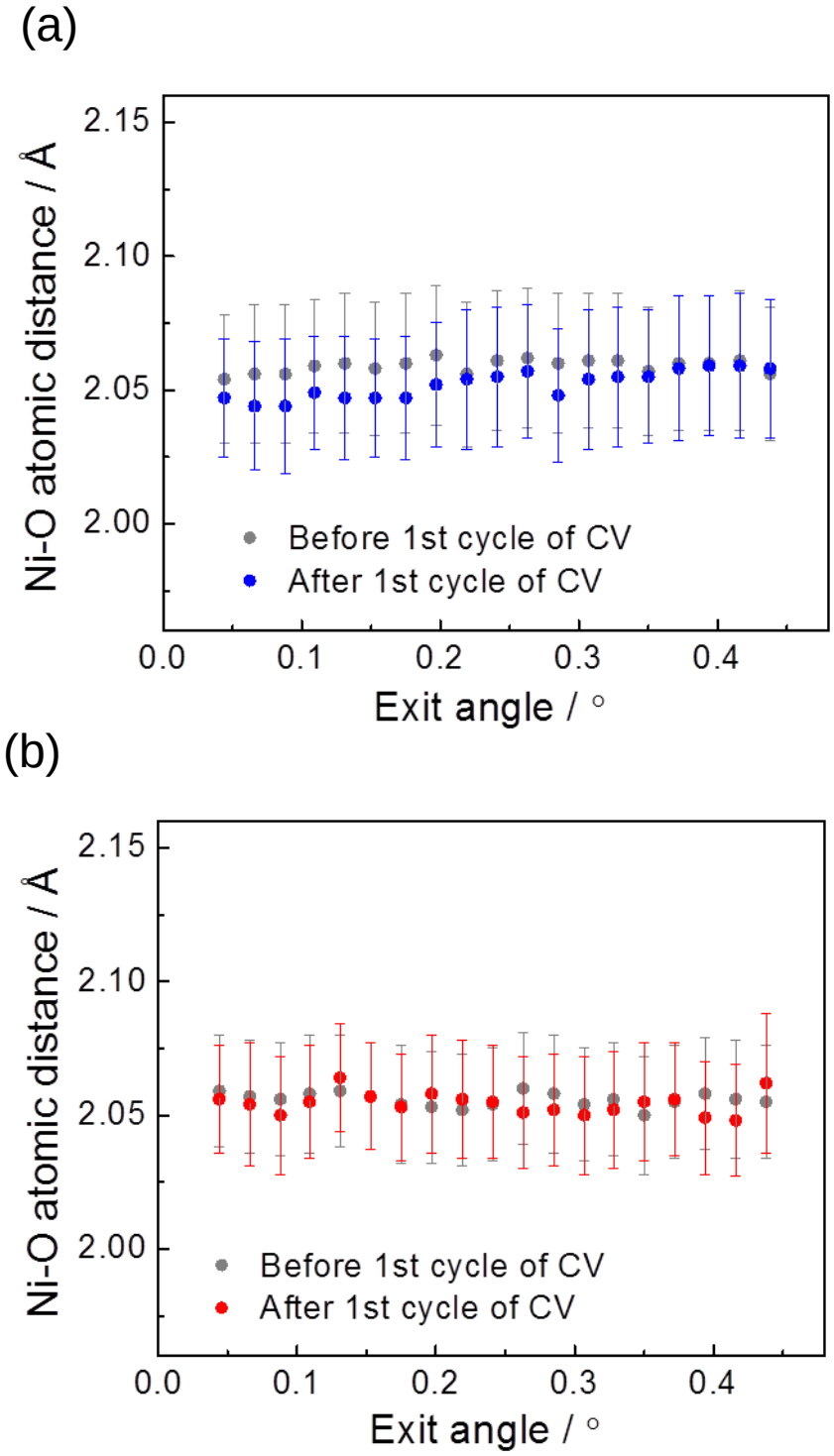

Figure 2.15 Ni-O bond distance of thin-film electrodes (a) without interlayer and (b) with interlayer measured before and after 1st cycle of CV measurement.

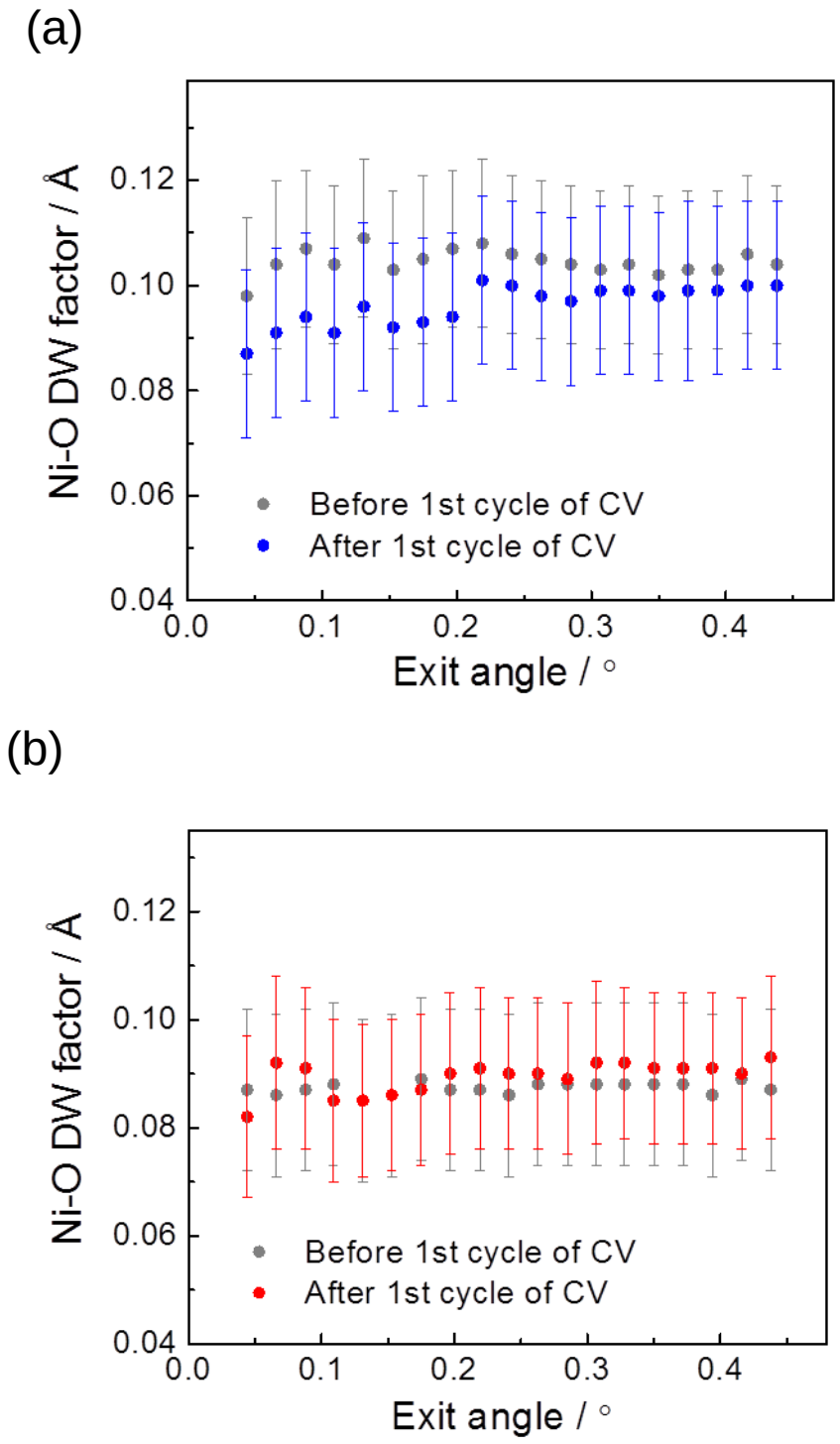

Figure 2.16 Ni-O DW factor of thin-film electrodes (a) without interlayer and (b) with interlayer measured before and after 1st cycle of CV measurement.

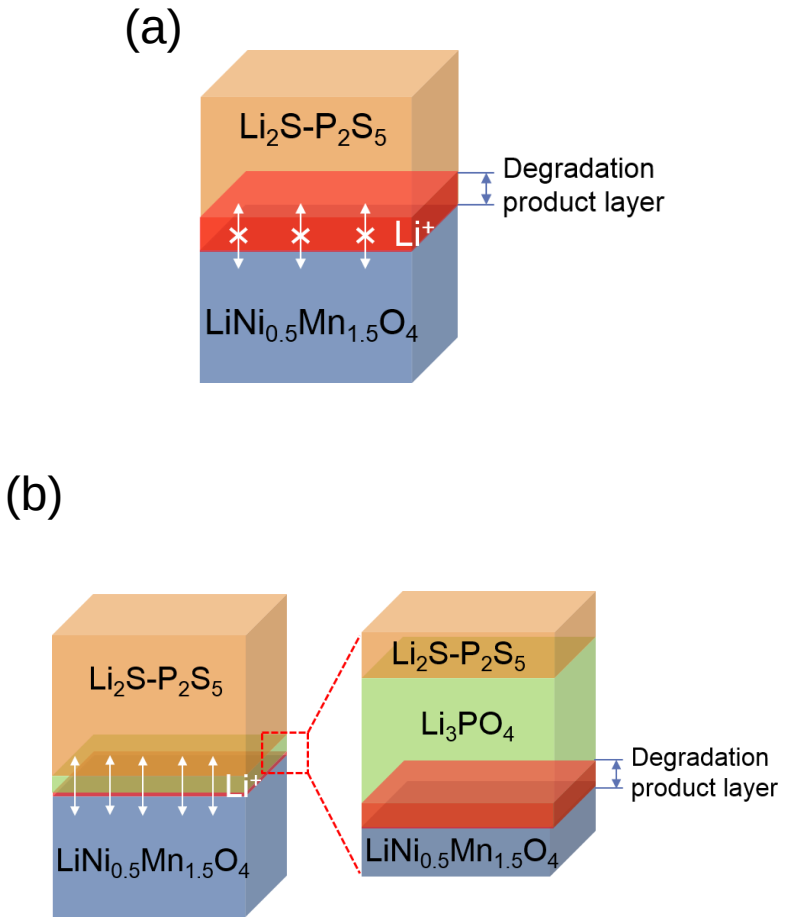

Figure 2.17 Reaction mechanism of thin-film electrodes (a) without and (b) with interfacial modification during charge and discharge process.

References

(1) A. M. Haregewoin, A. S. Wotango, B. J. Hwang, *Energy Environ. Sci.* 2016, **9**, 1955-1988.

(2) A. Manthiram, X. W. Yu, S. F. Wang, *Nat. Rev. Mater.* 2017, **2**, 16103.

(3) Q. Zhong, A. Bonakdarpour, M. Zhang, Y. Gao, J. R. Dahn, *J. Electrochem. Soc.* 1997, **144**, 205-213.

(4) T. Ohzuku, K. Ariyoshi, S. Yamamoto, Y. Makimura, *Chem. Lett.* 2001, **12**, 1270-1271.

(5) K. Ariyoshi, Y. Iwakoshi, N. Nakayama, T. Ohzuku, *J. Electrochem. Soc.* 2004, **151**, A296-A303.

(6) H. Morimoto, H. Awano, J. Terashima, Y. Shindo, S. Nakanishi, V. Ito, K. Ishikawa, S. Tobishima, *J. Power Sources* 2013, **240**, 636-643.

(7) M. Tatsumisago, M. Nagao, A. Hayashi, *J. Asian Ceramic Societies* 2013, **1**, 17-25.

(8) N. Ohta, K. Takada, I. Sakaguchi, L. Zhang, R. Ma, K. Fukuda, M. Osada, T. Sasaki, *Electrochem. commun.* 2007, **9**, 1486-1490.

(9) N. Ohta, K. Takada, L. Zhang, R. Ma, M. Osada, T. Sasaki, *Electrochem. commun.* 2006, **18**, 2226-2229.

(10) Y. Sakurai, A. Sakuda, A. Hayashi, M. Tatsumisago, *Solid State Ionics* 2011, **182**, 59-63.

(11) Y. Ito, Y. Sakurai, S. Yubuchi, A. Sakuda, A. Hayashi, M. Tatsumisago, *J. Electrochem. Soc.* 2015, **162**, A1610-A1616.

(12) K. Takada, N. Ohta, L. Zhang, K. Fukuda, I. Sakaguchi, R. Ma, M. Osada, T. Sasaki, *Solid State Ionics* 2008, **179**, 1333-1337.

(13) N. Machida, J. Kashiwagi, M. Naito, T. Shigematsu, *Solid State Ionics* 2012, **225**, 354-358.

(14) S. T. Myung, K. Izumi, S. Komaba, Y. K. Sun, H. Yashiro, N. Kumagai, *Chem. Mater.* 2005, **17**, 3695-3704.

(15) S. Yubuchi, Y. Ito, T. Matsuyama, A. Hayashi, M. Tatsumisago, *Solid State Ionics* 2016, **285**, 79-82.

(16) G. Oh, M. Hirayama, O. Kwon, K. Suzuki, R. Kanno, *Chem. Mater.* 2016, **28**, 2634-2640.

(17) K. Takada, N. Ohta, L. Zhang, K. Fukuda, I. Sakaguchi, R. Ma, M. Osada, T. Sasaki, *Solid State Ionics* 2008, **179**, 1333-1337.

(18) J. Haruyama, K. Sodeyama, L. Han, K. Takada, Y. Tateyama, *Chem. Mater.* 2014, **26**, 4248-4255.

(19) A. Sakuda, A. Hayashi, M. Tatsumisago, *Chem. Mater.* 2010, **22**, 949-956.

(20) D. Takamatsu, T. Nakatsutsumi, S. Mori, Y. Orikasa, M. Mogi, H. Yamashige, K. Sato, T. Fujimoto, Y. Takamashi, H. Murayama, M. Oishi, H. Tanida, T. Uruga, H. Arai, Y. Uchimoto, Z. Ogumi, *J. Phys. Chem. Lett.* 2011, **2**, 2511-2514.

(21) S. Yubuchi, Y. Ito, T. Matsuyama, A. Hayashi, M. Tatsumisago, Solid State Ionics 2016, **285**, 79-82.

(22) A. Sakuda, A. Hayashi, S. Hama, M. Tatsumisago, *J. Am. Ceram. Soc.* 2010, **93**, 765-768.

(23) Q. Zhong, A. Bonakdarpour, M. Zhang, Y. Gao, J. R. Dahn, *J. Electrochem. Soc.* 1997, **144**, 205-213.

(24) K. Kanamura, W. Hoshikawa, T. Umegaki, *J. Electrochem. Soc.* 2002, **149**, A339-A345.

(25) W. D. Richards, L. J. Miara, Y. Wang, J C. Kim, G. Ceder, *Chem. Mater.* 2016, **28**, 266-273.

(26) T. Okumura, T. Nakatsutsumi, T. Ina, Y. Orikasa, H. Arai, T. Fukutsuka, Y. Iriyama, T. Uruga, H. Tanida, Y. Uchimoto, Z. Ogumi, *J. Mater. Chem.* 2011, **21**, 10051-10060.

Chapter 3. Elucidation of the Effect of Introducing LiF Interlayer into $LiNi_{0.5}Mn_{1.5}O_4$/Li_2S-P_2S_5 Interface in All-Solid-State Battery

3.1. Introduction

Due to their outstanding safety, high gravimetric and volumetric energy density comparison to traditional liquid electrolyte based systems, all-solid-state lithium-ion batteries using sulfide solid electrolytes are highly considered to replace the conventional lithium ion batteries. It is necessary to apply high-voltage cathode materials to all-solid-state lithium-ion batteries in order to improve their energy density.[1-3]

Among various kinds of cathode materials, spinel structure $LiNi_{0.5}Mn_{1.5}O_4$ is attracting increasing attention owing to its outstanding high operating voltage of 4.7 V (vs Li/Li^+).[4,5] However, one of the biggest problems limiting the improvement of all-solid-state battery is the high interfacial resistance between electrode and solid state electrolyte.[6] Since the interfacial resistance is considered as a result of electrochemical potential gap between electrode and solid state electrolyte[7], the influence of interfacial resistance is more serious in all-solid-state batteries using high voltage cathode such as $LiNi_{0.5}Mn_{1.5}O_4$. Therefore, the method which can reduce the interfacial resistance is becoming the key point to realize the application of all-solid-state batteries using high

voltage.

So far, interfacial modification has been used as an effective method to reduce the interfacial resistance.[8] Besides the oxide such as ZrO_2[9] and Al_2O_3[10], oxide lithium ionic solid electrolyte such as $LiNbO_3$[11], $Li_4Ti_5O_{12}$[12] and Li_4SiO_4[13] are also used as the interlayer between the cathode and solid state electrolyte in interfacial modification. Yubuchi *et al.*[14] showed that Li_3PO_4-coated $LiNi_{0.5}Mn_{1.5}O_4$ could exhibit lower interfacial resistance and a better rate performance in all-solid-state battery using $80Li_2S \cdot 20P_2S_5$ sulfide solid electrolyte. Oh *et al.*[15] reported that $LiNbO_3$ could reduce the interfacial resistance between $LiNi_{0.5}Mn_{1.5}O_4$ and $Li_{10}GeP_2S_{12}$. In recent years, LiF under specific fabrication condition has been found to be conductive for lithium ions[16]. Since the LiF is considered to be highly stable even under high voltage. The LiF interlayer is a promising candidate for interfacial modification. However, the effect and detailed mechanism of LiF using as interlayer between high voltage cathode and solid state electrolyte still remain unclear.

So far, two main hypotheses have been proposed as the origin of the interfacial resistance: (1) space-charge layer theory and (2) reaction product layer theory. For space-charge layer theory, based on electrochemical analysis[17] and theoretical calculation,[18] a space-charge layer was considered to form at the interface due to the gap of lithium electrochemical potential between oxide cathode and sulfide electrolyte. For product layer theory, based on transmission electron microscopy (TEM) observation and energy dispersive X-ray spectrometry (EDX) analysis of the interface,[19] a reaction product layer was considered to form at interface due to the

mutual diffusion of elements between cathode and electrolyte during charge/discharge process.

X-ray absorption spectroscopy (XAS) is an useful method to analyze electronic and local structures of a certain atom, and especially depth-resolved XAS (DR-XAS) technique has been proved to be an effective method to examine those structures at the interface.[20,21]

In this study, the effect of LiF interlayer for interfacial modification in all-solid-state batteries using sulfide solid state electrolyte was confirmed by electrochemical methods. Combining the electrochemical methods and DR-XAS technique, the mechanism of LiF interlayer was analyzed when comparing to $LiPO_3$ interlayer in the respect of electronic and local structures at high voltage. Since the LiF is not a frequently used coating material for cathode in lithium ion batteries, the investigation of suitable manufacture condition of LiF has also been carried out in this work.

Model thin-film electrodes were fabricated by pulsed laser deposition using $LiNi_{0.5}Mn_{1.5}O_4$ and $80Li_2S{\cdot}20P_2S_5$ as cathode and solid-state electrolyte, and Li_3PO_4 or LiF as the interlayer material. Then, their electrochemical performances were studied by using cyclic voltammetry (CV) and electrochemical impedance spectroscopy (EIS). Finally, the interface status of both thin-film electrodes were compared before and after charge/discharge cycle using DR-XAS technique. Our study revealed that LiF interlayer stabilizes the interfacial structure between $LiNi_{0.5}Mn_{1.5}O_4$/$80Li_2S{\cdot}20P_2S_5$, which leads to lower interfacial resistance and higher durability during charge/discharge processes.

3.2. Experimental Section

3.2.1. Investigation of fabrication condition for LiF interlayer

The crystal structure of LiF deposited under different temperature (room temperature, 473 K, 573 K, 673 K and 773 K) was confirmed by X-ray diffraction (XRD). Various temperature of substrates for LiF thin film fabrication by PLD method were attempted to find the best temperature condition. The influence of deposition temperature was investigated by CV using a three-electrode cell in which LiF-coated $LiNi_{0.5}Mn_{1.5}O_4$ was used as cathode and lithium metal was used as anode. The CV measurement was carried out for 3 cycles from 3.5 V to 5.0 V with a sweep speed of 0.1 mV s^{-1}. The deposition time for LiF thin film was investigated by scanning electron microscope (SEM) and EDX. The morphology of LiF thin films deposited on mirror-polished quartz substrates during different times were observed by SEM and the distribution condition was confirmed by EDX.

3.2.2. Sample preparation

Both thin-film electrodes (without interlayer, with Li_3PO_4 interlayer and with LiF interlayer) were prepared by pulsed laser deposition (PLD) method. The diagrammatic sketches of the thin-film model electrodes are shown in Figure 3.1. To supply the sufficient Li amount during PLD deposition, the PLD targets for $LiNi_{0.5}Mn_{1.5}O_4$ thin films consisted of $LiNi_{0.5}Mn_{1.5}O_4$ (Sigma-Aldrich Co., LLC) with 5 w% Li_2O (Sigma-Aldrich Co., LLC.). The targets

were sintered at 773 K for 6 h. The $LiNi_{0.5}Mn_{1.5}O_4$ thin films were deposited on mirror-polished polycrystalline platinum substrates (15 mm × 15 mm × 2 mm) under an oxygen pressure of 26 Pa for 30 min. The substrates were heated at a temperature of 873 K. A Nd:YAG laser (λ = 266 nm) with a repeating frequency of 10 Hz were used for the laser ablation. The laser energy density was set to 3.5 J cm^{-2} at the target. The PLD target for LiF interlayers were prepared by sintering LiF (Sigma-Aldrich Co., LLC.) at 573 K for 8 h. The LiF thin films were deposited on the $LiNi_{0.5}Mn_{1.5}O_4$ films at 673 K under an argon pressure of 26 Pa for 26 min. A Nd:YAG laser (λ = 266 nm) with a repeating frequency of 10 Hz were used for the laser ablation. The laser energy density was set to 2 J cm^{-2} at the target. The PLD target for $80Li_2S{\cdot}20P_2S_5$ layer consisted of Li_2S (99.9%, Idemitsu Kosan Co. Ltd.) and P_2S_5 (99%, Aldrich Chemical Co., Inc.) with a molar ratio of 80:20. The $80Li_2S{\cdot}20P_2S_5$ thin films were deposited on $LiNi_{0.5}Mn_{1.5}O_4$ films or LiF interlayer at room temperature under an argon pressure of 5 Pa for 140 s. A KrF excimer laser (λ = 266 nm) with a repeating frequency of 5 Hz were used for the laser ablation. The laser energy density was set to 2 J cm^{-2} at the target.[22]

3.2.3. Electrochemical measurements

Cyclic voltammetry were carried out for the thin-film electrodes with and without LiF interlayer by using a three-electrode cell as shown in Figure 1.2. To minimize the influence of interface between anode and solid electrolyte, the cell were simplified by

using liquid electrolyte. The thin-film electrode was used as working electrode. The Li_3PO_4 protective layers were deposited on the top to restrain the dissolving of $80Li_2S{\cdot}20P_2S_5$ into the liquid electrolyte. Lithium metals were used as both counter electrode and reference electrode. 1 M $LiPF_6$ in ethylene carbonate and ethyl methyl carbonate (EC : EMC = 3:7 v/v %) was used as the liquid electrolyte.

The CV measurement was carried out for 10 cycles from 3.5 V to 5.0 V with a sweep speed of 0.1 mV s^{-1}. Electrochemical impedance spectroscopy (EIS) was carried out for analyzing the change of interfacial resistance during charge/discharge process by using the same cell configuration as CV measurement during four charge/discharge cycles. The amplitude was 30 mV and the scan range was from 10^{-2} Hz to 10^{6} Hz. The potential of EIS measurement points were 4.4 V-5.0 V versus Li/Li^+ during both charge/discharge, respectively. Before each EIS measurement point, the cathode was set at the target potential by linear sweep voltammetry and kept at that potential for 30 min by the charge or discharge current change becomes sufficient small.

3.2.4. Depth-resolved X-ray Absorption Spectroscopy Measurements

In this study, to compare the change of interface before and after charge/discharge process, the thin-film electrodes with and without interlayer were both analyzed by DR-XAS at two measurement points: (1) as-prepared and (2) after the 1st cycle of CV measurement. Thin-films after 1st cycle of CV measurement refers to thin-films that were charged from open circuit potential (OCP) to 5.0 V (vs. Li/Li^+) and then discharged

to 3.5 V (vs. Li/Li^+). DR-XAS measurements of Ni *K*-edge and Mn *K*-edge in $LiNi_{0.5}Mn_{1.5}O_4$ cathode were carried out in BL37XU (SPring-8, Japan) with a two-dimensional pixel array detector, Pilatus (Dectris Ltd.) for detecting the exit X-ray fluorescence. Thin-film electrodes after charge/discharge process were taken out from the three-electrodes cells, washed by EC:EMC and dried, then set into a custom-made cell which can be vacuumed to 10^{-3} Pa and can pass incident and exit X-ray. All of the operations mentioned above were carried out in glove box with argon atmosphere.

3.3. Results and discussion

3.3.1 Fabrication condition for LiF thin film

The results of XRD measurement are shown in Figure 3.2. It indicated that crystal LiF thin film could be fabricated under different termperature. The results of CV measurement for LiF thin film deposited under different substrate temperature are shown in Figure 3.3.The relative low oxidation current at high voltage indicated that 673K was the best deposition temperature of LiF thin film used as interlayer. The results of SEM and EDX are shown in Figure 3.4 and Figure 3.5. As the deposition time extended, the LiF was becoming well-distributed in SEM and EDX results. And when the deposition time was 26 min, the LiF thin film could cover the whole surface.

3.3.2. Electrochemical measurement

Electrochemical properties of the prepared thin-film electrodes without interlayer, with Li_3PO_4 interlayer and with LiF interlayer were evaluated with CV and EIS

measurements. The cyclic voltammograms of both thin-film electrodes were shown in Figure 3.6. The anodic and cathodic peaks corresponding to a redox reaction of Mn^{3+}/Mn^{4+} were detected at 4.0 V. Another two pairs of reversible redox peaks observed at 4.7 V and 4.8 V represent the redox reactions of Ni^{2+}/Ni^{3+} and Ni^{3+}/Ni^{4+}, respectively.[23,24] Also, the oxidation current attributed to oxidation decomposition of electrolyte was observed at high voltage range (4.8 V ~ 5.0 V).

The oxidation current attributed to the electrolyte decomposition was reduced for the thin-film with LiF interlayer, meaning that interlayer suppressed the electrolyte decomposition. The discharge capacities and coulombic efficiency of both thin-film electrodes based on CV measurements were plotted against the cycle number in Figure 3.7(a) and Figure 3.7(b), respectively. The discharge capacity of thin-film electrode without interlayer gradually decreased from 3.5 to 1.6 mC with cycling (1nd cycle ~ 9th cycle). In contrast, the discharge capacity of the thin-film electrode with LiF interlayer was kept at about 5.7 mC (1nd cycle ~ 9th cycle), it showed higher discharge capacity retention than thin-film electrode without interlayer. The introduction of the LiF interlayer improves the coulombic efficiency of $LiNi_{0.5}Mn_{1.5}O_4$ to about 85% from 1nd cycle to 9th cycle. These results suggest that interface modification with LiF interlayer can improve the cyclability of $LiNi_{0.5}Mn_{1.5}O_4$ cathode when using $80Li_2S \cdot 20P_2S_5$ solid electrolyte.

The interfacial resistance of the thin-film electrode without interlayer was lower than that of thin-film electrode with LiF interlayer at initial state. (Figure 3.8) However,

it showed an increasing trend from 1st cycle to 4th cycle due to the formation of a new interfacial layer caused by electrolyte decomposition. And the interfacial resistance of the thin-film with LiF interlayer was higher due to the existence of LiF interlayer at initial state, it kept decreasing during charge/discharge processes. These results indicates that introduction of LiF interlayer can restrain the increase of interfacial resistance during charge/discharge process. According to the results of both CV and EIS measurement, it suggests that the interfacial modification by LiF interlayer can reduce side reaction at the interface between $LiNi_{0.5}Mn_{1.5}O_4$ cathode and $80Li_2S{\cdot}20P_2S_5$ solid electrolyte and improve the electrochemical performance.

3.3.3. Depth-resolved X-ray Absorption Spectroscopy Measurements

In order to investigate the electronic and local structures of the cathode/electrolyte interface before and after charge/discharge process, DR-XAS measurements for Mn *K*-edge and Ni *K*-edge was conducted for both thin-films. In the DR-XAS measurement, which has a depth resolution of 3-4 nm, XAS spectra gained at lower exit angles provide more information about the surface of a thin film, whereas XAS spectra gained at higher exit angles provide more information about the bulk properties.[20,26] The schematic diagram of DR-XAS was shown in Figure 1.10.

In general, an energy shift of the absorption edge towards lower energy means that the oxidation state of the ions decreased. The relative energy in the half of the normalized absorbance of the XANES obtained from each exit angle to the XANES

obtained from the exit angle of 0.438°, from which reflected sufficiently on the bulk information, was plotted against each exit angle. The relative energy of the Mn *K*-edge XANES of both thin-film electrodes before and after one potentiostatic cycle was shown in Figure 3.9(a) and 3.9(b), respectively. The relative energy of the Ni *K*-edge XANES of both thin-film electrodes before and after one potentiostatic cycle was shown in Figure 3.10(a) and 3.10(b), respectively. For both Mn *K*-edge and Ni *K*-edge, there was no obvious change of the relative energy before and after one potentiostatic cycle between cathode bulk and interface in both thin-films. These results mean that the oxidation state of Mn ions and Ni ions almost kept steady from the interface to the bulk before and after one potentiostatic cycle neither with or without LiF interlayer. These results mean that the local structure around Mn ions and Ni ions almost kept steady from the interface to the bulk before and after one potentiostatic cycle neither with or without LiF interlayer .

3.3.4. Effect of LiF interlayer

According to the results of both electrochemical and DR-XAS measurement, we discuss the interfacial phenomenon between $LiNi_{0.5}Mn_{1.5}O_4$ /Li_2S-P_2S_5, and the effect of the introducing Li_3PO_4 and LiF interlayer into the interface. As the summary, we propose the interfacial phenomenon mechanism diagrammatically in Figure 3.11.

For the thin-film without interlayer, the electrochemical measurements showed that the interfacial resistance increased and the discharge capacity decreased with cycling number. The DR-XAS measurement showed that the electronic and local

structures at the interface did not change after potentiostatic cycling. These results indicate that the degradation of the electrochemical performance is caused by decomposition of the electrolyte (Figure 3.11(a)). Li_2S-P_2S_5 is thermodynamically unstable at the redox potential of $LiNi_{0.5}Mn_{1.5}O_4$ (4.7 V vs. Li/Li^+) because the potential window of Li_2S-P_2S_5 is 2.1 V ~ 2.6 V. [25]

For the thin-film with Li_3PO_4 interlayer, although the electronic and local structures at the interface did not change after potentiostatic cycling, the increase of the interfacial resistance and the degradation with cycle number were suppressed. These results indicate that the Li_3PO_4 interlayer suppresses the decomposition of Li_2S-P_2S_5, leading to better electrochemical performance. Although Li_3PO_4 has a wider potential window (0.69 ~ 4.2 V vs. Li/Li^+) than the sulfide solid electrolyte,[25] the Li_3PO_4 interlayer become thermodynamically unstable in the redox potential of $LiNi_{0.5}Mn_{1.5}O_4$.[27] Thus, we suggest that the Li_3PO_4 interlayer also decomposes at the redox potential of $LiNi_{0.5}Mn_{1.5}O_4$ to form the productive layer, which stabilizes the interfacial structure kinetically to suppress the increase of the interfacial resistance (Figure 3.11(b)).. However because the productive layer is thermodynamically unstable at the high potential, the decomposition reaction of the Li_3PO_4 interlayer proceeds during charge/discharge process, resulting in insufficient coulombic efficiency.

For the thin-film with LiF interlayer, although the electronic and local structures at the interface did not change after potentiostatic cycling, the increase of the interfacial resistance and the degradation with cycle number were suppressed. These results

indicate that the LiF interlayer suppresses the decomposition of Li_2S-P_2S_5, leading to better electrochemical performance. Since LiF has a wider potential window (0 ~ 6.4 V vs. Li/Li^+) than the sulfide solid electrolyte,[25] the LiF interlayer kept thermodynamically stable in the redox potential of $LiNi_{0.5}Mn_{1.5}O_4$[26] (Figure 3.11(c)).

3.4. Conclusion

We examined the interfacial reaction between $LiNi_{0.5}Mn_{1.5}O_4$ cathode and $80Li_2S \cdot 20P_2S_5$ electrolyte, and also effect of introducing LiF interlayer into the interface using electrochemical and DR-XAS measurements. The introduction of LiF interlayer improved the cyclability and decreased the interfacial resistance. Since the LiF interlayer is thermodynamically stable under operating potential of $LiNi_{0.5}Mn_{1.5}O_4$, it can restrain the decomposition of sulfide electrolyte, resulting in improvement of the electrochemical performance.

(a)

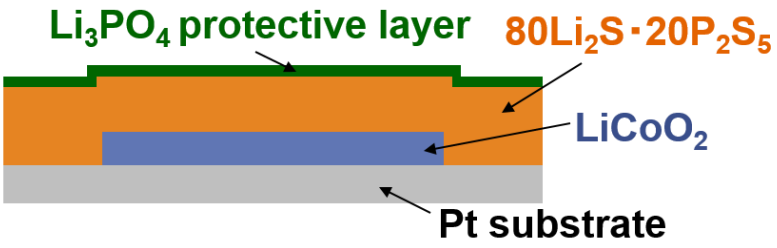

(b)

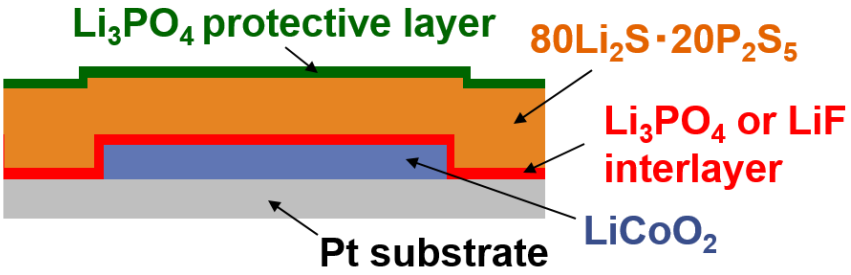

Figure 3.1 Diagrammatic sketch of the thin-film model electrodes (a) without and (b) with Li_3PO_4 or LiF interlayer.

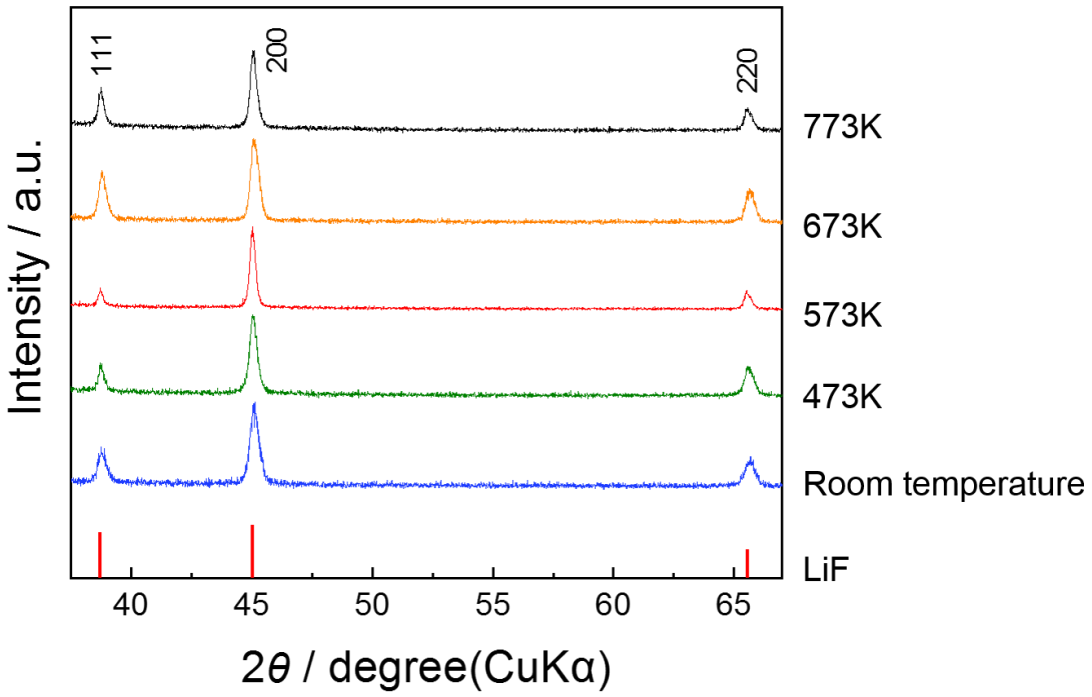

Figure 3.2 XRD pattern of the LiF thin-film deposited under different temperature of substrate.

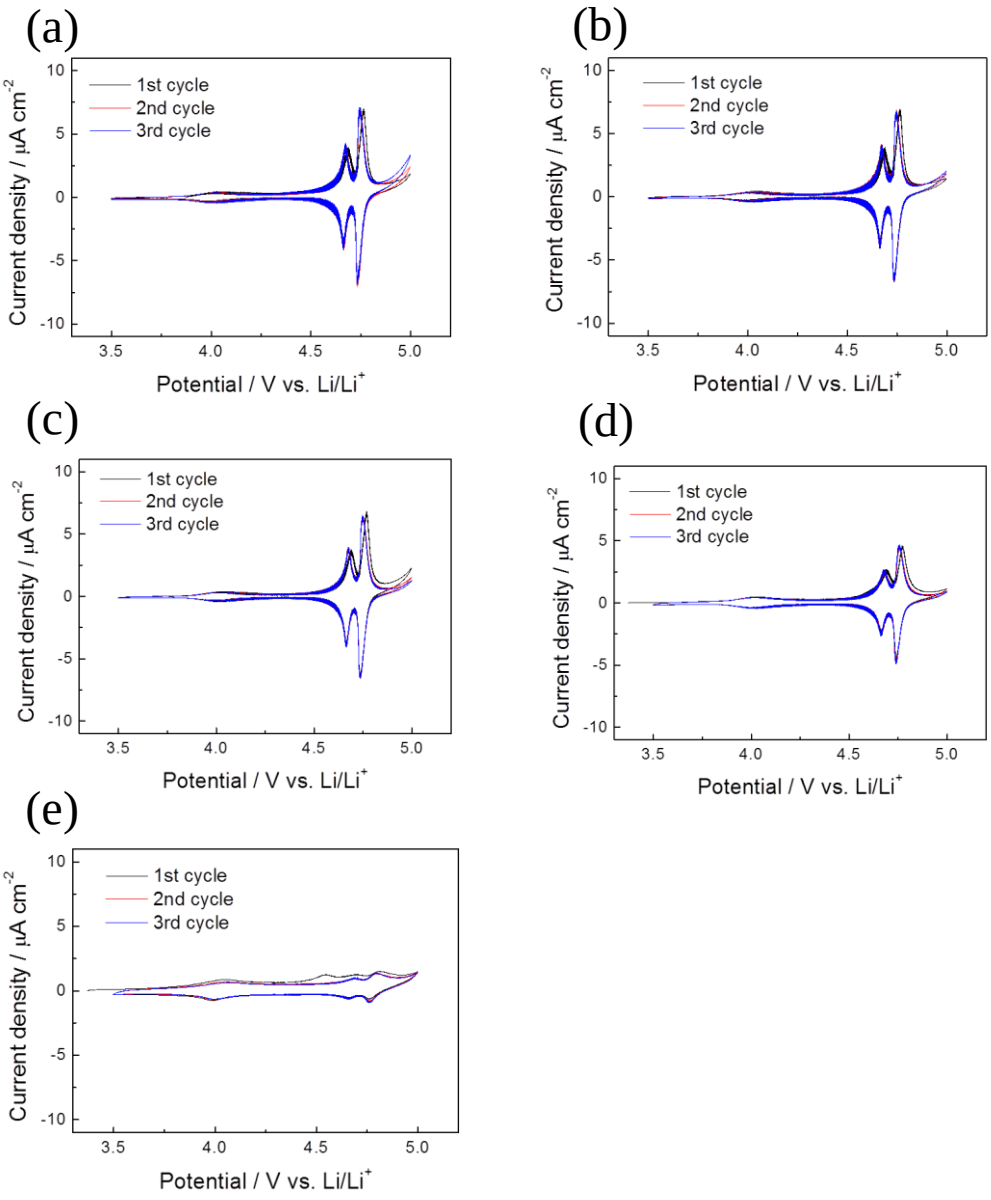

Figure 3.3 CV curves of three-electrode cells using LiF under different deposition temperature as coated layer for $LiNi_{0.5}Mn_{1.5}O_4$. (a) room temperature, (b) 473 K, (c) 573 K, (d) 673 K and (e) 773 K.

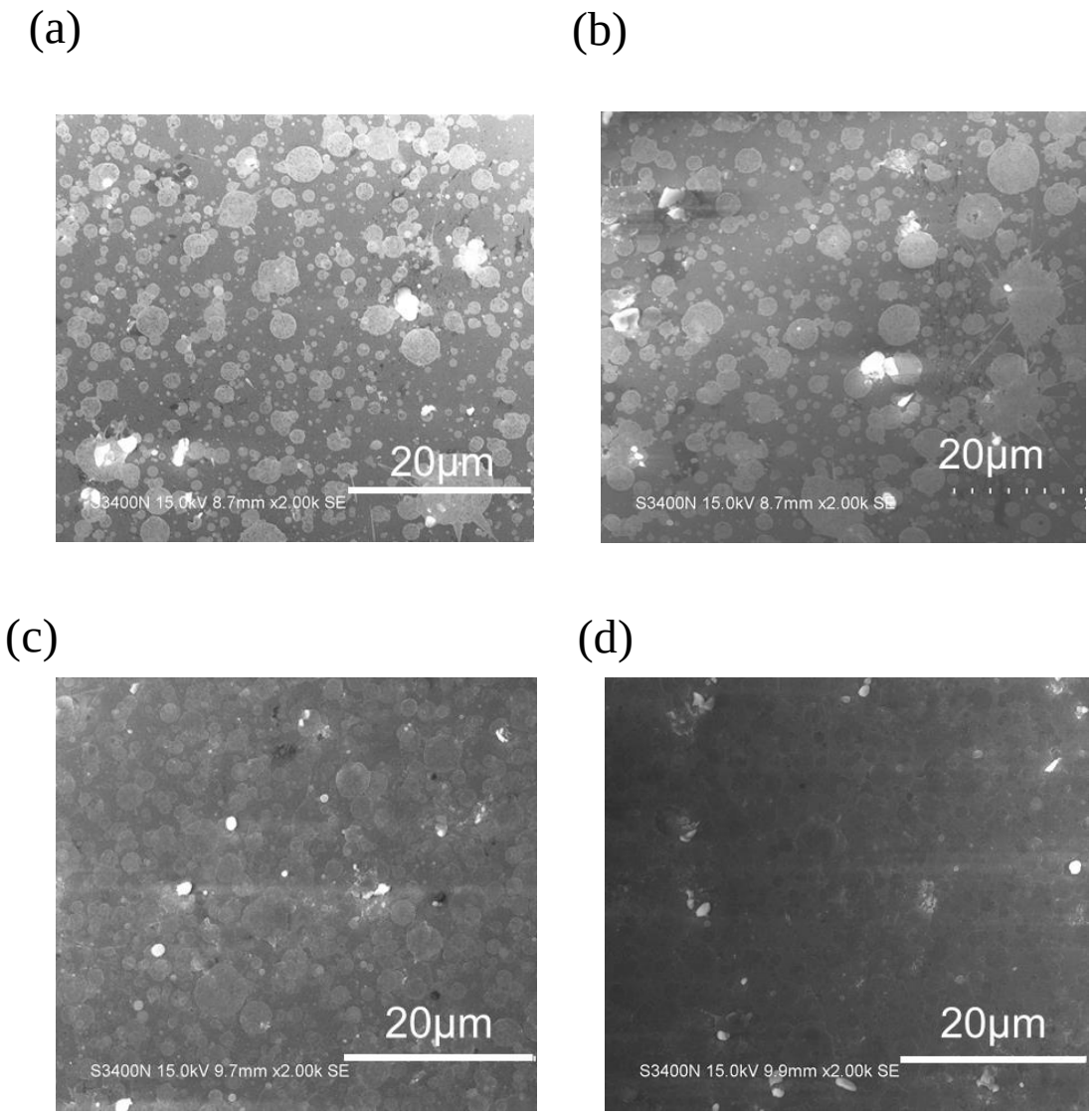

Figure 3.4 SEM images of LiF thin-film under different deposition time (a) room temperature, (b) 6.5 min, (c) 13 min, (d) 19.5 min and (e) 26 min.

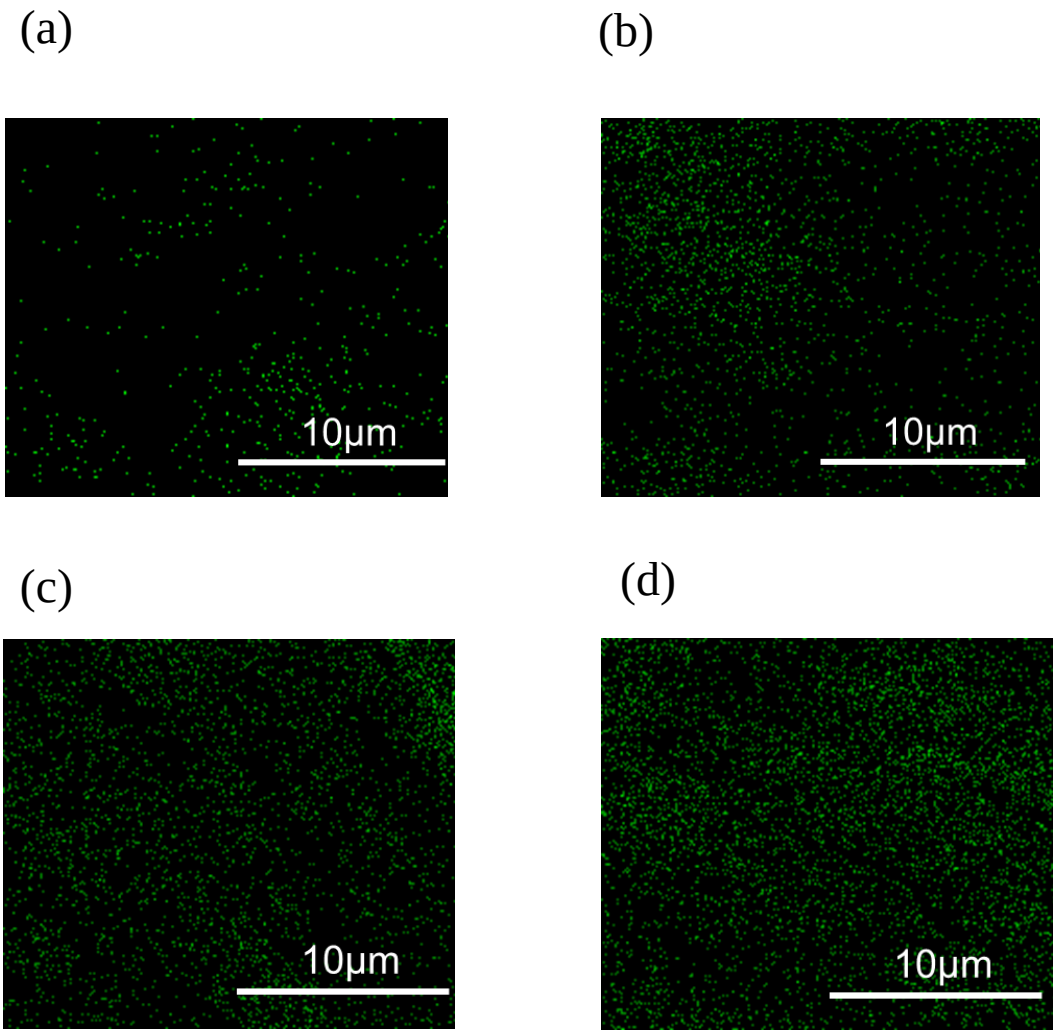

Figure 3.5 EDX images of fluorine from LiF thin-film under different deposition time (a) room temperature, (b) 6.5 min, (c) 13 min, (d) 19.5 min and (e) 26 min.

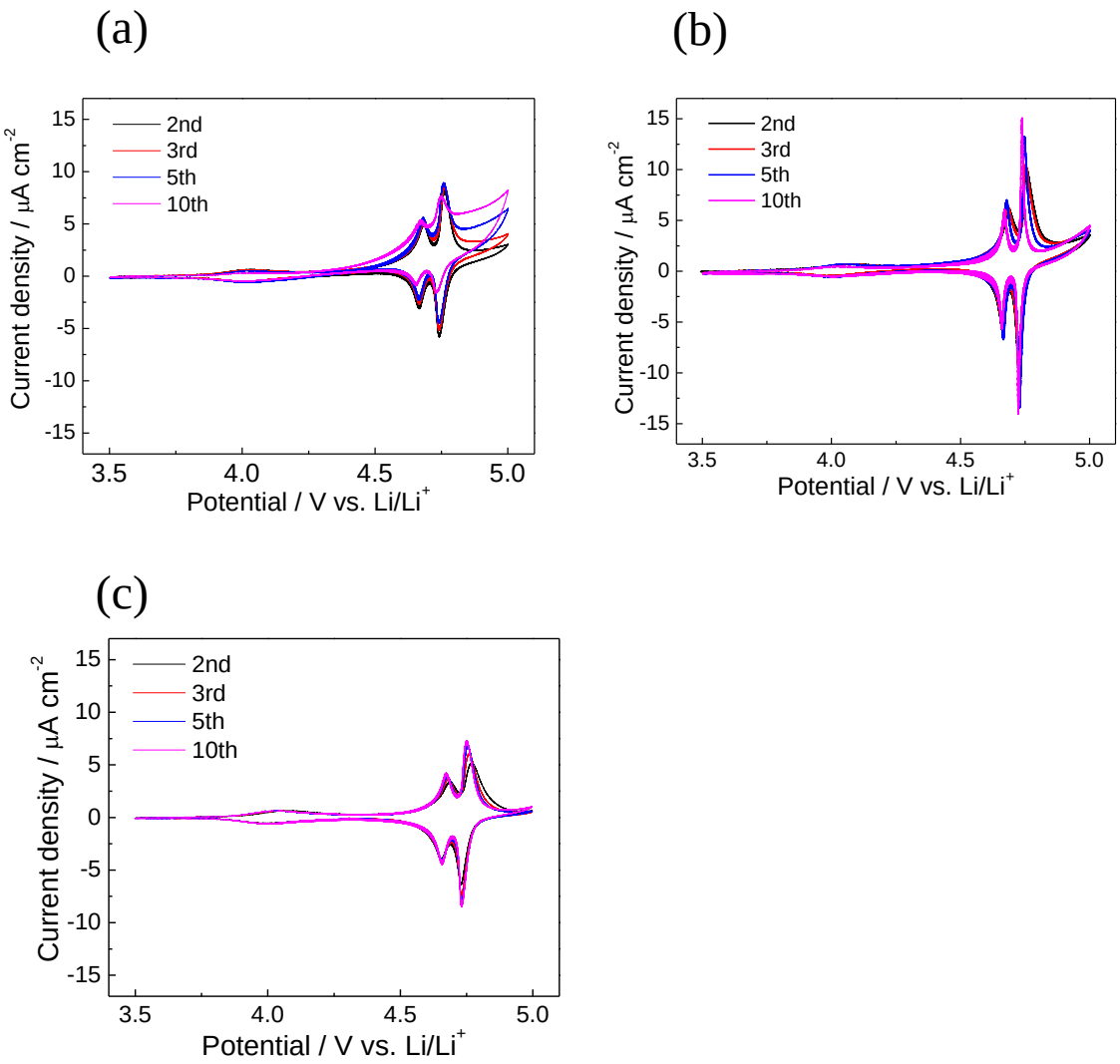

Figure 3.6 CV curves of thin-film electrodes (a) without interlayer (b) with Li_3PO_4 interlayer and (c) with LiF interlayer

.

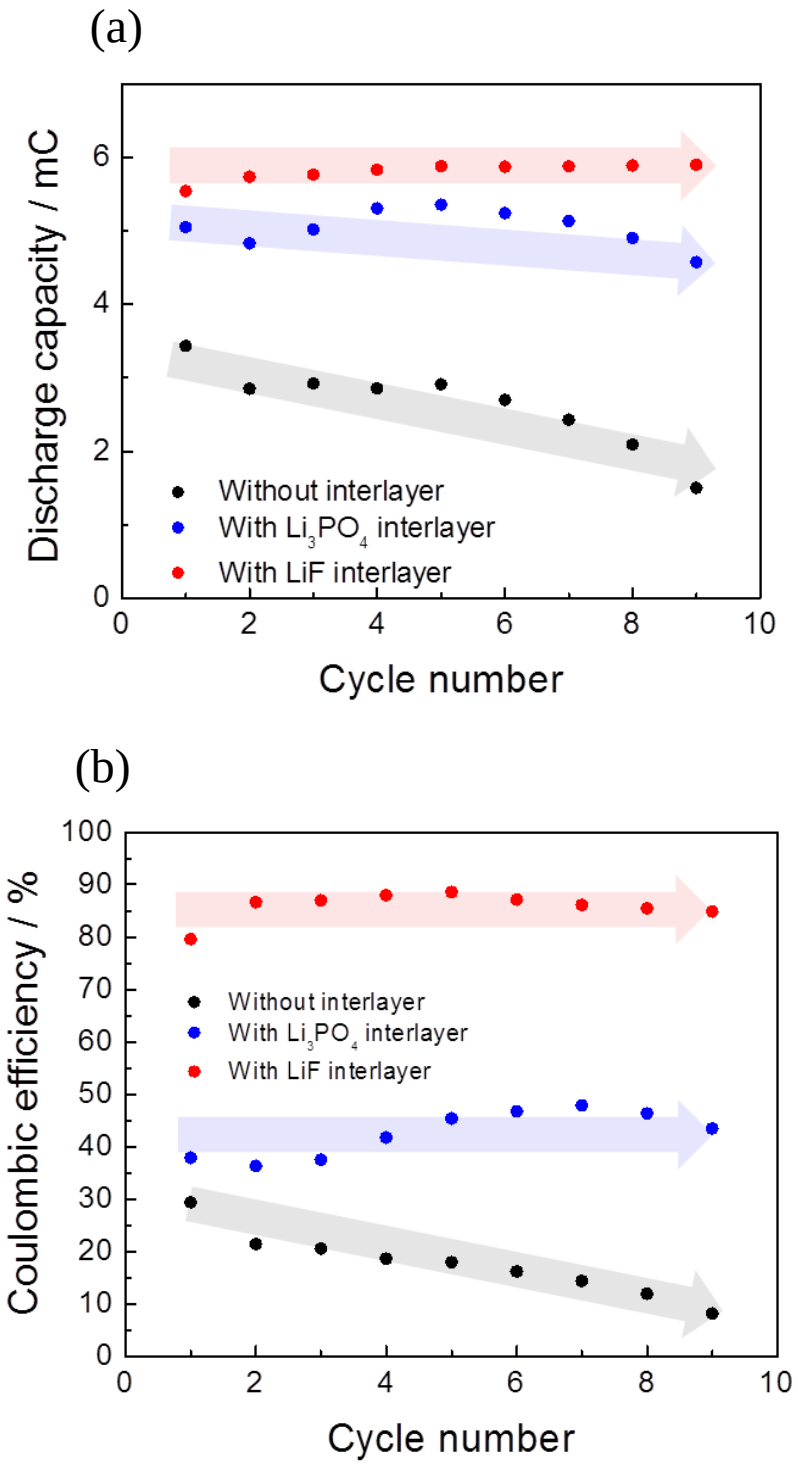

Figure 3.7 (a) Discharging capacity and (b) coulombic efficiency of electrodes with and without interlayer from 2nd cycle to 10th cycle.

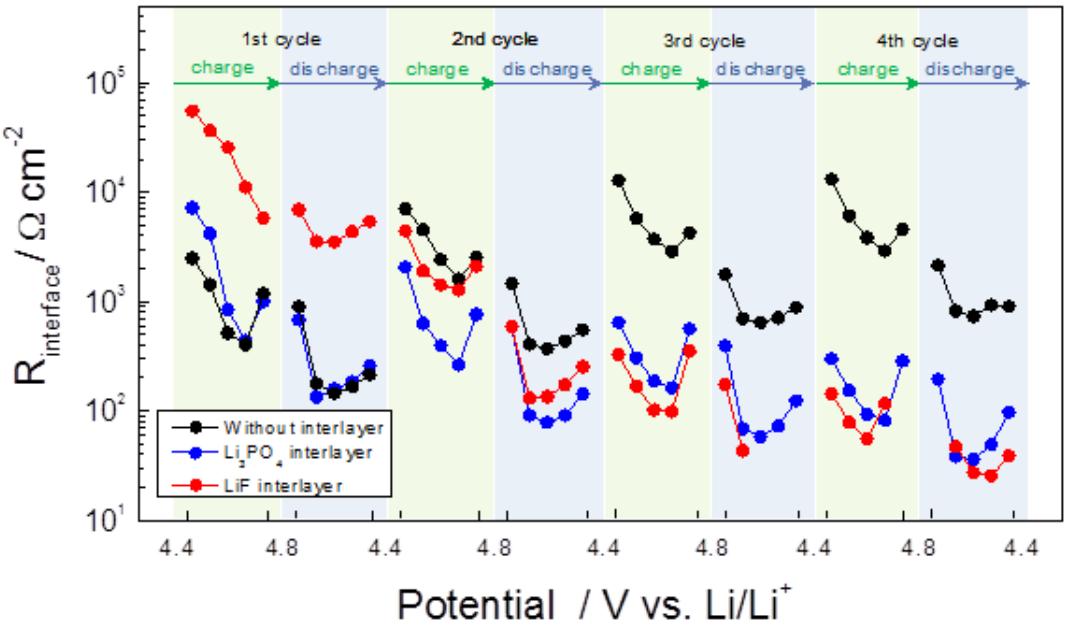

Figure 3.8 Potential-dependent interfacial resistance of thin-film electrodes without and with interlayer from 1st cycle to 4th cycle.

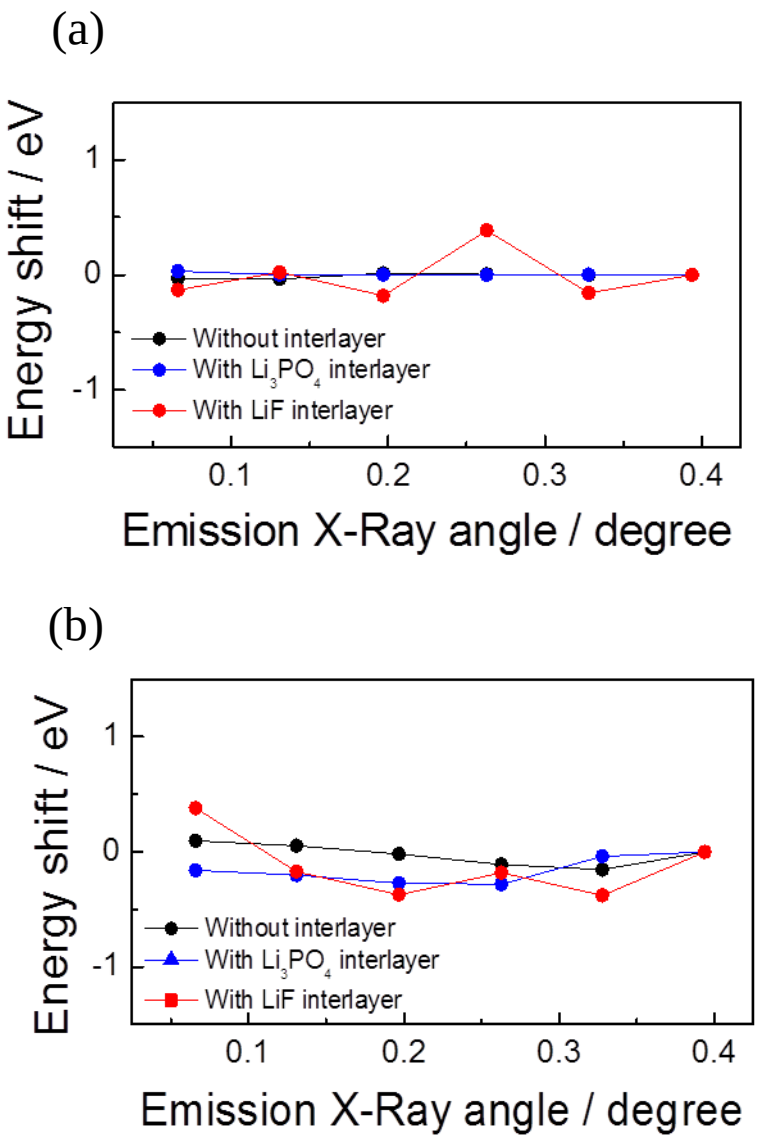

Figure 3.9 Energy shift of that before and after 1st cycle of CV measurement for both thin-film electrodes (a) without and (b) with interlayer at Mn *K*-edge.

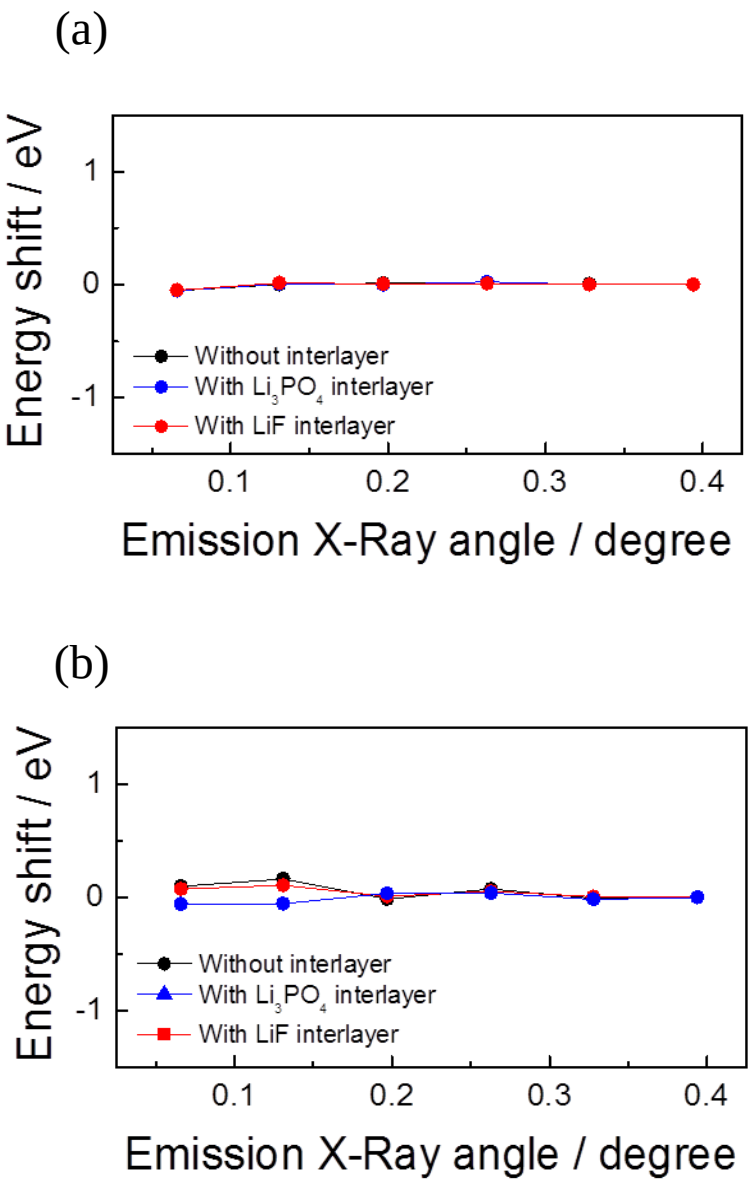

Figure 3.10 Energy shift of that before and after 1st cycle of CV measurement for both thin-film electrodes (a) without and (b) with interlayer at Ni *K*-edge.

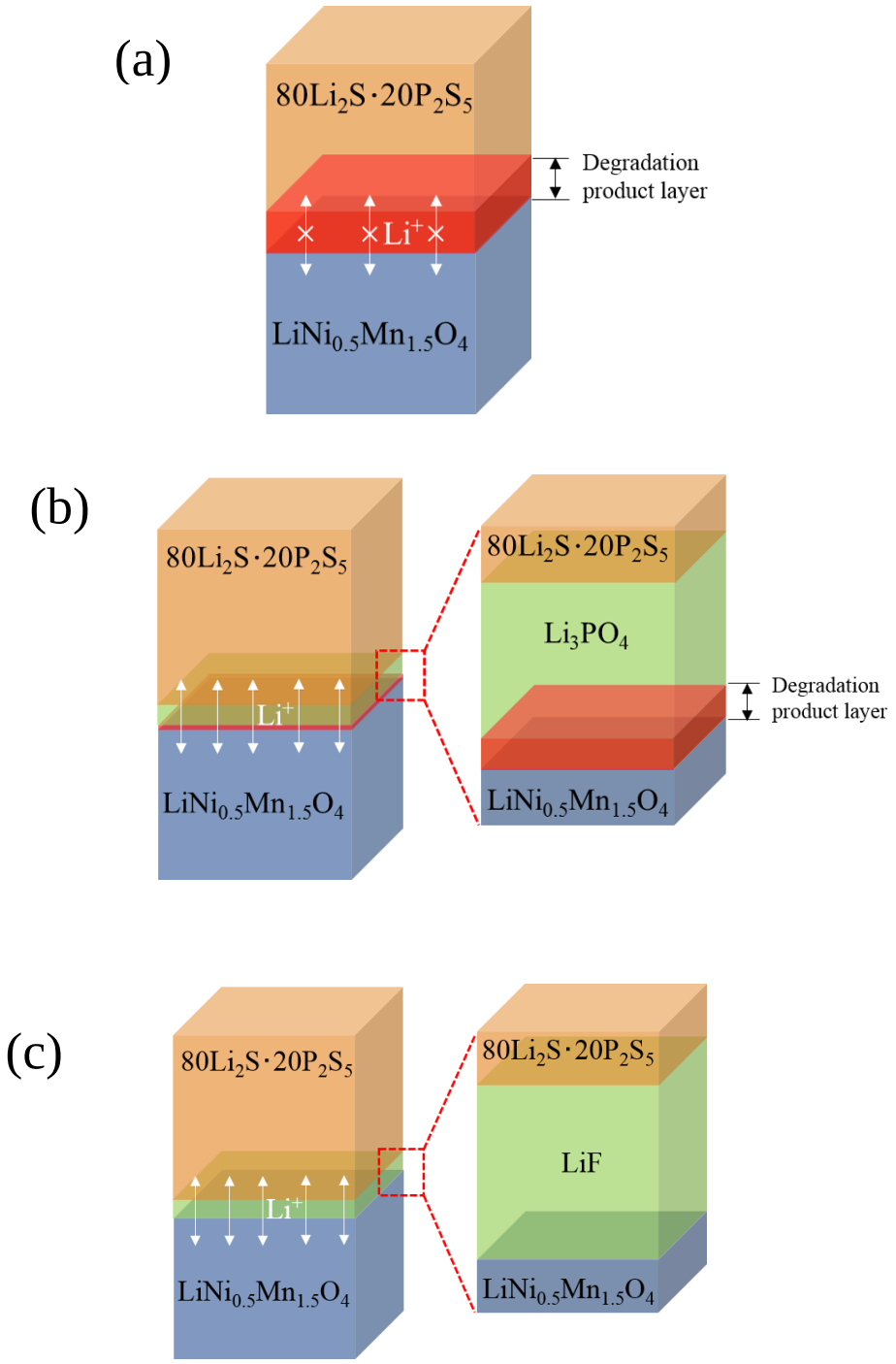

Figure 3.11 Reaction mechanism of thin-film electrodes (a) without interlayer, (b) with Li_3PO_4 interlayer and (c) with LiF interlayer during charge and discharge process.

References

(1) A. M. Haregewoin, A. S. Wotango, B. J. Hwang, *Energy Environ. Sci.* 2016, **9**, 1955-1988.

(2) C. Yada, A. Ohmori, K. Ide, H. Yamasaki, T. Kato, T. Saito, F. Sagane, Y. Iriyama, Adv.Energy Mater. 2014, 1301416.

(3) Q. Zhong, A. Bonakdarpour, M. Zhang, Y. Gao, J. R. Dahn, *J. Electrochem. Soc.* 1997, **144**, 205-213.

(4) T. Ohzuku, K. Ariyoshi, S. Yamamoto, Y. Makimura, *Chem. Lett.* 2001, **12**, 1270-1271.

(5) K. Ariyoshi, Y. Iwakoshi, N. Nakayama, T. Ohzuku, *J. Electrochem. Soc.* 2004, **151**, A296-A303.

(6) H. Morimoto, H. Awano, J. Terashima, Y. Shindo, S. Nakanishi, V. Ito, K. Ishikawa, S. Tobishima, *J. Power Sources* 2013, **240**, 636-643.

(7) C. Li, L. Gu, J. Maier, *Adv. Funct Mater.* 2012, **22**, 1145-1149.

(8) N. Ohta, K. Takada, I. Sakaguchi, L. Zhang, R. Ma, K. Fukuda, M. Osada, T. Sasaki, *Electrochem. commun.* 2007, **9**, 1486-1490.

(9) N. Ohta, K. Takada, L. Zhang, R. Ma, M. Osada, T. Sasaki, *Electrochem. commun.* 2006, **18**, 2226-2229.

(10) Y. Sakurai, A. Sakuda, A. Hayashi, M. Tatsumisago, *Solid State Ionics* 2011, **182**, 59-63.

(11) Y. Ito, Y. Sakurai, S. Yubuchi, A. Sakuda, A. Hayashi, M. Tatsumisago, *J. Electrochem. Soc.* 2015, **162**, A1610-A1616.

(12) K. Takada, N. Ohta, L. Zhang, K. Fukuda, I. Sakaguchi, R. Ma, M. Osada, T. Sasaki, *Solid State Ionics* 2008, **179**, 1333-1337.

(13) N. Machida, J. Kashiwagi, M. Naito, T. Shigematsu, *Solid State Ionics* 2012, **225**, 354-358.

(14) S. T. Myung, K. Izumi, S. Komaba, Y. K. Sun, H. Yashiro, N. Kumagai, *Chem. Mater.* 2005, **17**, 3695-3704.

(15) S. Yubuchi, Y. Ito, T. Matsuyama, A. Hayashi, M. Tatsumisago, *Solid State Ionics* 2016, **285**, 79-82.

(16) C. Li, L. Gu, J. Maier, *Adv. Runct. Mater.* 2012, **22**, 1145-1149.

(17) K. Takada, N. Ohta, L. Zhang, K. Fukuda, I. Sakaguchi, R. Ma, M. Osada, T. Sasaki, *Solid State Ionics* 2008, **179**, 1333-1337.

(18) J. Haruyama, K. Sodeyama, L. Han, K. Takada, Y. Tateyama, *Chem. Mater.* 2014, **26**, 4248-4255.

(19) A. Sakuda, A. Hayashi, M. Tatsumisago, *Chem. Mater.* 2010, **22**, 949-956.

(20) D. Takamatsu, T. Nakatsutsumi, S. Mori, Y. Orikasa, M. Mogi, H. Yamashige, K. Sato, T. Fujimoto, Y. Takamashi, H. Murayama, M. Oishi, H. Tanida, T. Uruga, H. Arai, Y. Uchimoto, Z. Ogumi, *J. Phys. Chem. Lett.* 2011, **2**, 2511-2514.

(21) S. Yubuchi, Y. Ito, T. Matsuyama, A. Hayashi, M. Tatsumisago, Solid State Ionics 2016, **285**, 79-82.

(22) A. Sakuda, A. Hayashi, S. Hama, M. Tatsumisago, *J. Am. Ceram. Soc.* 2010, **93**, 765-768.

(23) Q. Zhong, A. Bonakdarpour, M. Zhang, Y. Gao, J. R. Dahn, *J. Electrochem. Soc.* 1997, **144**, 205-213.

(24) K. Kanamura, W. Hoshikawa, T. Umegaki, *J. Electrochem. Soc.* 2002, **149**, A339-A345.

(25) W. D. Richards, L. J. Miara, Y. Wang, J C. Kim, G. Ceder, *Chem. Mater.* 2016, **28**, 266-273.

(26) T. Okumura, T. Nakatsutsumi, T. Ina, Y. Orikasa, H. Arai, T. Fukutsuka, Y. Iriyama, T. Uruga, H. Tanida, Y. Uchimoto, Z. Ogumi, *J. Mater. Chem.* 2011, **21**, 10051-10060.

Chapter 4. Elucidation of Reaction Distribution in Composite Electrode of All-Solid-State Battery by Two-Dimensional X-Ray Absorption Spectroscopy

4.1. Introduction

All-solid-state lithium-ion batteries are a promising candidate for the large-scale use of batteries in electric vehicles and smart grid systems [1, 2], owing to their properties of high safety and larger energy density in comparison with the conventional lithium-ion batteries using a liquid electrolyte.[3–5] However, the rate capability of all-solid-state batteries is still insufficient for the demand of next generation batteries.[6] One of the reasons is the inhomogeneous reaction distribution in composite electrodes, which is used in all-solid-state batteries.[7] The composite electrodes in all-solid-state lithium-ion batteries consist of active cathode materials, solid electrolyte, conduction additives, and binder materials. Thus, they form complex ionic and electronic pathways during charge/discharge.[7, 8] The dispersion state and interaction of these components greatly influences the supply of ions and electrons at partial positions, which causes a reaction distribution in the composite electrode and reduces the utilization efficiency of the cathode materials.[9] However, the relationship between the dispersion state and the

reaction distribution in the composite electrode used in all-solid-state batteries has not been clarified yet.[10, 11]

To understand the relationship between the dispersion state and the reaction distribution, the visualization of the electrochemical reaction's progress along the depth and the in-plane direction of the composite electrode is a powerful technique. We have developed an *operando* two dimensional imaging X-ray absorption spectroscopy (2D-XAS)[12, 13] method to investigate the reaction distribution within composite electrodes in the in-plane and cross sectional directions. In this study, two different types of binder materials were used to fabricate the composite electrodes. The effects of the different binder materials on the reaction distribution in the composite electrodes were analyzed using the 2D-XAS method, which detects the change of the Ni *K*-edge X-ray absorption spectra of $LiNi_{1/3}Co_{1/3}Mn_{1/3}O_2$ as a function of position.

4.2. Experimental Section

4.2.1. Fabrication of Composite Electrodes

Two types of composite electrodes were prepared with different binder materials using a procedure similar to that described in a previous report.[14] The cathode active material, solid electrolyte, and conductive additive were $LiNbO_3$-coated $LiNi_{1/3}Co_{1/3}Mn_{1/3}O_2$ (NCM), acetylene Black (AB), and $75Li_2S \cdot 25P_2S_5$ glass (LPS), respectively. Two different types of binder materials were used: styrene-butadiene rubber (SBR) and styrene-ethylene-butylene-styrene (SEBS). In this study, the composite electrode using SBR as the binder materials, and the composite electrode

using SEBS as the binder materials are termed as the SBR electrode and the SEBS electrode, respectively. For the fabrication of the SBR electrode, the slurry was prepared by mixing NCM:AB:LPS:SBR=70:30:3:3 (wt %) with anisole solvent. For the fabrication of the SEBS electrode, the slurry was prepared by mixing NCM:AB:LPS:SEBS=70:30:3:3 (wt %) with heptane solvent. The obtained slurry was coated on Al foil that served as a current collector. Additionally, the slurry dried at room temperature for 72 h for the SBR electrode and 24 h for the SEBS electrode to obtain sheet-type electrodes. Then, the sheet-type electrodes were pressed uniaxially at 360 MPa to reduce the thickness. All steps were carried out in a glove box under an Argon atmosphere.

4.2.2. Fabrication of Cells for Electrochemical Measurement

To analyze the effects of different binder materials on the electrochemical performance in composite electrodes, pellet-type cells using composite electrodes were fabricated. $75Li_2S \cdot 25P_2S_5$ glass and $Li_{0.1}In$ foil were used as the solid electrolyte and anode, respectively. The composite electrode was punched into ϕ 10 mm and placed into a cylindrical cell. Then, 80 mg of $75Li_2S \cdot 25P_2S_5$ solid electrolyte powder were placed onto the composite electrode as a separator layer. These two layers were pressed at 330 MPa to be pelletized. Finally, a ϕ 10 mm anode foil was put onto the separator layer to form the pellet-type cells, which were constrained by a persistent pressure of approximately 150 MPa during the electrochemical measurement to maintain contact between these three layers. The thickness of the composite electrode, separator layer,

and anode were approximately 100 μm, 500 μm, and 100 μm, respectively. All steps were carried out in a glove box under an Argon atmosphere.

4.2.3. Fabrication of Cells for 2D-XAS Measurement

Sheet-type cells were fabricated for the 2D-XAS measurements to analyze the reaction distribution in the composite electrodes. A schematic diagram of the cross-sectional and overhead views of the sheet-type model cell is shown in Figure 4.1. The solid electrolyte sheet that was used as separator was fabricated by mixing a $75Li_2S \cdot 25P_2S_5$ glass solid electrolyte and an SBR binder with anisole solvent (95:5, wt %). The slurry was coated onto Cu foil and dried for 72 h at room temperature under an Argon atmosphere. After uniaxial pressing at 520 MPa, the solid electrolyte sheet (120-150 μm) was peeled off from the Cu foil and used as a separator independently. The composite electrodes were used as a cathode. The size and thickness of each component in the model cell are listed in Table 1. A titanium foil was set at a specific position on the composite electrode. Subsequently, the solid electrolyte sheet was placed such that it covered the entire composite electrode. To avoid a short circuit, a lithium ionic conductive polymer sheet was placed on the solid electrolyte sheet. Moreover, a lithium foil was placed as the anode over the lithium ionic conductive polymer sheet. Ni and Cu tabs were used as current collectors for the composite electrode and anode, respectively. Finally, the entire model cell was sealed with laminate film to prevent the components from contacting the air atmosphere.

4.2.4. Electrochemical Measurement

Charge/discharge and electrochemical impedance spectroscopy (EIS) measurements were carried out by using pellet-type cells. The charge/discharge measurements were carried out at 30 °C with a current density of 64 μA cm^{-2}, which corresponded to a rate of approximately 1/40 C. The cutoff potential was set to 2.0 V-3.7 V (vs. $Li_{0.1}In$), which corresponds to 2.6 V-4.3 V (vs. Li^+/Li). Moreover, EIS measurement was carried out to measure the internal resistance of both cell types after charging to 3.7 V. The frequency range was 10^{-2} Hz-10^6 Hz and the amplitude was 30 mV.

4.2.5. 2D-XAS Measurement

2D-XAS measurement[13] was carried out for Ni *K*-edge by a transmission mode using a synchrotron radiation beam at the BL37XU beam line, SPring-8, Japan. The intensity of the transmission X-ray was recorded by a two-dimensional detector consisting of a complementary metal oxide semiconductor (CMOS) image sensor, scintillator (LuAG:Ce^+, thickness=10 μm), and magnifying glasses. The transmitted light was converted into visible light by the scintillator. Then, the visible light was enlarged five times by the magnifying glasses and guided to the image sensor. The image sensor was composed of 2,048 × 2,048 CMOS elements, and the pixel size was 6.5 μm × 6.5 μm. Therefore, the maximum field of view was 13.312 mm × 13.312 mm and the resolution was 1.3 μm × 1.3 μm under ideal conditions. By

changing the energy of the incident X-ray, 2D-XAS measurements were carried out in 20 minutes per spectrum under the continuous charge of the cells at a rate of 1/40 C.

Figure 4.2 illustrates the observation region of the composite electrodes for the 2D-XAS measurements. The incident X-ray with a beam size of 200 × 650 μm penetrated from the top to the bottom of the cell. A titanium foil was inserted between the composite electrode and the solid electrolyte sheet in the cell. In the region covered with titanium foil, the movement of the lithium ions in the electrode was restricted to the in-plane direction of the composite electrode. Here, this region is represented as an ion-blocking region. Conversely, in the regions where the titanium foil was not inserted, the electrode reaction proceeded normally. Thus, this is represented as a non-blocking region. The movement of ions in the ion-blocking region follows the movement of ions (potential gradient) in the adjacent non-blocking region. For example, in the ion-blocking region under a charge process, the extraction reaction of lithium ions occurs from the boundary between the non-blocking region and the ion-blocking region, and results in an electrode reaction. By comparing the anisotropy in the direction of the electrode reaction progress, it can be assumed that the non-blocking region functions as a separator layer for the adjacent ion-blocking region. In other words, in the ion-blocking region, the reaction behavior can be simulated in the electrode thickness direction. Thus, in this paper, the ion-blocking region is termed as the cross-sectional direction, while the non-blocking region is termed as the in-plane direction.

4.3. Results and Discussion

4.3.1. Electrochemical Measurement

Figure 4.3 shows the charge/discharge curves of the SBR and SEBS electrodes. In comparison with the SBR electrode, the SEBS electrode exhibited lower charging and discharging capacities, and larger polarization. Figure 4.4 shows the Nyquist plots for each sample after charging to 3.7 V (vs. Li-In). Although a semicircle attributed to the charge transfer resistance was observed in both electrodes, the SBR electrode had a lower charge-transfer resistance. These results correspond to the results of the charge/discharge curves. The difference with regard to electrochemical performance in these two types of electrodes also reflects the difference of the reaction distribution in the composite electrodes.

4.3.2. Reaction Distribution in In-Plane Direction

Figure 4.5(a) shows the X-ray absorption spectra at the Ni *K*-edge of the NCM composite electrode that was prepared for the 2D-XAS measurements as a reference for the state of charge (SOC) in the sample. When the NCM was charged, the spectra shifted to higher energy, which indicates the oxidation of Ni ions. For a more quantitative evaluation, in Figure 4.5(b), the peak top energy of each XANES spectrum is plotted as a function of the Li content extracted from the NCM. Before charging, the peak top energy was at 8,347.6 eV. After charging to x = 1, the peak top energy shifted to 8,351.9 eV. This observation is in good agreement with a previous report.[15]

For both the SBR electrode and the SEBS electrode, the X-ray transmission image of the composite electrodes and the reacted area mapping result along the in-plane direction are shown in Figure 4.6. For each electrode, all images were observed in the same region. The X-ray transmission image is a diagram expressing the transmitted light intensity ratio using light and dark shades, and the amount of incident light absorbed by each element in the sample is reflected in the contrast (brightness). In the sheet cells for this measurement, the parts except the positive electrode layer did not have a distribution in the absorption intensity of the incident X-ray because they were a homogeneous film. Therefore, the lightness distribution of the X-ray transmission image reflected on the dispersion of the absorption intensity in the composite electrode layer. Because the energy of the incident X-ray was in the vicinity of the Ni *K*-edge and the positive electrode material did not contain another element with a nearby absorption edge, the absorption amount by the Ni element was the largest. Therefore, the X-ray transmission image captured the dispersion of the active material's NCM particles. This image was averaged in the depth direction (the thickness direction of the sheet cell) because it contained information on all the elements that existed on the optical path of the incident X-ray. The lower the lightness was, the more the X-ray was absorbed by the NCM.

As shown in Figure 4.6, a clear lightness distribution was not observed in the X-ray transmission image of the SBR electrode, which means that the active material particles dispersed uniformly in the SBR electrode. Conversely, the lightness distribution was observed in the X-ray transmission of the SEBS electrode. The lower

lightness region indicates that the active material particles were agglomerated, while the higher lightness indicates that the solid electrolyte agglomerated. These results suggest that the macroscale structure of the SEBS electrode is non-uniform.

The reacted area mapping at different SOC for both electrodes is also shown in Figure 4.6. In the SBR electrode shown in Figure 4.6, the reaction proceeded uniformly in the in-plane direction at 3% SOC, and a slight distribution was observed at a high SOC (18%). In the SEBS electrode, the reaction proceeded preferentially in a specific region from the very beginning of charging at 3% SOC. As charging proceeded, the reaction area spread around the specific regions. By comparing this result with the X-ray transmission image, it can be seen that the reaction proceeded preferentially around the active material agglomerates.

4.3.3. Reaction Distribution in Cross-Sectional Direction

The mapping results of the reacted region in the cross-sectional direction of both electrodes are shown in Figure 4.7. These results confirm that the reaction region spread from the electrolyte side (0 μm position) for both electrodes. The cause of the reaction distribution can be discussed with regard to the balance of the electronic conduction and ionic conduction.[12, 13] It has been reported that, for NCM, the electronic conductivity is improved markedly by eliminating Li, and is three times larger than the lithium ionic conductivity of the solid electrolyte.[16, 17] Moreover, the composite electrodes contain 3wt% AB. Therefore, the formation factor of the reaction distribution should be the lithium ionic conduction and the penetration depth of the reaction is

limited by the lithium ionic conduction. In the SBR electrode with a homogeneous structure, the reaction proceeded uniformly at a depth of 20 μm. This result corresponds to that of the in-plane direction. In the SEBS electrode with a heterogeneous structure, the reaction spread from the aggregated domain structure and was observed at a depth of 20 μm, which is similar to the behavior of the in-plane direction.

To discuss the propagation of the reaction in this ion block region more quantitatively, the reaction amount profiles in the cross-sectional direction were calculated for both electrodes at 21% of SOC. The averaged XANES spectra were calculated according to the reaction amount in a rectangular region of 170 μm × 2.6 μm against the observation region shown in Figure 4.7. Then, the energy value of the peak top in the XANES spectra was extracted. A one-dimensional reaction amount profile can be obtained by performing this operation continuously along the electrode depth direction (lateral direction in the image), and by plotting the peak top energy change according to the distance from the ion-blocking edge. The results are presented in Figure 4.8. In the SBR electrode, which had a uniform structure, it was found that the reaction permeated deeper into the electrode. Conversely, in the SEBS electrode, which had a non-uniform structure, the reaction did not penetrate deeper into the electrode, in comparison with the SBR electrode.

To calculate the diffusion coefficient in the composite electrode, fitting was carried out using the diffusion expressed by Equation (1), which describes the one-dimensional

diffusion in the bulk against the reaction amount profile shown in Figure 4.8. The fitting results for both electrodes are shown in Figure 4.8 as curves.

$$\frac{c(x,t)}{c_0} = \frac{1}{\sqrt{\pi D_{bulk} t}} exp\left(-\frac{x^2}{4D_{bulk}t}\right) \quad (1)$$

where x is the distance (cm) from the end of the ion-blocking region, t is the charging time (s), and D_{bulk} is the effective diffusion coefficient in the composite electrode ($cm^2 \cdot s^{-1}$).

From the fitting results, the D_{bulk} value was estimated as 7.5×10^{-11} cm^2 s^{-1} in the SBR electrode, and as 3.9×10^{-11} cm^2 s^{-1} in the SEBS electrode, respectively. The diffusion coefficient of the solid electrolyte $75Li_2S \cdot 25P_2S_5$ glass has been reported as $7.8 \times 10^{-10}/cm^2$ s^{-1}.[18] In comparison with the diffusion coefficient of the solid electrolyte, the effective diffusion coefficient of the composite electrodes exhibited a small diffusion coefficient in both electrodes. Moreover, the SEBS electrode exhibited a smaller diffusion coefficient than the SBR electrode.

The movement of ions depends on the tortuosity of the ionic conductive paths.[19] As mentioned before, the effective diffusion coefficient in the composite electrode is different from the value in the bulk electrolyte. The difference in the effective diffusion coefficients of the SBR electrode and the SEBS electrode indicates that the dispersion state of the composite electrode affects the behavior of lithium ion diffusion.

The factor controlling the formation of the reaction distribution in the cross-sectional direction was considered as shown in Figure 4.9. Owing to the homogeneous

structure of the SBR electrode, the ionic conductive phase, which formed by the connection of the solid electrolyte, connected into the deep portion of the electrode, and thus the reaction proceeded uniformly. In the case of the domain-like heterogeneous structure in the SEBS electrode, the ionic conductive phases were divided because of the large tortuosity. Thus, the ionic conduction resistance was larger in the deeper part of the electrode. This caused a large potential gradient and the reaction proceeded preferentially in the vicinity of the electrolyte. The cause for the difference in the dispersion state of the composite electrodes using different binder materials was considered as the different polarity of the solvents used in the preparation of the composite electrodes. The dispersion of the active materials and the solid electrolyte composite electrode was better using the SBR and polar solvent anisole, in comparison with the composite electrode using SEBS and nonpolar heptane solvent. These results suggest that the ionic conduction is the dominant factor with regard to the formation of the reaction distribution, depending on the structure of the composite electrode. The dispersion state of the composite electrode was influenced by the polarity of the solvents used in the preparation of the composite electrode. Finally, we believe that the knowledge obtained from this study can be useful in designing a composite electrode with high electrochemical performance.

4.4. Conclusion

The reaction distribution in composite electrodes using different binder materials, namely, SBR and SEBS, was analyzed both in the in-plane and cross-sectional

directions using 2D-XAS measurements. The analysis results revealed that the dispersion state of the cathode active materials and solid electrolyte in the composite electrodes exerted a remarkable influence on the formation of ionic conductive paths, leading to the reaction distribution. To suppress the reaction distribution, it is important to control the morphology of the composite electrode by choosing a suitable solvent to prepare the composite electrode.

(a)

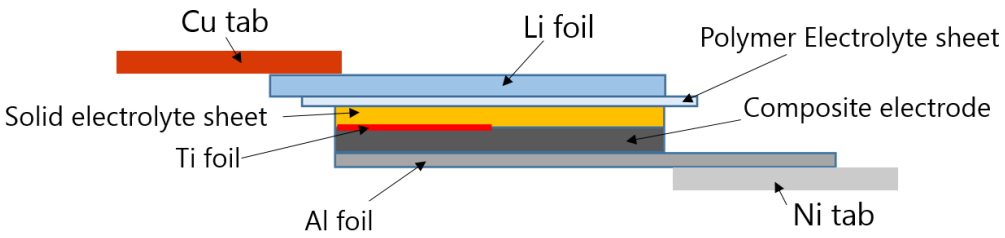

(b)

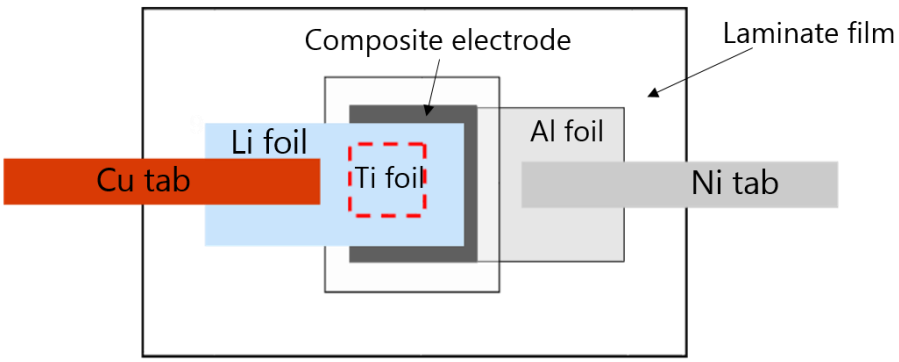

Figure 4.1 Schematic diagram of model cell: (a) cross-sectional view; (b) overhead view.

Table 1 Cell components.

	Size (mm)	Thickness (μm)
Li foil	8×20	100
Polymer Electrolyte sheet	15×15	40
Solid electrolyte sheet	10×10	120-150
Ti foil	5×5	5
Cathode sheet	10×9	75-90
Al current collector	10×20	

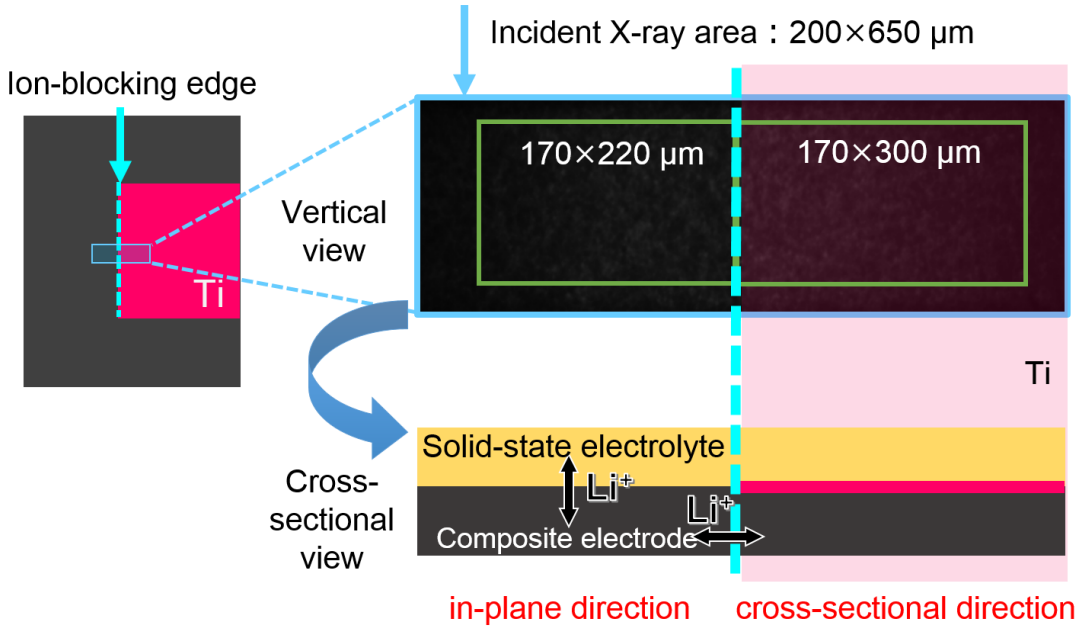

Figure 4.2 Schematic illustration of ion-blocking electrode for 2D-XAS measurements.

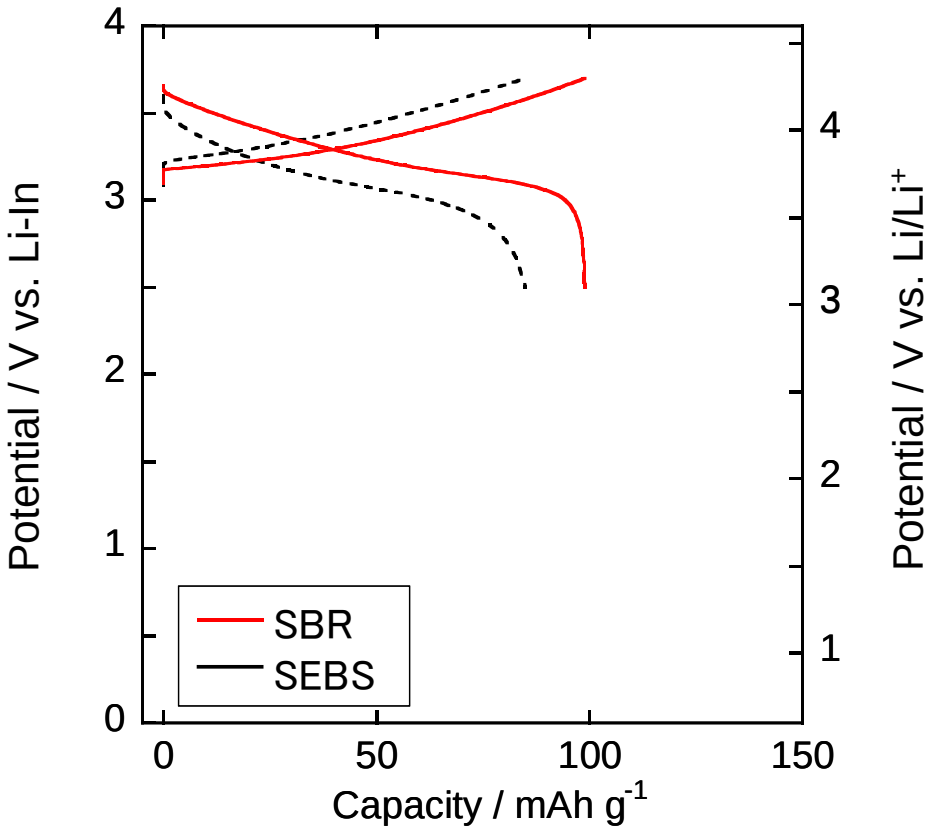

Figure 4.3 Charge/discharge curves of SBR electrode (solid red line) and SEBS electrode (dashed black line) at 30 °C with a current density of 64 μA cm^{-2}.

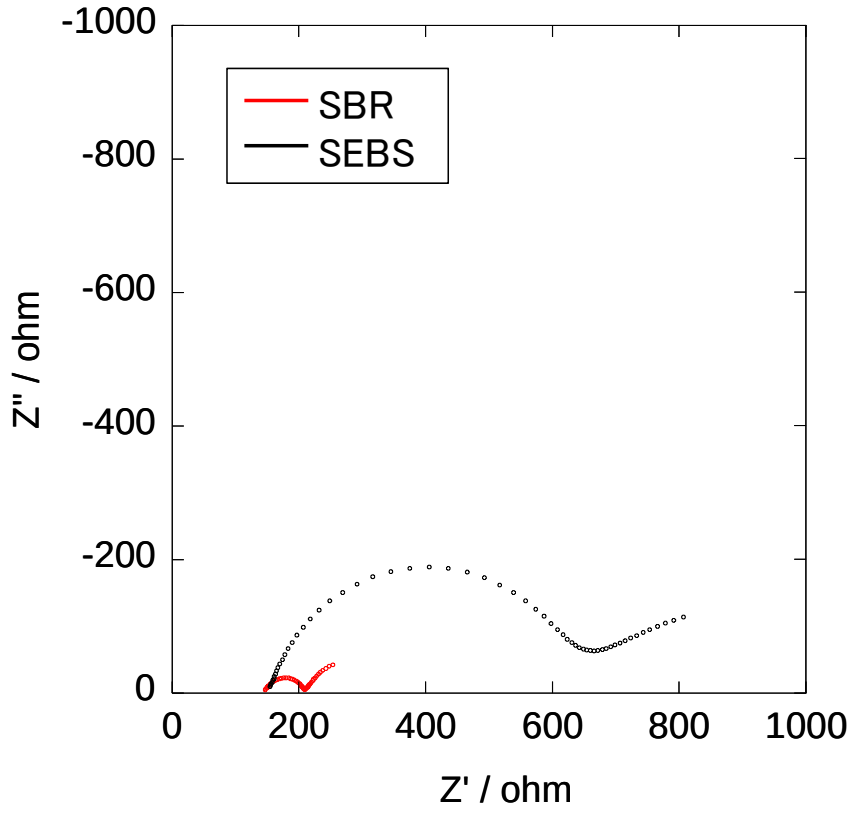

Figure 4.4 Nyquist plot of impedance after discharging to 3.7 V of composite electrodes using different binders.

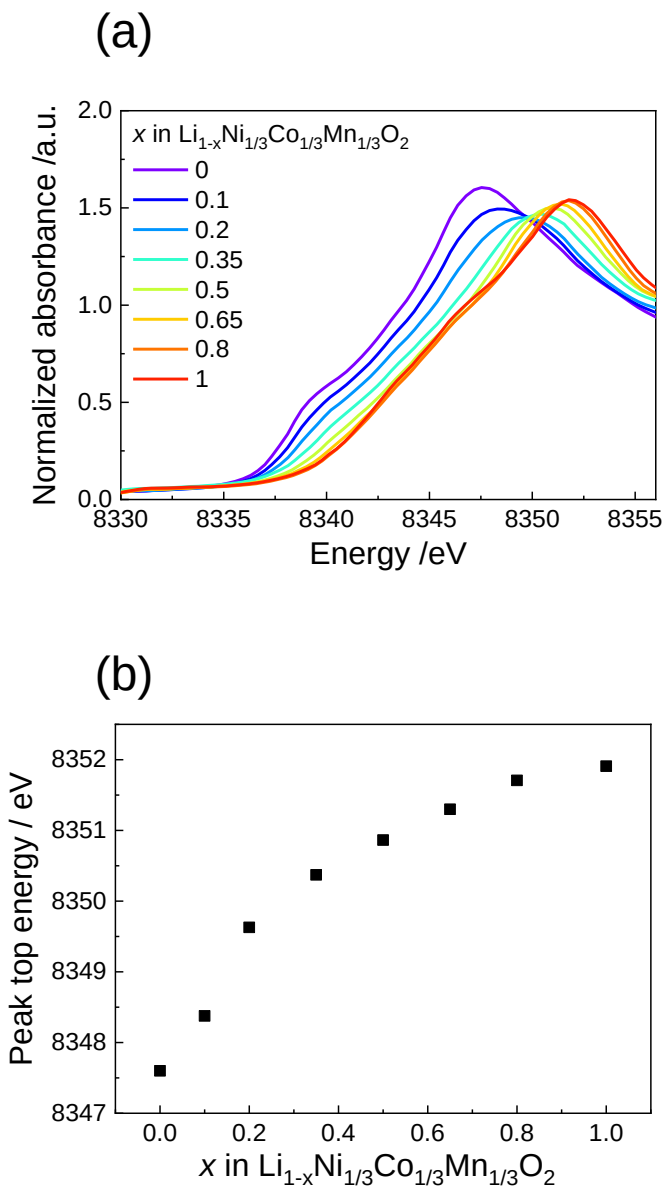

Figure 4.5 (a) X-ray absorption spectra; (b) peak top energy of $Li_{1-x}Ni_{1/3}Co_{1/3}Mn_{1/3}O_2$ with different Li content.

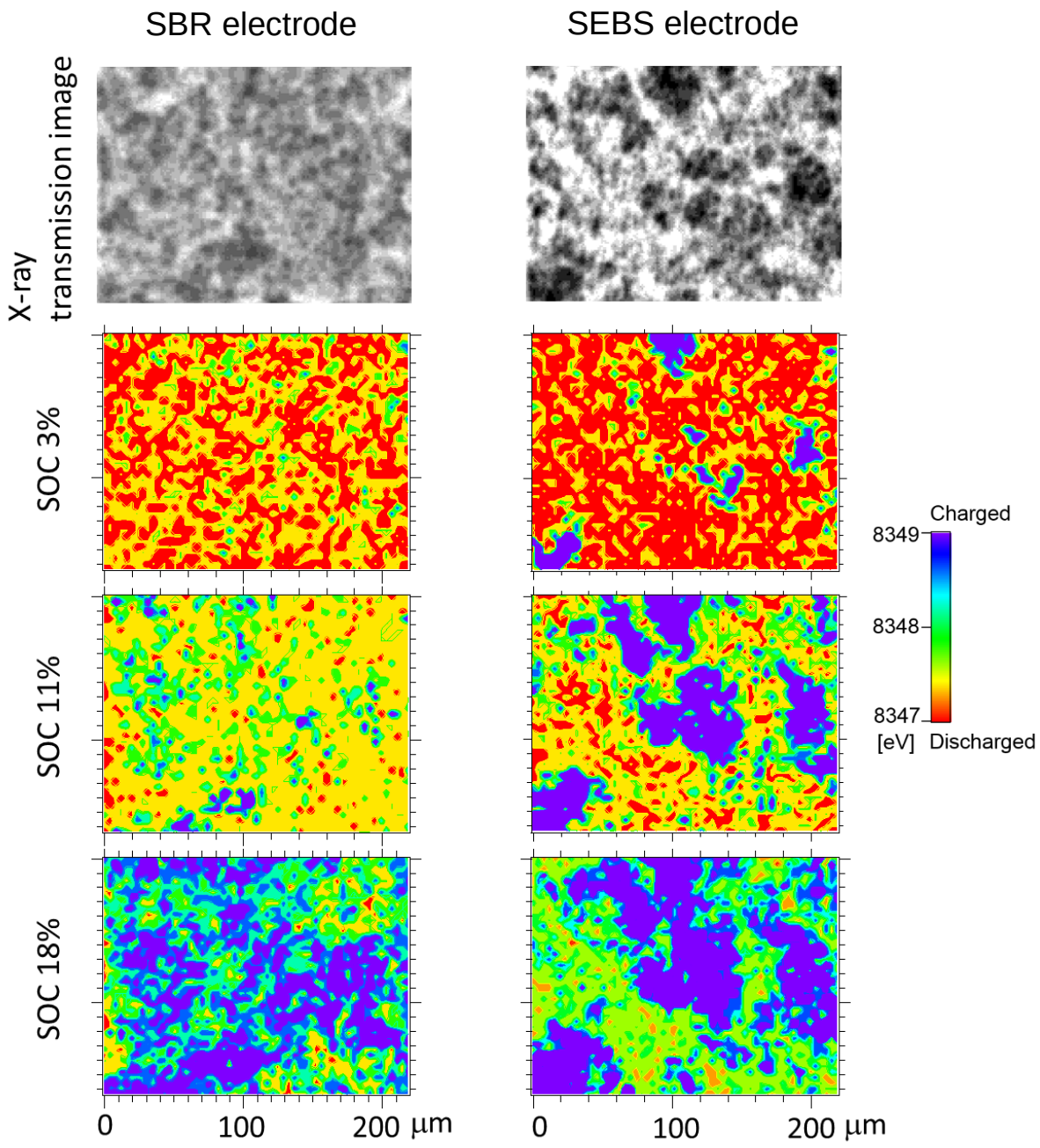

Figure 4.6 X-ray transmission images and reacted area mapping results for different SOC in in-plane direction for SBR electrode (left side) and SBES electrode (right side).

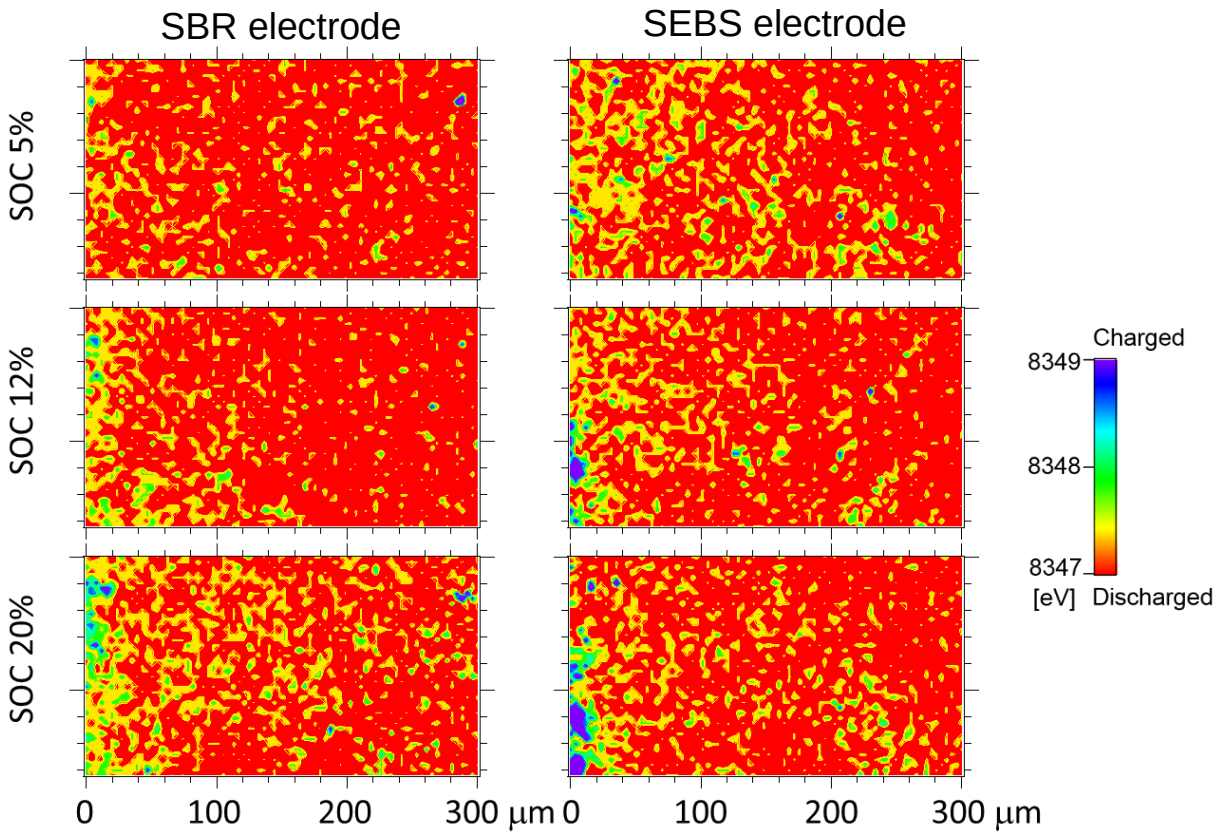

Figure 4.7 Reacted area mapping results in cross-sectional direction for SBR electrode (left side) and SEBS electrode (right side) at different SOC.

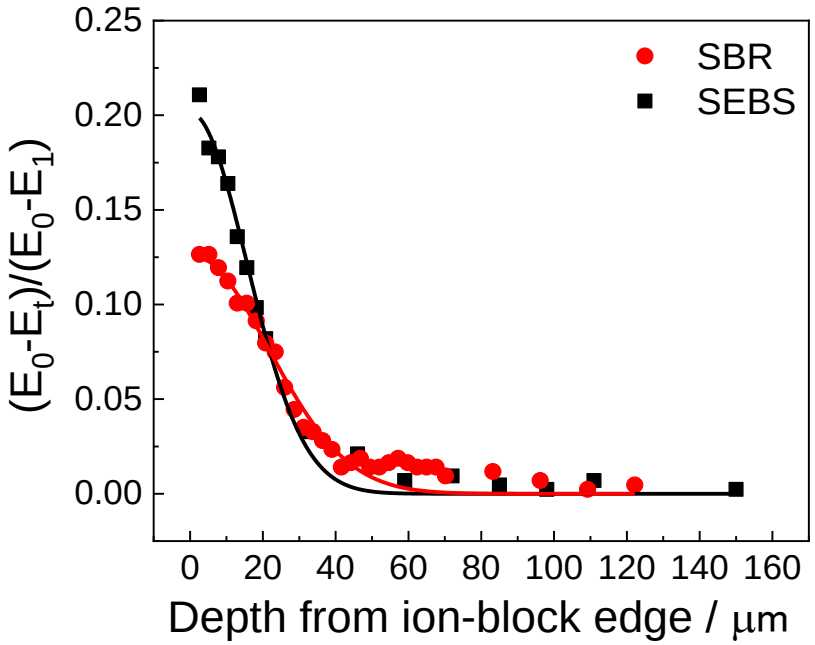

Figure 4.8 Reaction amount estimated from XANES spectra of SBR electrode and SEBS electrode as function of depth from ion-block edge.

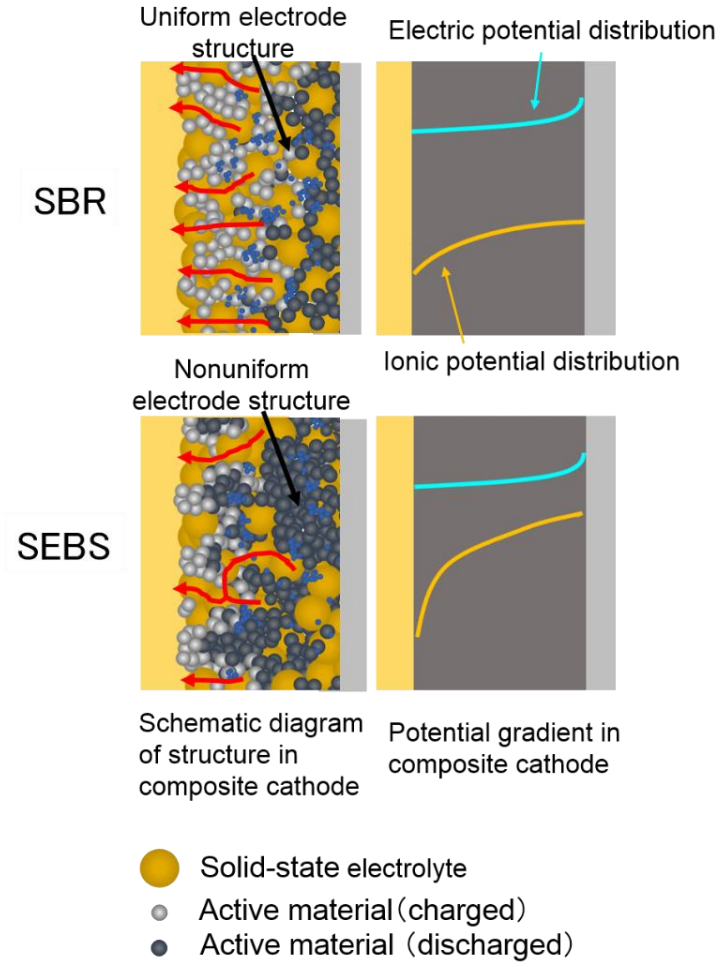

Figure 4.9 Schematic diagram of structure and potential gradient in composite cathodes using different binders.

References

(1) T. Okumura, T. Takeuchi, H. Kobayashi, *Solid State Ionics* 2016, **288**, 248–252.

(2) A. Sakuda, A. Hayashi, T. Ohtomo, S. Hama, M. Tatsumisago, *Electrochemistry* 2012, **80**, 839–841.

(3) N. J. Dudney, *Mater. Sci. Eng.* B 2005, **116**, 245–249.

(4) T. Minami, A. Hayashi, M. Tatsumisago, *Solid State Ionics* 2006, **177**, 2715–2720.

(5) J. B. Goodenough, Y. Kim, *Chem. Mater.* 2010, **22**, 587–603.

(6) A. Sakuda, T. Takeuchi, H. Kobayashi, *Solid State Ionics* 2016, **285**, 112–117.

(7) M. Tatsumisago, F. Mizuno, A. Hayashi, *J. Power Sources* 2006, **159**, 193–199.

(8) C. Sun, J. Liu, Y. Gong, D. P. Wilkinson, J. Zhang, *Nano Energy* 2017, **33**, 363–386.

(9) M. Doyle, J. Newman, *J. Appl. Electrochem.* 1997, **27**, 846–856.

(10) K. C. Hess, W. K. Epting, S. Litster, *Anal. Chem.* 2011, **83**, 9492–9498.

(11) K. C. Hess, J. F. Whitacre, S. Litster, *J. Electrochem. Soc.* 2012, **159**, A1351–A1359.

(12) Y. Orikasa, Y. Gogyo, H. Yamashige, M. Katayama, K. Z. Chen, T. Mori, K. Yamamoto, T. Masese, Y. Inada, T. Ohata, Z. Siroma, S. Kato, H. Kinoshita, H. Arai, Z. Ogumi, Y. Uchimoto, *Sci. Rep.* 2016, 26382.

(13) T. Nakamura, T. Watanabe, Y. Kimura, K. Amezawa, K. Nitta, H. Tanida, K. Ohara, Y. Uchimoto, Z. Ogumi, *J. Phys. Chem. C* 2017, **121**, 2118–2124.

(14) A. Sakuda, K. Kuratani, M. Yamamoto, M. Takahashi, T. Takeuchi, H. Kobayashi, *J. Electrochem. Soc.* 2017, **164**, A2474–A2478.

(15) Y. W. Tsai, B. J. Hwang, G. Ceder, H. S. Sheu, D. G. Liu, J. F. Lee, *Chem. Mater.* 2005, **17**, 3191–3199.

(16) X. Y. Qiu, Q. C. Zhuang, Q. Q. Zhang, R. Cao, Y.H. Qiang, P. Z. Ying, S. G. Sun, *J. Electroanal. Chem.* 2013, **688**, 393–402.

(17) M. Tatsumisago, S. Hama, A. Hayashi, H. Morimoto, T. Minami, *Solid State Ionics* 2002, **154**, 635–640

(18) T. Baba, Y. Kawamura, *Front. Energy Res.* 2016, **4**, 22.

(19) V. Ramadesigan, R. N. Methekar, F. Latinwo, R. D. Braatz, V. R. Subramanian, *J. Electrochem. Soc.* 2010, **157**, A1328–A1334.

Chapter 5. General Conclusions

Lithium ion batteries have been used in widely used in portable electronic devices such as cellphone and laptop due to their high energy density. In recent years, owing to the depletion of petroleum resources and environment pollution, vehicles using petroleum fuels are restrained and electric vehicle using electricity are promoted. Thus, there is a great desire for batteries with better safety and higher power density. Conventional lithium ion batteries using flammable liquid electrolyte have serious safety issues such as combustion and explosion. Therefore, all-solid-state batteries using nonflammable solid electrolyte are considered to be a promising candidate for electric vehicles. Among all the solid electrolyte, the sulfide solid electrolytes were attracting increasing attention due to their relative high ionic conductivity. However, the high interfacial resistance at electrode/solid electrolyte interface and the reaction distribution in composite electrode need to be solved. The present work focused on the interfacial reaction mechanism at cathode/solid electrolyte interface and the reaction distribution in composite electrode in all-solid-state batteries using sulfide electrolyte.

In general introduction, an overview of all-solid-state battery was described including the introduction of various inorganic solid electrolyte. Then the limitations of interfacial resistance and reaction distribution as well as the effort to overcome these issues were introduced. Methods to analyze and control the interfacial phenomena and the reaction distribution were reviewed.

In chapter 1, to analyze the interface between $LiCoO_2$ cathode and Li_2S-P_2S_5 solid

electrolyte, model thin-film electrodes were fabricated by PLD. And the effect of Li_3PO_4 interlayer was researched by electrochemical and DR-XAS measurement. The origin of high interfacial resistance was considered to be from the side reaction product layer formed between $LiCoO_2$ and Li_2S-P_2S_5 during charge and discharge. And the Li_3PO_4 interlayer was considered to hinder the mutual diffusion through $LiCoO_2$/Li_2S-P_2S_5 interface and the formation of reaction product layer which lead to a more stable interface.

In chapter 2, due to the need for application of high voltage cathode in all-solid-state batteries, an typical 5 V cathode materials $LiNi_{0.5}Mn_{1.5}O_4$ was introduced. The interface between $LiNi_{0.5}Mn_{1.5}O_4$ and Li_2S-P_2S_5 was investigated by electrochemical and DR-XAS measurement. The effect of Li_3PO_4 interlayer was also analyzed. The origin of high interfacial resistance was considered as the decomposition of sulfide electrolyte due to high potential gap at cathode/electrolyte interface. The introduction of Li_3PO_4 interlayer could restrain the decomposition of sulfide solid electrolyte and decrease the interface. However, Li_3PO_4 will also decompose at the operation range of $LiNi_{0.5}Mn_{1.5}O_4$. Therefore, it is necessary to find new interlayer materials for the high voltage cathode materials.

In chapter 3, LiF was used as the interlayer between $LiNi_{0.5}Mn_{1.5}O_4$ and Li_2S-P_2S_5. The interfacial reaction mechanism between $LiNi_{0.5}Mn_{1.5}O_4$ and Li_2S-P_2S_5 as well as the effect of LiF interlayer were investigated by electrochemical and DR-XAS measurement. Comparing to Li_3PO_4 interlayer, LiF interlayer resulted in even lower interfacial resistance. According to the results of both CV and EIS measurement, it

suggests that the interfacial modification by LiF interlayer can maintain a more stable interface between $LiNi_{0.5}Mn_{1.5}O_4$ cathode and $80Li_2S \cdot 20P_2S_5$ solid electrolyte than Li_3PO_4 interlayer.

In chapter 4, the reaction distribution in composite electrode of all-solid-state batteries using different binder materials was analyzed by 2D-XAS. The results of electrochemical measurement indicated that composite electrode using SBR exhibited better cell performance than that using SEBS. The results of 2D-XAS showed that the reaction distribution in composite electrode using SBR was much slighter than that of composite electrode using SEBS. These results indicated that the three-dimensional structure, especially the dispersion condition of active materials, affects the reaction distribution in composite electrode of all-solid-state batteries.

In chapter 5, the results of this thesis were summarized. By using DR-XAS techniques and electrochemical measurements, the interfacial reaction mechanisms at interface of cathode/sulfide solid electrolyte were analyzed. By 2D-XAS, the reaction distribution in composite electrodes of all-solid-state batteries using sulfide solid electrode. The results of these measurement provide important information at different scale for the fundamental study of all-solid-state batteries with better performance.

Acknowledgements

I would like to express my gratitude to all those who helped me during the writing of this thesis.

My deepest gratitude goes first and foremost to Professor Yoshiharu Uchimoto, for his constant encouragement and guidance. He has walked me through all the stages of the writing of this thesis. Without his consistent and illuminating instruction, this thesis could not have reached its present form.

I would like to express my heartfelt gratitude to Prof. Masahiro Tatsumisago, Prof. Akitoshi Hayashi and the members of Tatsumisago's laboratory for their helps and suggestions of solid-state electrolyte. I also would like appreciate Prof. Yuki Orikasa and Dr. Kentaro Yamamoto for their help and suggestion on my research.

I would to give my great gratitude to Prof. Setsuhisa Tanabe and Prof. Teppei Yoshida at Graduate School of Human and Environmental Studies, Kyoto university for their precious commonts of this thesis.

I would like to express my heartfelt gratitude to Prof. Hu Yougen, who led me into the world of batteries. I am also greatly indebted to all the members of Prof. Uchimoto's laboratory, who have instructed and helped me a lot in the past five years.

Special thanks are expressed to Dr. Tomoya Uruga and Dr. Kiyofumi Nitta at Japan Synchrotron Radiation Research Institute and Prof. Koji Amezawa for their helps on DR-XAS and 2D-XAS measurement..

Finaly, my great thanks would go to my beloved parents for their loving considerations and great confidence in me all through these years.

Kezheng Chen

Kyoto, JAPAN, November, 2017